Multiscale Modeling of Self-assembly of Nanostructures, Nanomedicines, and Functionalized Graphenes

BY

NILADRI PATRA
B.Sc., University of Calcutta, 2006
M.Sc., Indian Institute of Technology Delhi, 2008

THESIS

Submitted in partial fulfillment of the requirements
for the degree of Doctor of Philosophy in Chemistry
in the Graduate College of the
University of Illinois at Chicago, 2013

Chicago, Illinois

Defense Committee:

Petr Král, Chair and Advisor
Tim Keiderling
Preston T. Snee
Seungpyo Hong, Biopharmaceutical Sciences and Bioengineering
Hossein R. Sadeghpour, Harvard University

ACKNOWLEDGMENTS

I would like to acknowledge my advisor, Prof. Petr Král, for his constant guidance throughout my graduate studies. He encouraged me to pursue high quality research and spent enormous amount of his invaluable time to teach, motivate and discuss my research. He taught me the importance of curiosity, creativity and thoroughness in research.

I am very grateful to Prof. Seungpyo Hong and his research group in Department of Biopharmaceutical Sciences at UIC. Our collaboration on nanomedicine led to several interesting projects and helped us to find a solid basis for the theoretical modeling of their experimentally prepared nanocarrier for drug delivery. The discussion with them provided me an invaluable perspective into computational chemical biology.

I am very grateful to Dr. H. R. Sadeghpour for giving me the opportunity to work in his laboratory at the Institute for Theoretical Atomic, Molecular and Optical Physics (ITAMP) during the last year of my PhD studies. I would like to thank all the visitors and other members of ITAMP. The seminars at ITAMP and other departments at Harvard University were particularly inspiring.

I would like to thank all the faculty in the Department of Chemistry at UIC, and especially Prof. Michael Trenary and Prof. Luke Hanley for delivering inspiring lectures and their support during my studies. I also would like to acknowledge Prof. Timothy Keiderling, Prof. Scott Shippy, and Prof. Duncan Wardrop for their efforts in managing my graduate studies and career advice.

ACKNOWLEDGMENTS (Continued)

I acknowledge all the staff of the Department and particularly Ms. Silvia Solis, Ms. Patricia Ratajczyk, Ms. Rhonda Staudohar, Mr. Don Ripon, and Ms. Mary Ann Borjal for their great help.

I am also very grateful to the students in our research group and in the Department of Chemistry at UIC, who made my PhD studies an interesting experience. I would also like to thank all my group members; especially: Dr. Boyang Wang, Dr. Alexey Titov, Dr. Lela Vuković, Dr. John T. Russell, Dr. Artem Baskin, Yuanbo Song, Henry Chan, Dominic Esan, and Irena Yzeiri.

I also express my gratitude to UIC Chemistry Department (PAAREN graduate fellowship), and Harvard-Smithsonian Astrophysical Observatory (SAO predoc fellowship) for the financial support. I would like to thank the Graduate Student Council, UIC Graduate College and UIC College of Liberal Arts & Sciences for the travel awards which helped me to present my work and interact with a large scientific community at many meetings and conferences.

Last, I would like to thank my family for their constant support and encouragement during my PhD study at the University of Illinois at Chicago.

TABLE OF CONTENTS

CHAPTER			PAGE
1	**INTRODUCTION**		1
	1.1	Computational modeling of nanoscale systems	1
	1.2	Thesis structure	3
2	**THEORY AND METHODS**		6
	2.1	Introduction	6
	2.2	First-Principle Quantum Mechanical Methods	7
	2.3	Electronic Structure Calculations	8
	2.3.1	Exact Many-Electron Wavefunctions	9
	2.3.2	The Hartree-Fock Method	10
	2.3.3	Density Functional Theory	13
	2.4	Classical Molecular Dynamics Methods	16
	2.4.1	Force Field Functions	17
	2.4.2	Many-body Potentials	21
	2.4.3	Periodic Boundary Conditions	23
	2.4.4	Numerical Integration Schemes	23
	2.4.5	Statistical Ensembles in MD Simulations	24
	2.4.6	The Langevin Dynamics	25
	2.4.7	Simulation Parameters	26
	2.5	Coarse-Grained Molecular Dynamics	27
	2.5.1	Interactions between CG Particles	28
	2.5.2	Simulation Parameters	31
	2.6	Hybrid QM/MM Molecular Dynamics	31
	2.7	Ab-initio Molecular Dynamics	32
3	**NANODROPLET ACTIVATED AND GUIDED FOLDING OF GRAPHENE NANOSTRUCTURES**		34
	3.1	Introduction	34
	3.2	Computational Methods	36
	3.3	Results and Discussion	37
	3.3.1	Folding of flakes	37
	3.3.2	Folding of ribbons	41
	3.4	Conclusion	50
4	**SELF-ASSEMBLY OF GRAPHENE NANOSTRUCTURES ON NANOTUBES**		51
	4.1	Introduction	51

TABLE OF CONTENTS (Continued)

CHAPTER **PAGE**

4.2 Computational Methods . . . 52
4.3 Results and Discussion . . . 53
4.3.1 GNR folding outside and inside CNTs . . . 53
4.3.2 Analytical model . . . 58
4.3.3 Testing of the analytical model . . . 60
4.3.4 More complex nanostructures . . . 64
4.4 Conclusion . . . 69

5 CONTROLLED SELF-ASSEMBLY OF FILLED MICELLES ON NANOTUBES . . . 70
5.1 Introduction . . . 70
5.2 Computational Methods . . . 72
5.3 Results and Disussion . . . 74
5.3.1 Double-headed lipid micelles . . . 74
5.3.2 Single-headed lipid micelles . . . 77
5.4 Conclusion . . . 80

6 POROUS CARBON NANOTUBES: MOLECULAR ABSORPTION, TRANSPORT, AND SEPARATION . . . 82
6.1 Introduction . . . 82
6.2 Computational Methods . . . 83
6.3 Results and Discussion . . . 84
6.3.1 Condensation and transport of water within PCNTs . . . 84
6.3.2 Exchange of ions using PCNTs . . . 88
6.3.3 Separation of organic mixtures using PCNTs . . . 90
6.4 Conclusion . . . 94

7 NANOMEDICINE I: DENDRON MEDIATED SELF-ASSEMBLY OF PEGYLATED BLOCK COPOLYMERS . . . 95
7.1 Introduction . . . 95
7.2 Synthesis of PEGylated Dendron-Coils . . . 96
7.3 Atomistic Modeling of PEGylated DCs and Their Assemblies 100
7.3.1 Computational Methods . . . 100
7.3.2 Configurational Entropies of Linear and Branched Copolymers 101
7.3.3 Modeling PDC Micelles . . . 102
7.3.4 Computational Results . . . 103
7.4 Characterization of PDC Nanomicelles . . . 103
7.5 Conclusion . . . 106

TABLE OF CONTENTS (Continued)

CHAPTER **PAGE**

8 NANOMEDICINE II: POSITIVELY CHARGED DENDRON MICELLES DISPLAY NEGLIGIBLE CELLULAR INTERACTIONS . . . 107
8.1 Introduction . . . 107
8.2 Synthesis of PEGylated Dendron Copolymers . . . 109
8.3 Molecular Dynamics (MD) Simulations of PDCs and Micelles 110
8.3.1 Computational Methods . . . 110
8.3.2 Modeling PDC Micelles . . . 111
8.4 Characterization of PDC Micelles . . . 112
8.5 Conclusion . . . 118

9 DYNAMICS OF ION BINDING TO GRAPHENE NANOSTRUCTURES . . . 120
9.1 Introduction . . . 120
9.2 Computational Methods . . . 122
9.3 Results and Discussion . . . 122
9.3.1 Coronene ($C_{24}H_{12}$) . . . 122
9.3.2 Triangular Graphene Flakes . . . 125
9.3.3 Simulation of Other Ions . . . 128
9.3.4 Porous Graphene Flakes . . . 129
9.3.5 Passage over the Nanostructure edge . . . 132
9.4 Conclusion . . . 132

10 SELF-ASSEMBLY OF LARGE CARBON-RICH STRUCTURES IN INTERSTELLAR MEDIUM . . . 134
10.1 Introduction . . . 134
10.2 Computational Method . . . 137
10.3 Results and Discussion . . . 139
10.3.1 Formation of chain and cage structures: dependence with gas temperature . . . 140
10.3.2 Formation of chain and cage structures: dependence with gas density . . . 143
10.3.3 Hydrogenation process . . . 144
10.3.4 Carbon inflow: non-equilibrium nucleation . . . 144
10.3.5 Probability Distribution of Cluster sizes . . . 147
10.4 Conclusion . . . 151

11 CONCLUDING REMARKS . . . 153

CITED LITERATURE . . . 157

APPENDIX . . . 184

TABLE OF CONTENTS (Continued)

CHAPTER **PAGE**

VITA 189

LIST OF TABLES

TABLE		PAGE
I	CRITICAL MICELLE CONCENTRATIONS (CMCS) OF THE AMPHIPHILIC COPOLYMERS WITH VARIOUS HYDROPHILIC-LIPOPHILIC BALANCES (HLBS)	99
II	MOLECULAR WEIGHT AND POLYDISPERSITY INDICES (PDIS) OF SYNTHESIZED PDCS	110
III	DEPENDENCE OF THE TOTAL MICELLE DIAMETER (D_{TOTAL}), CORE DIAMETER (D_{CORE}) AND PEG CORONA DIAMETER (D_{PEG}) BASED ON AGGREGATION NUMBER (N_{AGG}) AND MONOMER TYPE. THESE VALUES ARE OBTAINED BY ANGULAR AVERAGING ($10 - 12$ NS) OF THE RADIAL EXTENSIONS OF THE PEG CHAINS WITH RESPECT TO THE MICELLE CENTER OF MASS.	118

LIST OF FIGURES

FIGURE		PAGE
1	Internal coordinates for bonded interactions: b describes bond stretching; θ represents the bond angle term; ϕ gives the dihedral angle; the small out-of-plane angle α is given by the "improper" dihedral angle ϕ.	19
2	Side view on two water nanodroplets, each with $N_w = 1300$ molecules, adsorbed on the opposite sides of a graphene sheet. The nanodroplets create two shallow holes in the graphene. Eventually, the nanodroplets become adjacent but stay highly mobile. Their dynamical coupling is realized by the minimization of the graphene bending energy associated with the two holes.	38
3	(a-d) Water nanodroplet activated and guided folding of two graphene flakes connected by a narrow bridge. The nanodroplet is squeezed away when the system is heated to $T = 400$ K. (e-h) Nanodroplet assisted folding of a star-shaped graphene flake, resembling the action of a "meat-eating flower".	39
4	Folding and sliding of a graphene ribbon with the size of 30×2 nm^2, which is activated and guided by a nanodroplet with $N_w = 1300$ waters and the radius of $R_d \approx 2.1$ nm. (a-c) The free ribbon end folds around the droplet into a knot structure that slides on the ribbon surface (d-e).	42
5	Folding and rolling of a graphene ribbon with the size of 90×2 nm^2, which is activated and guided by a nanodroplet with $N_w = 1,0000$ waters and the radius of $R_d \approx 4.2$ nm. (a-b) The ribbon tip folds around the water droplet into a wrapped cylinder, and (c-e) the wrapped cylinder is induced to roll on the ribbon surface (c-e).	43
6	The phase diagram of a nanodroplet and graphene nanoribbon with different folding dynamics. We display the nonfolding, sliding, rolling and zipping phases.	46
7	Folding and zipping of a graphene ribbon with the size of 60×16 nm^2, which is activated and guided by a nanodroplet with $N_w = 17,000$ waters and the radius of $R_d \approx 5$ nm. (a-b) The ribbon end folds around the droplet. (c-d) The zipping propagates along the ribbon until the fixed end, while water channel is formed in the graphene sleeve.	48

LIST OF FIGURES (Continued)

FIGURE		PAGE
8	Binding modes of graphene rings based on a ribbon with the size of 30×2 nm^2, inside water droplets. (a) The stable "capping" configuration of a hydrophobic ring with $N_w = 10,000$ waters. (b) The metastable "locking" configuration of a hydrophilic ring with $N_w = 18,000$ waters.	49
9	Rolling of a *GNR* (40×3 nm^2) on a (60,0) *CNT* when placed close to the *CNT* perpendicular to its axis.	54
10	(a-c) Helical rolling of a *GNR* (40×2 nm^2) when placed at the angle of $\varphi = 60^\circ$ with respect to the axis of the $l = 20$ nm (60,0) *CNT*. (d-e) The same when this *GNR* is placed inside this *CNT* (front part of the *CNT* is removed for better visualization). (f) The final structure of two *GNRs* (40×1 nm^2) when placed inside this *CNT*	55
11	Phase diagrams of *GNRs* of the width w self-assembled on long *CNTs* of the diameter D_C, shown for different initial angles φ with respect to the *CNT* axis. The *GNRs* self-assemble into nanostructures called the (A) straight, (B) nonfolding, (C) rolling, and (D) helical phases.	57
12	(a) Helical locked *GNR* (40×3 nm^2) inside a (60,0) *CNT*. (b) The same outside this *CNT* and detail of the locked structures. (c) Loosely helical folded *GNR* (60×1 nm^2) when it is placed inside the $l_C = 50$ nm long (60,0) *CNT*. (d) Two *GNRs* (25×2 nm^2) helical folded and *vdW* coupled over the wall of the (60,0) *CNT* (front parts of all the *CNTs* and *GNRs* (a-b) are removed for better visualization).	63
13	Graphene rings and knot formations from structured graphene flakes self-assembled on the *CNT* surface. (a-c) The formation of multiple *GNR* rings, covered with a single layer graphene sheet, on the (20,0) *CNT*. (d-e) After removal of the *CNT*, the multi-ring structure, covered with a single layer graphene sheet, is stabilized. (f) When the (20,0) *CNT* is placed between two connected *GNRs* a complex knot is formed.	66
14	Binding of *CNTs* and polyethylene by graphene nanoribbons. (a) Top view and (b) side view of two crossed *CNTs* (20,0), tied by a 60×2 nm^2 *GNR*. (c-d) Polyethylene chains wrapped by a (40×2 nm^2) *GNR*. (e-f) Helical rolling of a *GNR* (20×2 nm^2) when placed at the angle of $\varphi = 60^\circ$ with respect to the axis of the $l = 15$ nm (30,0) *CNT* in hexane (front part of solvent is removed for better visualization).	68

FIGURE		PAGE
15	Controlled self-assembly of hydrated double-headed lipid micelles filled with hexadecane. (a) Lipids deposited on the CNT form random hemimicelles after 20 ns. (b-d) Micelles with kinetically controlled sizes and filling are sequentially formed at the CNT tip when the hexadecane molecules in the CNT interior are pressurized and the lipids on its surface are dragged by the water flowing around it. The inset shows a single biheaded lipid molecule. Color scheme: red, CG hexadecane; gray, hydrophilic lipid head; cyan, hydrophobic lipid tail. (e) Three hexadecane-filled micelles from (d) after 400 ns of equilibration. (f) Thermodynamically driven self-assembly of double-headed lipid monomers and hexadecane in water for the same system as in (d). After 300 ns of equilibration, the sizes of the micelles and their filling are largely random.	73
16	Controlled self-assembly of hydrated single-headed lipid bicelles filled with hexadecane. (a) Lipids deposited on the CNT form random tubular structures after 20 ns. (b-d) Bicelles with kinetically controlled sizes and filling are sequentially formed at the CNT tip when the hexadecane molecules in the CNT interior are pressurized and the lipids on its surface are dragged by the water flowing around it. The inset shows single single-headed lipid molecule. Color scheme: red, CG hexadecane; gray, hydrophilic lipid head; cyan, hydrophobic lipid tail. (e) Hexadecane-filled bicelle from (d) after 375 ns of equilibration. (f) Thermodynamically driven self-assembly of single-headed lipid monomers and hexadecane in water for the same system as in (d). After 450 ns of equilibration, the sizes of the micelles and their filling are largely random.	78
17	Number of water molecules present within 0.5 nm (first monolayer) of the hydrophobic micelle core during the self-assembly of hydrated double-headed (red) and single-headed (blue) lipid monomers into micelles filled with hexadecane. The inset shows different forms of one micelle selected from the system of self-assembling single-headed lipid monomers. . . .	79
18	Condensation of 40,000 water molecules from an oversaturated vapor into a (28,28) PCNT: (a) $t = 1$ ns, (b) 6 ns, and (c) 10 ns. At $t = 10$ ns, a pressure of $P \approx 156$ atm is applied to water at the left PCNT entrance, causing the absorbed water to flow through the tube with a speed of $v_w \approx 1.86$ nm/ns, as shown in (d) at $t = 14$ ns. The droplet adsorbed onto the PCNT moves with the flow with its own velocity of $v_d \approx 0.88$ nm/ns.	85

LIST OF FIGURES (Continued)

FIGURE **PAGE**

19 The total change in energy when a water nanodroplet ($d_w \approx 6$ nm) enters inside a (40,40) PCNT through a single pore ($d_p \approx 1.5$ nm). Here, w is the relative amount of water inside the CNT. 87

20 Separation of Cl^- and Na^+ ions from the 0.2 M NaCl solution using oppositely charged (± 0.02 e per carbon atom or ± 50.8 e per tube) (20,20) PCNTs, 10 nm in length, at $T = 300$ K. 89

21 (top) Separation of the (1:1) benzene-ethanol mixture at $T = 300$ K with the (20,20), (28,28), and (40,40) PCNTs having $d_p \approx 1$ nm nanopores. (middle) The same in the (20,20) PCNT at different temperatures. (inset) The distribution of benzene (dark) and ethanol inside (20,20) PCNT after $t = 20$ ns of simulations. (bottom) Separation of the (1:1), (1:2), (2:1) benzene-ethanol mixtures in the (20,20) PCNT at $T = 300$ K. (inset) Separation of benzene from the benzene-ethanol (1:1) binary mixture at $T = 300$ K using a (20,20) PCNT membrane. Vertical arrows show direction of flow. 91

22 Schematic diagram of preparation of a nanomicelle from PEGylated DCs, synthesized through click chemistry between PCL and G3 dendron, followed by mPEG conjugation. The synthesis and experimental analyses were performed in Prof. Hong's laboratory. 97

23 (a) Linear relationship between CMC and HLB for PDCs and linear-block copolymers. Additional data points for the linear-block copolymers (empty symbols) were acquired from the literature that used the same polymer blocks. Note that, at the same HLB ($10 - 15$), the PDC self-assemblies maintain CMCs that are $1 - 2$ orders of magnitude lower than the linear counterparts, as highlighted in the shaded region. The data were obtained in Prof. Hong's laboratory. (b) MD simulations of (i) PCL3.5K-mPEG2K, (ii) PCL3.5K-mPEG16K, (iii) PCL3.5K-G3-mPEG2K, and (iv) PCL14K-G3-mPEG2K molecules after 5 ns in water (PCL: blue, G3-dendron: yellow, PEG: red). Water is not shown for clarity. 98

LIST OF FIGURES (Continued)

FIGURE **PAGE**

24 (a) TEM images of micelles self-assembled from PDCs obtained in Prof. Hong's laboratory: (i) PCL3.5K-G3-mPEG2K, (ii) PCL3.5K-G3-mPEG5K, (iii) PCL14K-G3-mPEG2K, (iv) PCL14K-G3-mPEG5K; and from the linear copolymers : (v) PCL3.5K-mPEG2K, (vi) PCL3.5K-mPEG5K, and (vii) PCL14K-mPEG5K. Scale bar = 100 nm. (b) MD simulations of micellar structures formed from (i) 128 PCL3.5K-mPEG2K, (ii) 14 PCL3.5K-G3-mPEG2K, and (iii) 10 PCL14K-G3-mPEG2K (PCL: blue, G3-dendron: yellow, PEG: red). Water is not shown. 105

25 Characterization of surface-modified dendron micelles. (A) Hydrodynamic diameter measurements of dendron micelles using dynamic light scattering. (B) Zeta potential (ZP) values measured in ddH_2O (pH 5.6) and critical micelle concentration (CMC) of dendron micelles measured in ddH_2O and PBS (pH 7.4). Transmission electron micrographs of dendron micelles comprised of (C) PDC-NH_2, (D) PDC-COOH, (E) PDC-Ac, and (F) PDC-OMe. Scale bar: 50 nm. 113

26 Atomistic molecular dynamics simulations of the dendron -NH_3^+ micelle in water. Black arrows indicate hydrogen bonding (yellow bonds) between hydrogens (gold balls) present on the terminal amine group (blue ball; identified by a blue arrow) with the oxygen atoms (red balls) present on the PEG chain. The hydrogen bond cutoff distance is 2.75 Å. We expect to observe intra- as well as intermolecular hydrogen bond formation within the micelle. Water is not shown for clarity. 117

27 Scanning of F^- (left) and Na^+ (right) ions coupled to coronene, evaluated at $h = 2$ Å (for F^-) and 2.5 Å (for Na^+) above its surface. The potential energy surface for (a) F^- ($\alpha = -1009.60$ au and $\beta = -1009.64$ au) and (d) Na^+ ($\alpha = -1077.97$ au and $\beta = -1078.06$ au). The charge transfer surface for (b) F^- ($\alpha = -0.65$ and $\beta = -1$) and (e) Na^+ ($\alpha = 1$ and $\beta = 0.8$). The dynamics of (c) F^- released at $h = 4$ Å ($T = 100$ K) and (f) Na^+ released at $h = 3.5$ Å above the coronene flake ($T = 300$ K). The flakes are shown for the last simulation frame, where atoms are colored by charge. The pixel density is 0.5 Å. (a-f) have the same scale. 123

LIST OF FIGURES (Continued)

FIGURE **PAGE**

28 Sanning of F^- ion coupled to zigzag-edge (left) and armchair-edge (right) triangular graphene flakes, evaluated at $h = 2$ Å above their surfaces. The potential energy surface for (a) zigzag ($\alpha = -1841.36$ au and $\beta = -1841.54$ au) and (d) armchair ($\alpha = -1464.97$ au and $\beta = -1465.04$ au) flakes. The charge transfer surface for (b) zigzag ($\alpha = -0.45$ and $\beta = -0.95$) and (e) armchair ($\alpha = -0.65$ and $\beta = -1$) flakes. The structure and dynamics of (c) zigzag flake after 1 ps simulations with F^- released at $h = 4.8$ Å and (f) armchair flake in 0.4 ps simulations where F^- released at $h = 3.6$ Å. The covalent coupling formed is seen in both cases. 126

29 Scanning of Cl^- (left) and Li^+ (right) above coronene (left set), and armchair-edge triangular H-passivated graphene flake (right set) at $h = 2$ Å (Cl^-) and 2.5 Å (Li^+) above the surface of each molecule. Potential energy surface for (a) Cl^- ($\alpha = -1374.94$ au and $\beta = -1375.1$ au) and (c) Li^+ ($\alpha = -924.13$ au and $\beta = -924.22$ au). Charge distribution surface for (b) Cl^- ($\alpha = -0.3$ and $\beta = -1.0$) and (d) Li^+ ($\alpha = 1.0$ and $\beta = 0.78$). Potential energy surface for (e) Cl^- ($\alpha = -1833.364$ au and $\beta = -1833.54$ au) and (g) Li^+ ($\alpha = -1382.57$ au and $\beta = -1382.66$ au). Charge distribution surface for (f) Cl^- ($\alpha = -0.3$ and $\beta = -1.0$) and (d) Li^+ ($\alpha = 0.92$ and $\beta = 0.76$). 127

30 Scans of F^- (left) at $h = 2$ Å and Na^+ (right) at $h = 2.5$ Å above a rectangular H-passivated flake with a nanopore of the diameter ≈ 8.25 Å. Potential energy surface for (a) F^- ($\alpha = -4872.68$ au and $\beta = -4872.86$ au) and (d) Na^+ ($\alpha = -4934.58$ au and $\beta = -4934.70$ au). The charge transfer surface for (b) F^- ($\alpha = -0.45$ and $\beta = -1$) and (e) Na^+ ($\alpha = 1$ and $\beta = 0.2$). (c) The porous rectangular flake with atoms colored by charge. (f) Scanned calculations for a regular rectangular flake with F^-; (top left) potential energy surface ($\alpha = -3200.94$ au and $\beta = -3201.05$ au); (top right) charge transfer surface ($\alpha = -0.45$ and $\beta = -0.95$); (bottom) the rectangular flake with covalently bonded F^- at the edge, obtained after 1.5 ps quantum MD simulation at $T = 300$ K (F^- released at $h \approx 6$ Å above the center of the flake). 130

31 Scanning of Na^+ around the base of the zigzag-edge triangular H-passivated flake shown in Figure 28c (two basal layers of C rings are visualized from the structure). (a) The potential energy surface ($\alpha = -1915.39$ au and $\beta = -1915.47$ au) and (b) the charge transfer surface ($\alpha = 1.1$ and $\beta = 0.4$) are calculated in a U-shaped pixel arrangement around the flake (here, the pixel density is 0.25 Å). 131

FIGURE **PAGE**

32 Self-assembly of carbon atoms at different temperatures (a–c at $T = 3,000$ K; d–e at $T = 2,000$ K; g–i at $T = 1,000$ K; j–l at $T = 500$K; most dominant structures are shown). 512 carbon atoms are placed in a cubic box ($500 \times 500 \times 500$ Å^3; atom density, $\rho = 4.1 \times 10^{-6}$ Å^{-3}). a) Formation of planar clusters (six member rings are well observed) within 10 ns. b) Fullerene type and big planar cluster with six and five member rings are observed after 25 ns. c) Almost all carbon atoms form fullerene type clusters ($C_{70} - C_{84}$) within 50 ns. d) Planar structures are formed within 25 ns. e) Formation of cage like structures with five and six member rings are observed after 50 ns. f) Cylindrical clusters, due to the merger of small fullerene type clusters, are found within 75 ns. g) Long chains emerge from short chains and eventually large member rings structures are observed (snapshot taken at 50 ns). h) Several large member rings form cage like structures (snapshot taken at 100 ns). i) Formation of five and six member rings are observed after 200 ns. j)Long chains molecules are observed within 50 ns. k) Large member rings emerge from long chains after 100 ns. l) Planar clusters, with big rings, are found after 200 ns. 141

33 Self-assembly of carbon atoms to small linear or branched chains at different temperature. The analytic dependence is t(ns)$= 23,153\ \mathrm{T}^{-1.10}$(K). 142

34 Formation of Carbon-hydrogen clusters (most dominant structures were shown, snapshots taken at 200 ns). 256 carbon atoms and 256 hydrogen atoms were placed in cubic box ($500 \times 500 \times 500$ Å^3). a) Short unsaturated chain and branched molecules, terminated with hydrogen atoms, were formed at $T = 500$ K. b) Planar clusters, terminated with hydrogen atoms, were observed at $T = 1,000$ K. c) At $T = 2,000$ K, fullerene like clusters, with some hydrogen atoms attached to surface, were found. . 145

FIGURE **PAGE**

35 Carbon inflow at $T = 1,750$ K. 100 carbon atoms are placed in a cubic box ($150 \times 150 \times 150$ Å^3). a) Formation of planar cluster with few six and five member rings is observed; snapshot taken at 10 ns. b) Bend cluster, with of six and five member rings, is observed after 20 ns. c) More bend structure, with all five and six member rings, is formed after 30 ns (note that some C-C bonds are missing for b and c; this is due to the fact, some part of these structures are in other periodic boxes and VMD (visualization software) can not draw bonds in such situations). d)Formation of planar cluster after 10 ns, where 20 carbon atoms are added after 10 ns simulation of 100 carbon atoms(a). e)Formation of even bigger planar cluster after 10 ns, where another 20 carbon atoms are added after 10 ns simulation of 120 carbon atoms(d). 146

36 Probability distribuition of carbon clusters (based on atom numbers in each cluster). (top) Simulated and gamma (blue; $\alpha = 2.3902$ and $\theta = 2.6447$) probability distributions of formed cluster sizes with $4,100$ carbon atoms (atom density, $\rho = 4.0 \times 10^-6$ Å^{-3}) at 500 K. (bottom) Simulated and gamma (blue; $\alpha = 1.4441$ and $\theta = 5.3347$) probability distributions of cluster sizes with $10,000$ carbon atoms (atom density, $\rho = 4.0 \times 10^-6$ Å^{-3}). The bin size is 25 carbon atoms. The snapshots are taken at 200 ns. 148

37 Probability distribuition of carbon clusters (based on atom numbers in each cluster). (top) Simulated and gamma (blue; $\alpha = 2.0007$ and $\theta = 2.6959$) probability distributions of formed cluster sizes with $4,100$ carbon atoms (atom density, $\rho = 4.0 \times 10^-6$ Å^{-3}) at $1,000$ K. (bottom) Simulated and gamma (blue; $\alpha = 1.4342$ and $\theta = 3.7367$) probability distributions of cluster sizes, with $10,000$ carbon atoms (atom density, $\rho = 4.0 \times 10^-6$ Å^{-3}) at $1,000$ K. The bin size is 25 carbon atoms. Snapshot taken at 100 ns. 149

38 Probability distribuition of carbon clusters (based on atom numbers in each cluster). (top) Simulated and gamma (blue; $\alpha = 1.0832$ and $\theta = 3.177804$) probability distributions of obtained cluster sizes, when $4,100$ carbon atoms (atom density, $\rho = 4.0 \times 10^-6$ Å^{-3}) are simulated at $2,000$ K (snapshot taken at 50 ns). (bottom) Simulated and gamma (blue; $\alpha = 0.7571$ and $\theta = 2.5915$) probability distributions of obtained cluster sizes, when $4,100$ carbon atoms (atom density, $\rho = 4.0 \times 10^-6$ Å^{-3}) are simulated at $3,000$ K (snapshot taken at 40 ns). The bin size is 25 carbon atoms. 150

LIST OF ABBREVIATIONS

AFM	Atomic Force Microscopy
AIMD	*ab initio* Molecular Dynamics
AIREBO	Adaptive Intermolecular Reactive Empirical Bond-order
AMBER	Assisted Model Building with Energy Refinement
BNT	Boron-Nitride Nanotube
CG	Coarse Grained
CHARMM	Chemistry at HARvard Macromolecular Mechanics
CMC	Critical Micelle Concentration
CNT	Carbon Nanotube
CSF	Configuration State Function
DC	Dendron Coil
DEAE	Diethylaminoethyl
DFT	Density Functional Theory
DIB	Diffuse Interstellar Band
DLS	Dynamic Light Scattering
ERE	Extended Red Emission
GGA	Generalized Gradient Approximation

LIST OF ABBREVIATIONS (Continued)

GNR	Graphene Nanoribbon
GROMACS	GROningen MAchine for Chemical Simulations
HF	Hartree Fock
HLB	Hydrophilic-Lipophilic Balance
ISM	Interstellar Medium
LAMMPS	Large-scale Atomic/Molecular Massively Parallel Simulator
LBC	Linearblock Copolymer
LDA	Local-density Approximation
MD	Molecular Dynamics
MM	Molecular Mechanics
NAMD	NAnoscale Molecular Dynamics
NP	Nanoparticle
OPLS	Optimized Potentials for Liquid Simulations
PAH	Polycyclic Aromatic Hydrocarbon
PAMAM	Poly(amidoamine)
PBC	Periodic Boundary Conditions
PBS	Phosphate Buffer Saline
PCL	poly(ϵ-caprolactone)

LIST OF ABBREVIATIONS (Continued)

PCNT	Porous Carbon Nanotube
PDC	PEGylated Dendron Coils
PEG	Polyethylene Glycol
PEI	Polyethylenimine
PER	PERiodic
PES	Potential Energy Surface
PLL	Poly(L-lysine)
PME	Particle Mesh Ewald
REBO	Reactive Empirical Bond-order
RHF	Restricted Hartree Fock
STM	Scanning Tunneling Microscopy
TEM	Transmission Electron Microscopy
vdW	van der Waals
VMD	Visual Molecular Dynamics

SUMMARY

In this thesis, we have studied by multiscale computational methods the atomic and molecular self-assembly, leading to complex and functionalized nanostructures. The thesis is based on 6 original papers, 1 review paper, 2 proceedings papers, and 2 manuscripts which are currently either submitted or in preparation.

In the first part of the thesis, we have used classical molecular dynamics simulations to show how to activate and guide the folding of planar graphene nanostructures. We have described how water nanodroplets and carbon nanotubes can induce bending, folding, sliding, and rolling of the nanostructures. We have investigated the self-assembly conditions and analyzed the stability of the formed nanosystems, with numerous possible applications.

In the second part of the thesis, we have investigated selected nanofludic applications of carbon nanotubes (CNT). We have used coarse-grained molecular dynamics (CGMD) to show that hydrated lipid micelles of preferred sizes and amounts of filling with hydrophobic molecules can be self-assembled on the surfaces of CNTs. We have shown that porous carbon nanotubes (PCNTs) can be used in selective molecular absorption, transport, and separation.

In the third part of the thesis, we have modeled nanomedicines based on the self-assembled micelles formed by highly PEG-ylated linear and branched (dendron-based) polymers by classical molecular dynamics simulations. In close collaboration with the experimental group of Prof. Seungpyo Hong, we have characterized physical properties of the self-assembled micellar

aggregates. We have identified how different chemical and physical factors contribute to the stabilization of the micelles and their interactions with cellular membranes.

In the fourth part of the thesis, we have studied the dynamics of ion binding to graphene nanostructures. We have shown that anions are either physisorbed onto the nanostructures or covalently bound at their selected regions, depending on the initial conditions, while cations only physisorb onto the nanostructures. Finally, we have described the self-assembly of carbon and hydrogen atoms in gas phases by reactive molecular dynamics methods. The dependence of temperatures and density of carbon atoms on clusters formation are investigated.

CHAPTER 1

INTRODUCTION

1.1 Computational modeling of nanoscale systems

In the last two decades, we experienced a revolutionary growth in technologies which allowed us to study various physical and chemical phenomena in unprecedented details at all scales. With the development of experimental equipments and techniques, such as scanning tunneling microscopy (STM) [1], atomic force microscopy (AFM) [2], optical tweezers [3], and others, we can now directly probe atoms ($0.1 - 0.2$ nm in size) [4], molecules [5], and composite nanoscale objects ($0.2 - 1000$ nm in size), and investigate the events occurring in single molecules in real time. With these methods, the mechanical, electronic, and optical properties of single molecules can be investigated [6–8]. All these experimental developments allow the manipulation of matter in a controllable and largely reproducible way.

Nanostructures of various sizes and shapes, such as semiconductor nanocrystals, quantum dots, and nanowires have been synthesized and characterized [9–11]. These nanoparticles are often functionalized and used in bio-sensing, active material coating, cosmetics, and numerous other areas [12–15]. For example, they can be used as potential building blocks in the preparation of periodic superstructures, which could significantly extend the applications of these novel materials in energy production and transportation. Carbon-based nanomaterials, such as

fullerenes, nanotubes and one-atom-thick graphenes [16–18], have also been synthesized and extensively studied for their unique chemical, physical, and electronic properties [19].

Despite the remarkable advances in all the experimental techniques, fabrication and manipulation of nanoscale objects scale are difficult. The experiments also can not provide all the information necessary for understanding of the physical and chemical phenomena. As noted in the justification for the 2013 Nobel Prize award to theoretical chemists, experiment does not tell "the story in between". Thus, theory and computational modeling are important for detailed understanding of phenomena in nanoscale systems.

In these days, we often need to study systems over many spatial regimes and timescales which necessitate using diverse theoretical approaches. For example, processes in a biological cells can last many different timescales and they are present in related length scales. In order to deal with all the issues, a variety of computational methods have been developed to accurately describe different properties of nanoscale systems, such as *ab-initio* methods, Monte Carlo, all-atom and coarse-grained molecular dynamics. Multiscale modeling methods, combining several different approaches, have also been developed to simulate complex phenomena.

With the introduction of massive supercomputers, development of new algorithms and methods, we can study much larger and complex systems (for example, MD simulation of HIV-1 virus capsid (64×10^6 atoms) [20]). These novel computational tools provide a platform for designing and optimizing new nanoconstructs, observing their dynamics in realistic environments, and testing of new hypotheses.

In this thesis, first, we study how molecules and molecular aggregates can activate and control the self-assembly of nanostructures. Then, we investigate the self-assembly of lipids and PEGylated dendrimers in water. We also describe the nanofludic properties of porous carbon nanotubes (PCNTs) and show that PCNTs can be used as molecular sieves. Next, we model the dynamics of ion-binding to graphene nanostructures in vacuum and in water. Finally, we describe the nucleation of long chains, clusters and complex cage structures in carbon and/or hydrogen gas phases.

1.2 Thesis structure

In chapter 2, we review computational methods relevant to the conducted research. First, we show how molecular systems can be described quantum mechanically. We outline the approximations which are used in the solution of Schrödinger equation in material systems. Then, we discuss the fundamentals of classical molecular dynamics methods. It is followed by the discussion of coarse-grained molecular dynamics methodologies. Next, hybrid QM/MM molecular dynamics methods are described. Finally, we discuss *ab-initio* molecular dynamics methods.

In Chapter 3, we show how water nanodroplets can activate and guide the folding of planar graphene nanostructures. First, we describe that nanodroplets can act as catalytic elements that initiate conformational changes in graphene ribbons and help to overcome deformation barriers associated with them. Finally, we show how nanodroplets can induce rapid bending, folding, sliding, rolling and zipping of the planar nanostructures, which can lead to the assembly of nanoscale sandwiches, capsules, knots and rings.

In Chapter 4, we present the self-assembly of planar graphene nanostructures on carbon nanotubes surfaces and in their interiors. First, we describe how nanotubes can induce bending, folding, sliding, and rolling of the nanostructures in vacuum and in the presence of solvent, leading to stable graphene rings, helices, and knots. Finally, we investigate the self-assembly conditions and analyze the stability of the formed nanosystems, with numerous possible applications.

In Chapter 5, we show that hydrated lipid micelles of preferred sizes and amounts of filling with hydrophobic molecules can be self-assembled on the surfaces of carbon nanotubes. First, we simulate micelle formation on a hydrated (40,0) carbon nanotube with an open end that is covered with amphiphilic double-headed or single-headed lipids and filled with hexadecane molecules. Then, we apply pressure on hexadecane molecules inside and drag the lipids on its surface by the water flowing around it. As a result, kinetically stable micelles filled with hexadecane molecules become sequentially formed at the nanotube tip. We investigate the stability of the formed kinetically stable filled micelles and compare them with thermodynamically stable filled micelles that were self-assembled in the solution.

In Chapter 6, we study nanofluidic properties of porous carbon nanotubes. We show that saturated water vapor, condensed on these nanotubes, can be absorbed by them and transported in their interior. We show that when the nanotubes are charged and placed in ionic solutions, they can selectively absorb ions and transport them within the tube. We also show that porous carbon nanotubes can also be used as selective molecular sieves, as illustrated on a room temperature separation of benzene and ethanol.

In Chapter 7 and 8, we present the self-assembly of linear and branched (dendron-based) PEG-ylated copolymers into micelles. In the experiments of Prof. Seungpyo Hong and our classical MD simulations, we analyze the effects of the dendron-based polymer architectures on the micelle self-assembly. By experimental methods and classical MD simulations, we measure micelle sizes, estimate their aggregation numbers, and characterize structure of different micelle regions.

In Chapters 9, we model the dynamics of ion binding to graphene nanostructures. First, we perform scanned single-point DFT calculations of monovalent ions (Na^+, Li^+, Cl^-, F^-) at fixed distances above planar graphene-like H-passivated molecules of different shapes and sizes to obtain potential energy surfaces. We correlate these static results with our room-temperature quantum MD simulations of the ion-molecule systems, performed in both vacuum and water. We show that anions either are physisorbed onto the nanostructures or covalently bind at their selected regions, depending on the initial conditions, while cations only physisorb onto them.

In Chapters 10, we describe the nucleation of long chains, large clusters, and complex cage structures in carbon and hydrogen rich interstellar gas phases. We study how temperature, particle density, presence of hydrogen, and carbon inflow affect the nucleation of molecular moieties with different characteristics. We determine the probability distributions of the sizes of carbon clusters at different temperatures for a particular carbon atom density.

CHAPTER 2

THEORY AND METHODS

2.1 Introduction

Over the past two decades, analytical modeling and computational simulation methods have been developed to deal with the complex nature of nanoscale systems. Multiscale methods based on quantum mechanical methods, all atom classical and coarse grained molecular dynamics methods can be used to design nanoscale materials, and predict and analyze their properties.

The modeling methods used depend on the studied properties, sizes of the systems and timescale of the phenomena which we want to describe. The chosen methods have to be "complex" enough to capture the underlying physics of the crucial phenomena, without oversimplifying the system properties. Quantum mechanical methods can be used to describe material systems accurately. Kohn-Sham density functional theory is one of the most used methods to describe the quantum properties of matter [21]. However, it is not feasible to use such quantum mechanical approaches for systems containing several hundred atoms. Such large systems can be well described by classical and semi-classical methods. Recent development of parallel processor supercomputers have led to a tremendous increase in computational power. All these theoretical and computational developments have been creating new opportunities for modeling and simulation of electronic and molecular properties of nanomaterials, as well as for designing novel nanomaterial devices.

In the following sections, we will discuss first-principle quantum mechanical methods used for electronic structure calculations. Then, we will discuss all-atom molecular dynamics methods. This will be followed by coarse-grained molecular dynamics methods used for simulations of bigger systems and longer timescales. Finally, we will discuss ab-intio molecular dynamics methods.

2.2 First-Principle Quantum Mechanical Methods

The time-dependent Schrödinger equation (SE) of a molecular system, containing M nuclei and N electrons can be written as:

$$i\hbar\frac{\partial\Psi(\vec{R},\vec{r},t)}{\partial t} = \hat{H}\Psi(\vec{R},\vec{r},t), \tag{2.1}$$

where $\hbar$ is the reduced Planck constant, $\hat{H}$ is the Hamiltonian operator of the system, $\Psi(\vec{R}, \vec{r}, t)$ is the time-dependent wavefunction, which depends on nuclear coordinates $\vec{R} = \vec{R}_1, ..., \vec{R}_M$ and electronic coordinates $\vec{r} = \vec{r}_1, ..., \vec{r}_N$.

The time-dependent equation (2.1) can be used to derive the time-independent Schrödinger equation of the studied system. When $\hat{H}$ is time-independent, we can write the wavefunction that solves Equation 2.1 in a separable form, as a product of spatial and temporal components, $\Psi(\vec{R},\vec{r},t) = \Phi(\vec{R},\vec{r})f(t)$. Then the system can be described by a time-independent Schrödinger equation:

$$\hat{H}\Phi_n(\vec{R},\vec{r}) = E_n\Phi_n(\vec{R},\vec{r}), \tag{2.2}$$

where $\Phi_n(\vec{R},\vec{r})$ are the eigenfunctions of the time-independent SE, and E_n are the related eigenvalues of the Hamiltonian, corresponding to the eigenfunctions $\Phi_n(\vec{R},\vec{r})$. When $\hat{H}$ is time-independent, the general solution of Equation 2.1 can be written as:

$$\Psi(\vec{R},\vec{r},t) = \sum_{n=1}^{P} \Psi_n(\vec{R},\vec{r},t) = \sum_{n=1}^{P} \alpha_n \Phi_n(\vec{R},\vec{r}) e^{-iE_n t/\hbar}, \tag{2.3}$$

where α_n are the expansion coefficients of the wavefunctions $\Phi_n(\vec{R},\vec{r})$.

2.3 Electronic Structure Calculations

Since nuclei are much heavier than electrons, we can introduce the Born-Oppenheimer (BO) approximation, according to which the electrons adjust *instantaneously* to much slower nuclear motions [22]. Within the BO approximation, the repulsion between the nuclei can be considered to be constant. Using BO approximation, we can decouple the electronic degrees of freedom from the nuclear degrees of freedom. Then the wavefunction of a molecule can be written as a product of separable nuclear and electronic wavefunctions:

$$\Phi(\vec{R},\vec{r}) = \psi_{nucl}(\vec{R})\psi_{el}(\vec{r};\vec{R}), \tag{2.4}$$

where the electronic motion depends explicitly on the electronic coordinates and parametrically on the nuclear coordinates $\vec{R}$ (i.e., for different arrangements of the nuclei, $\psi_{el}(\vec{r};\vec{R})$ is a different function of the electronic coordinates).

One of the main goals of computational quantum chemistry is to accurately solve for ground and excited electronic state wavefunctions for systems containing large numbers of

atoms. Typically, the computation of energies and electron distributions in multi-electron is done by wavefunction-based and density-functional-based methods. Below, we will discuss one wavefunction-based method and one density-functional-based method.

2.3.1 Exact Many-Electron Wavefunctions

In the BO approximation, the time-independent electronic SE for a system of N electrons can be written as:

$$\hat{H}_{el} \quad \psi_{exact}(\vec{r_1}, ..., \vec{r_N}) = E_{exact} \quad \psi_{exact}(\vec{r_1}, ..., \vec{r_N}), \tag{2.5}$$

where the electronic Hamiltonian of a system containing N electrons and M nuclei is given by:

$$\hat{H}_{el} = \sum_{i=1}^{N} \hat{T}_i + \sum_{p=1}^{M} \sum_{i=1}^{N} \hat{V}_{i,p} + \sum_{j=1}^{N} \sum_{i=1, i>j}^{N} \hat{V}_{i,j}, \tag{2.6}$$

where $\hat{T}_i$ is the single electron kinetic energy operator, $\hat{V}_{i,p}$ and $\hat{V}_{i,j}$ are electron-nucleus and electron-electron potential energy operators, for electrons i, j and nuclei p.

The exact solution of Equation 2.5 has the form of a linear combination of Slater determinants (configuration state functions (CSFs)) which form a complete set of a N-electron problem. The CSFs can be written as:

$$\psi_{exact} = \sum_{s1,s2,...,sl} c_{s1,s2,...,sN} \begin{vmatrix} \phi_{s1}(r_1) & \phi_{s2}(r_1) & ... & \phi_{sN}(r_1) \\ \phi_{s1}(r_2) & \phi_{s2}(r_2) & ... & \phi_{sN}(r_2) \\ & & ... & \\ \phi_{s1}(r_N) & \phi_{s2}(r_N) & ... & \phi_{sN}(r_N) \end{vmatrix}, \tag{2.7}$$

where $\phi_{si}(r_i)$ are one-electron spin orbitals, which are products of spatial orbital and spin functions, and ϕ_{si} belong to a *complete basis set* of one-electron spin orbitals [23]. Since the many-electron wavefunctions given in Equation 2.7 contains a very large (infinite) number of basis set functions and CSFs, it is not feasible to get an exact solution. The time-independent SE equation can be solved approximately by many different methods.

2.3.2 The Hartree-Fock Method

The Hartree Fock theory is one the simplest approximation method for solving the many-electron problem. In the Hartree approximation, we can write the many-electron wavefunction as a product of one electron wavefunctions:

$$\psi = \phi_{a,\alpha}(1)\phi_{a,\beta}(2)....\phi_{z,\beta}(N), \tag{2.8}$$

where electron 1 occupies molecular orbital ϕ_a with spin α, electron 2 occupies molecular orbital ϕ_a with spin β and so on. However, many electron wavefunctions must satisfy the Pauli principle and be antisymmetric with the exchange of electrons. This can be achieve by expressing the wavefunction of N electrons as a single Slater determinant:

$$\psi_{HF} = \frac{1}{\sqrt{N!}} \begin{vmatrix} \phi_{a,\alpha}(1) & \phi_{a,\beta}(1) & ... & \phi_{z,\beta}(1) \\ \phi_{a,\alpha}(2) & \phi_{a,\beta}(2) & ... & \phi_{z,\beta}(2) \\ & & ... & \\ \phi_{a,\alpha}(N) & \phi_{a,\beta}(N) & ... & \phi_{z,\beta}(N) \end{vmatrix}, \tag{2.9}$$

when this wavefunction is combined with the variation principle, the orbitals (corresponding to the lowest total energy) must satisfy the Hartree-Fock equation:

$$f_1 \phi_{a,\sigma}(1) = \epsilon \phi_{a,\sigma}(1), \tag{2.10}$$

where σ is either α or β. The Fock operator f_1 is given by

$$f_1 = h_1 + \sum_j \{2J_j(1) - K_j(1)\}, \tag{2.11}$$

here, the first term, the core Hamiltonian can be written as

$$h_1 = -\frac{\hbar^2}{2m_e}\nabla_1^2 + \sum_n \frac{Z_n e^2}{4\pi\epsilon_0 r_{ni}}, \tag{2.12}$$

the second term is the Coulomb operator

$$J_i(1)\phi_a(1) = \int \phi_j^*(2)\phi_j(2)\frac{e^2}{4\pi\epsilon_0 r_{12}}\phi_a(1)d\tau_2, \tag{2.13}$$

and the third term is the exchange operator

$$K_i(1)\phi_a(1) = \int \phi_j^*(2)\phi_a(2)\frac{e^2}{4\pi\epsilon_0 r_{12}}\phi_j(1)d\tau_2. \tag{2.14}$$

In the computational scheme, we first prepare a trial Slater determinant ψ_{HF} containing orbitals $\phi_{a,\sigma}(r)$ which are linear combinations of basis set functions $\chi(r)$ with trial coefficients k_i, $\phi_{a,\sigma}(r) = \sum_i k_i\chi(r)$. Next, we perform an *iterative* minimization process where we gradually minimize the energy E_{HF} with respect to the coefficients k_i. The HF method gives the best single SD solution, which minimizes the energy $E_{HF} = \langle\psi_{HF} \mid H_{el} \mid \psi_{HF}\rangle$ [23].

The variational procedure results in the total wavefunction which is constructed from one-electron wavefunctions that are optimized in the *average* potential, or *mean field*, of all the other electrons (and nuclei) (see Equation 2.10). In the HF approximation, the electron correlations based on the use of many SDs (see Equation 2.7) are neglected. A number of approaches have been developed to include electron correlations to the many-electron wavefunction. In multi-configuration self-consistent field and configuration interaction methods, the many-electron wave function is expressed in terms of a linear combination of multiple Slater determinants. In density functional theories, multi-electron problem is solved by using a single

SD wavefunction but incorporating the correlations in an effective Hamiltonian lacking electron interactions.

2.3.3 Density Functional Theory

The first Hohenberg-Kohn theorem demonstrates that the ground state (nondegenerate) properties of a many-electron system are uniquely determined by an electron probability density ($\rho_0(x, y, z)$) that depends on only 3 spatial coordinates [24]. It reduces the many-body problem of N electrons with $3N$ spatial coordinates to 3 spatial coordinates through the use of functionals of the electron density. This theorem has also been proved for degenerate ground states. The second HK theorem defines an energy functional for the system, such that the true ground state electron density minimizes this energy functional

Within the framework of Kohn-Sham DFT (KS DFT), the intractable many-body problem of interacting electrons is reduced to a tractable problem of non-interacting electrons moving in an effective potential. The effective potential includes the external potential and the effects of the Coulomb interactions between the electrons, e.g., the exchange and correlation interactions.

The electron density ($\rho_0(x, y, z)$) can be determined from a single-particle picture of non-interacting electrons [24]. The corresponding Hamiltonian for the single-particle KS orbitals ψ_i is expressed by the KS equations as [21]

$$H^{KS}\psi_i(r) = \Big[-\frac{1}{2}\nabla^2 + V_{eff}(r)\Big]\psi_i(r) = \epsilon_i\psi_i(r) \tag{2.15}$$

where the effective potential V_{eff} is

$$V_{eff}(r) = \int dr^{'} \frac{\rho(r^{'})}{\mid r - r^{'} \mid} + V_a(r, \{R_{i_a}\}) + \frac{\delta E_{xc}[\rho(r)]}{\delta \rho(r)}, \tag{2.16}$$

here, $V_{eff}(r)$ explicitly depends on the density $\rho(r) = \sum_{i_0}$ with the sum running over occupied KS orbitals. $V_a(r, \{R_{i_a}\})$ is the external potential due to the nuclei at positions $\{R_{i_a}\}$. The exchange-correlation term (E_{xc}) accounts for all many-body effects and can only be determined using approximation methods. Finally, the ground state energy of the interacting problem can be expressed as

$$E[\rho(r)] = T[\rho(r)] + \int dr \rho(r) V_a(r, \{R_{ia}\}) + \frac{1}{2} \int \int dr dr^{'} \frac{\rho(r)\rho(r^{'})}{\mid r - r^{'} \mid} + E_{xc}[\rho(r)] \tag{2.17}$$

where T is the kinetic energy corresponding to the density $\rho(r)$ (function of three coordinates). The KS equations (Equation 2.15) are solved by SCF methods: starting with an initial density, the effective potential (V_{eff}) is computed together with the KS orbitals and the corresponding density, and this procedure is repeated until the convergence has been reached.

The major problem with DFT is that the exact exchange-correlation functionals are not known. However, there are relatively well understood approaches how to obtain exchange-correlation functionals that are precise enough in many practical situations to describe quantum properties of matter. Local-density approximation (LDA) is one of the simplest approximations. LDA assumes that the density can be treated locally as a uniform electron gas. The exchange-correlation energy at each point in the system is the same as that of a uniform electron gas of

the same density. Using LDA approximation the exchange-correlation energy for a density $\rho(r)$ cane be expressed by

$$E_{xc}^{LDA} = \int \rho(r)\, \epsilon_{xc}(\rho) dr \tag{2.18}$$

where $\epsilon_{xc}(\rho)$ is the exchange-correlation energy per particle of a uniform electron gas of density ρ [25]. The LDA is based on the uniform-electron gas model, which is appropriate for a system where ρ varies slowly with position. LDA fails in situations where the density undergoes rapid changes such as in molecules. Generalized Gradient Approximation (GGA), where the gradient of the electron density is considered, can be used to overcome the shortcomings of LDA [26].

Hybrid Functional

Hybrid functionals are composed of exact an exchange term from the Hartree-Fock theory with exchange and correlation terms from other sources [25,27,28]. B3LYP (Becke, 3-parameter, Lee-Yang-Parr) is one of most commonly used hybrid functional to study biology and chemistry related problems.

The B3LYP exchange-correlation functional can be expressed as:

$$E_{xc}^{B3LYP} = E_{xc}^{LDA} + a_0(E_x^{HF} - E_x^{LDA}) + a_x(E_x^{GGA} - E_x^{LDA}) + a_c(E_c^{GGA} - E_c^{LDA}), \tag{2.19}$$

where $a_0 = 0.20$, $a_x = 0.72$, and $a_c = 0.81$. E_x^{GGA} is the Becke 88 generalized gradient approximation to the exchange functional [27]. E_c^{GGA} is the Lee, Yang and Parr generalized

gradient approximation to the correlation functional [25]. E_c^{LDA} is the VWN local-density approximation to the correlation functional [28].

2.4 Classical Molecular Dynamics Methods

We can describe a system classically when there are no chemical reactions involved in it. In such cases, the dynamics of system can be described by classical Newtonian motion of the nuclei of molecules/atoms. For a system of N atoms, Newton's equations of motion can be written as:

$$m_i \dot{\vec{v}_i} = -\frac{\partial}{\partial \vec{r}_i} V_{total}\,(\vec{r}_1, \vec{r}_2, \ldots \vec{r}_N), \qquad i = 1, 2 \ldots N \tag{2.20}$$

$$\dot{\vec{r}_i} = \vec{v_i}\,, \qquad i = 1, 2 \ldots N \tag{2.21}$$

where m_i, $\vec{r}_i$ and $\vec{v}_i$ are the mass, the coordinate and the velocity of the i-th atom, respectively. Thus, $6N$ ($3N$ coordinates, $3N$ velocities) first-order Newtonian differential equations can be used to describe the dynamics of the system.

Molecular dynamics (MD) simulations generate a phase space trajectory by integrating the Newton's equations of motion for a system of interacting particles. However, real systems are typically described by Langevin equations of motion, which include coupling to a thermostat (more details are discussed later). The trajectories of atoms and molecules are determined by numerically solving the equations of motion for a system of interacting particles, where forces between the particles and potential energy are defined by molecular mechanics force fields.

The results of molecular dynamics simulations may be used to determine macroscopic thermodynamic properties of the system based on the ergodic hypothesis: the statistical ensemble averages are equal to time averages of the system. For a successful MD simulation, we need robust and efficient numerical algorithms to solve the $6N$ Newtonian differential equations and potentials which describe the interactions between the atoms. In the following sections, we discuss the functional form of the force field, numerical integration and special considerations for studying statistical properties with MD simulations.

2.4.1 Force Field Functions

The force field is a set of functions and parameters that describe the potential energy of interacting atoms in molecules. In this thesis, we have used CHARMM force field [29], as implemented in the NAMD molecular dynamics package for all atom simulations [30]. The potential energy (V_{total}) contributions are the following:

$$V_{total} = V_{bond} + V_{angle} + V_{dihedral} + V_{vdW} + V_{Coulomb}\,. \tag{2.22}$$

The first three terms describe the bonded interactions (stretching, bending, and torsional bonded interactions),

$$V_{bond} = \sum_{bonds\ i} k_i^{bond} (b_i - b_{0i})^2 \tag{2.23}$$

$$V_{angle} = \sum_{angles\ i} k_i^{angle} (\theta_i - \theta_{0i})^2 \tag{2.24}$$

$$V_{dihedral} = \begin{cases} \sum_{dihedrals} k_i^{dihe} [1 + \cos(n_i \phi_i - \gamma_i)], \ n_i \neq 0 \\ \sum_{dihedrals} k_i^{dihe} (\phi_i - \gamma_i)^2, \ n_i = 0 \end{cases} \tag{2.25}$$

where k_i^{bond} and b_0 are bond constant and the minimum energy bond length of particular type, respectively. A harmonic potential function is used to describe the bond interactions. The *angles* are defined as the angles between each pair of covalent bonds sharing a single atom at the vertex, and V_{angle} is defined in the similar way as V_{bond}. The last term, *dihedral*, represents atom pairs separated by three covalent bonds with the central bond subject to the torsion angle ϕ, as shown in Figure 1. $V_{dihedral}$ can have multiple minima. The *improper* interactions has only one well defined minima ($n_i = 0$), as shown in Figure 1 (bottom).

The last two terms in (Equation 2.22) describe the nonbonded interactions between atom pairs:

$$V_{Coulomb} = \sum_i \sum_{j>i} \frac{q_i q_j}{4\pi\varepsilon_0 r_{ij}}\ , \tag{2.26}$$

$$V_{vdW} = \sum_i \sum_{j>i} 4\epsilon_{ij} \left\{ \left(\frac{\sigma_{ij}}{r_{ij}} \right)^{12} - \left(\frac{\sigma_{ij}}{r_{ij}} \right)^{6} \right\}, \tag{2.27}$$

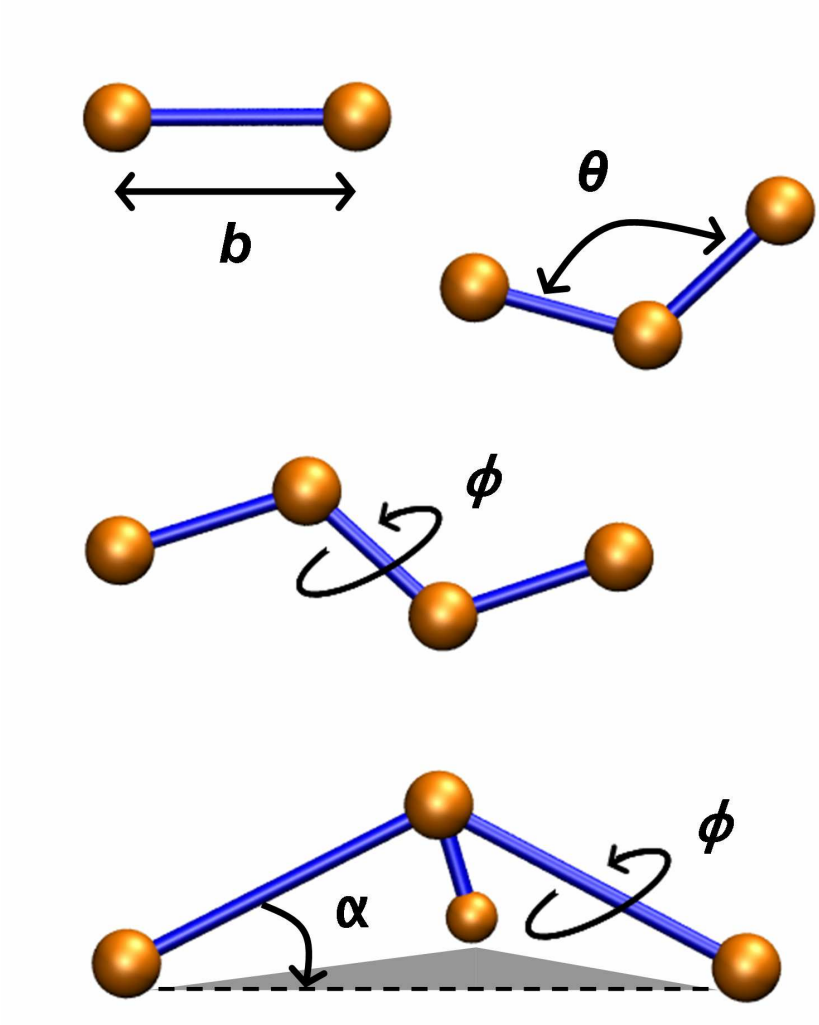

Figure 1. Internal coordinates for bonded interactions: b describes bond stretching; θ represents the bond angle term; ϕ gives the dihedral angle; the small out-of-plane angle α is given by the "improper" dihedral angle ϕ.

here, the first term represents electrostatic (Coulomb) interactions where ϵ_0 is the vacuum permittivity, q_i and q_j are partial atomic charges localized at atom centers, and r_{ij} is the distance between the atom centers. The PME method [31] is used to evaluate V_{Coul} for all the atoms with interatomic distances greater than the cut-off distance. PME is an efficient full electrostatics method for use with periodic boundary conditions.

The van der Waals interactions is approximated by a Lennard-Jones 12–6 potential. The strength of the interaction ϵ_{ij} and the minimum of the potential σ_{ij} are obtained from the parameters of atoms i and j, through the Lorentz-Berthelot mixing rules,

$$\epsilon_{ij} = \sqrt{\epsilon_i \, \epsilon_j} \ ,$$
$$\sigma_{ij} = \frac{1}{2}(\sigma_i + \sigma_j) \ .$$

The determination of these parameters for the interactions in Equation 2.23 - Equation 2.27 is a difficult task and generally it is accomplished through a combination of empirical techniques and quantum mechanical calculations. The force field is then validated and/or optimized by reproducing of structural, dynamic, and thermodynamic properties of small molecules or solvents which are well-characterized experimentally.

A large variety of force fields are available to describe different molecules including different solvents, lipids, peptides, nucleic acids, small organic drug molecules, etc. Force fields, such as CHARMM [29,32], AMBER [33], OPLS all-atom [34,35], GROMOS [36], have been successfully used to describe variety of experimental phenomena. It is important to note that in classical

force fields, the parameters remain constant throughout simulations. Therefore, no changes can occur in bonding between atoms.

2.4.2 Many-body Potentials

The classical MD simulation techniques are intended for modeling of physical processes, not chemical reactions. The formation and breaking of chemical bonds are inherently quantum mechanical processes, and need to be investigated by first-principles or like methods. There exist some classical potentials that can empirically model changes in covalent bonding. Tersoff-type [37,38] potentials are very successful for treating covalent bonding interactions in systems containing silicon, carbon, oxygen or hydrogens. One particularly successful example of a Tersoff-type potential is the reactive empirical bond-order (REBO) potential developed by Brenner [39].

In this thesis, we have used the adaptive intermolecular reactive empirical bond-order (AIREBO) potential proposed by Stuart [40], based on the Brenner bond-order potential [39], to describe the formation of carbon clusters. In AIREBO potential, nonbonding interactions and torsional potential for hindered rotation around single bonds are introduced, which are lacking in the REBO potential. This potential can be used for chemical reactions and intermolecular interactions in condensed-phase hydrocarbon systems such as liquids, graphite, and polymers. The AIREBO potential function can be written as:

$$
\begin{aligned}
E^{Total} &= E^{REBO} + E^{LJ} + E^{tors}\,, \qquad (2.28)\\
E^{REBO} &= V_{ij}^{R}(r_{ij}) + b_{ij}\, V_{ij}^{A}(r_{ij})\,,\\
E_{ij}^{LJ} &= S(t_r(r_{ij}))\, S(t_b(b_{ij}^{*}))\, C_{ij}\, V_{ij}^{LJ}(r_{ij}) + [1 - S((t_r(r_{ij})]\, C_{ij}\, V_{ij}^{LJ}(r_{ij}),
\end{aligned}
$$

where V_{ij}^{R} and V_{ij}^{A} are repulsive and attractive pairwise potentials between atoms i and j, separated by r_{ij}, and b_{ij} is the bond-order term in a Tersoff-type potential [40]. The dispersion and intermolecular interaction (E_{LJ}) are modeled with a Lennard-Jones (LJ) 12-6 potential, with universal switching function ($S(t)$) and connectivity switch (C_{ij}). $t_r(r_{ij})$ and $t_b(b_{ij})$ are both scaling functions.

The torsional potential (E^{tors}) is proportional to the bond weights (w_{ij}) that contribute to dihedral angles,

$$
E^{tors} = \frac{1}{2}\sum_{i}\sum_{j\neq i}\sum_{k\neq i}\sum_{l\neq i,j,k} w_{ij}(r_{ij})\, w_{jk}(r_{jk})\, w_{kl}(r_{kl})\, V^{tors}(\omega_{ijkl}). \qquad (2.29)
$$

The bond weights (w_{ij}) smoothly remove the torsional energy, associated with a given dihedral angle, as any of the constituent bonds are broken. The complete descriptions of the AIREBO potential could be found in Ref. [40].

2.4.3 Periodic Boundary Conditions

Typical experimental systems contain a large number of atoms. In atomistic MD simulations, we usually describe an ensemble of a much smaller number of particles. To eliminate edge effects, we introduce periodic boundary conditions where cubical simulation box is replicated throughout the space to form an infinite lattice. In the course of the simulations, when a molecule moves in the central box, its periodic image in other boxes moves with exactly the same orientation in exactly the same way. As the molecule leaves the central box, one of its images will enter through the opposite face. There are no walls at the boundary of the central box, and the system has no surface.

2.4.4 Numerical Integration Schemes

Finite difference methods are used to integrate the Newtonian or Langevin equations of motion. The velocity-Verlet method [41] is used for NVE ensemble simulations in the NAMD package. It obtains positions and velocities at the next time step $(\vec{r}_{n+1}, \vec{v_{n+1}})$ from the current step $(\vec{r}_n, \vec{v_n})$ assuming that forces $f_n = f(\vec{r}_n)$ are already computed:

$$
\begin{aligned}
\text{“half} - \text{kick”} \qquad & v_{n+1/2} = v_n + m^{-1} f_n \cdot \Delta t/2, \\
\text{“drift”} \qquad & r_{n+1} = r_n + v_{n+1/2} \Delta t, \\
\text{“compute force”} \qquad & f_{n+1} = f(r_{n+1}), \\
\text{“half} - \text{kick”} \qquad & v_{n+1} = v_{n+1/2} + m^{-1} f_{n+1} \cdot \Delta t/2.
\end{aligned}
$$

The velocity-verlet method is simplectic and time reversible. It conserves linear and angular momentum, and requires only one force evaluation for each time step. It exhibits a (global) energy error proportional to Δt^2 for a fixed time. Nevertheless, it is one of the simplectic and fastest algorithms for molecular dynamics of large systems.

2.4.5 Statistical Ensembles in MD Simulations

Statistical properties of a microscopic system can be characterized by ensembles. A statistical ensemble is composed of a large number of virtual copies of a system, considered all at once, each of which represents a possible microstate (one configuration of all the molecules) that the real system might be in. A statistical ensemble is a probability distribution for the (thermodynamic) state of the system.

Microcanonical Ensemble

In a *microcanonical* or NVE ensemble, the number of particles (N), volume (V) and energy (E) are constant. The NVE ensemble can be used to describe adiabatic processes with no heat exchange. In these cases, only Newtonian dynamics are allowed as the total energy must be conserved.

Canonical Ensemble

In a *canonical* or NVT ensemble, the number of particles (N), volume (V) and temperature (T) are constant. In NVT ensemble, the total energy is not conserved, as the energy is exchanged with a thermostat. In simulations using NVT ensembles, a variety of thermostat methods are available to add and remove energy from the simulated MD system and the coupling between

the thermostat and the system could be controlled. In the NAMD package, the Langevin dynamics or Nose-Hoover thermostat are used to couple the system to the reservoir [30].

Isothermal-Isobaric Ensemble

In a isothermal-isobaric ensemble, or NPT ensemble, the number of particles (N), pressure (P) and temperature (T) are constant, but volume (V) is allowed to change. In order to keep pressure constant, a barostat is needed in addition to the thermostat. These conditions resemble most closely real experimental environments. In NAMD, the Langevin piston method is used to model the barostat [42].

2.4.6 The Langevin Dynamics

The Langevin dynamics is an extension of the Newtonian dynamics to control the system temperature and its rate of energy dissipation to the reservoir. The Langevin equation can be written as:

$$\dot{\vec{v_i}} = \frac{\vec{f_i}\,(r_i)}{m_i} - \gamma \cdot \vec{v_i} + \sqrt{\frac{2\gamma k_B T}{m}} \cdot \vec{R}(t), \tag{2.30}$$

where, m_i is the mass of i-th particle, $\vec{v_i} = \dot{\vec{r_i}}$ is its velocity, $\vec{r_i}$ is its coordinate vector, $\vec{f_i}$ is the force, γ is the friction coefficient, k_B is the Boltzmann constant, T is the thermostat temperature, and $R(t)$ is a Gaussian random process.

The second (dissipative) term in Equation 2.30 represents a frictional damping that is applied to the particle. The third term represents random forces applied to the particle. The dynamics of the system depend on the strength of the coupling to the thermal reservoir γ. The dynamics of a *overdamped* ($\gamma > 10.0$ ps^{-1}) system are highly stochastic and far from Newtonian

dynamics, while the dynamics for a underdamped ($\gamma < 0.01$ ps^{-1}) system represent roughly the Newtonian motion but the thermalization is still achieved within tens of nanoseconds.

2.4.7 Simulation Parameters

Time step

In MD simulations the time step should be at least an order of magnitude smaller than the characteristic time of the fastest motion in the simulated system. In our all atom MD simulation studies, the fastest motion is the C-H bond stretching (≈ 10 fs). Therefore, the time step is chosen to be $1 - 2$ fs.

Cutoff

In NAMD, van der Waals and electrostatic interactions are always truncated at the cutoff distance, specified by *cutoff*. In our MD simulations, the cutoff distance is 1.2 nm.

Switching and Switchdist

When the switching is turned on, then smoothing functions are applied to both the electrostatics and van der Waals forces. The switchdist specifies the distance at which the switching function should begin to take effect. The value of switchdist must be smaller than or equal to the cutoff value, since the switching function is only applied in the range from switchdist to cutoff. In our MD simulations, we use 1.0 nm as a switching distance.

Particle Mesh Ewald (PME)

PME method [31] is used to evaluate V_{Coul} for all the atoms with interatomic distances greater than the cut-off distance. PME method is an efficient full electrostatics method for use with periodic boundary conditions.

In our classical atomistic MD simulations, we use the NAMD simulation code [30]. NAMD is a highly parallel molecular dynamics code designed to run on modern high-end supercomputers with thousands of processors. There are other MD softwares available, such as CHARMM [29], AMBER [33], and GROMACS [36]. We use Visual Molecular Dynamics (VMD) software [43] for analysis and visualization.

2.5 Coarse-Grained Molecular Dynamics

All-atom MD simulations can reveal in atomistic details the system dynamics. However, all-atom MD simulations are typically restricted to relatively small systems and short timescales [30]. In order to study very large systems, one can use coarse-grained methods [44–49]. Here, we use Marrink's CG model-MARTINI 2.0 [50, 51]. The building blocks of the coarse grained force field are extensively calibrated against thermodynamic data, in particular oil/water partitioning coefficients. In MARTINI 2.0 model, a four-to-one atom mapping is used to represent molecules in a simplified way. On average, four heavy atoms are represented by a single interaction center (CG bead). For ring structures a different mapping (two-to-one or three-to-one) is introduced. As the size and mass of the hydrogen atoms are small, hydrogens are not considered at all [50].

The MARTINI 2.0 model considers only four main types of interaction sites: polar (P), nonpolar (N), apolar (C), and charged (Q). For a more accurate representation of the chemical nature of the underlying atomic structure, each particle type is divided into several subtypes. Within a main type, subtypes are divided into four categories (denoted by letter) based on the hydrogen-bonding capabilities (d = donor, a = acceptor, da = both, and 0 = none). The degree

of polarity is indicated by a number (from 1 = low polarity, to 5 = high polarity). In this way, the main chemical types and interactions between them are described.

2.5.1 Interactions between CG Particles

Although, the overall character of the interactions between the CG particles and the interactions between the atoms in all-atom molecular dynamics are very similar, there are many important differences in certain details. As the CG beads are composed of certain numbers of atoms, the parameters in the all-atom force field are modified significantly. CG interactions are described in detail in the following sections.

Nonbonded Interactions

The form of the CG interaction potentials are similar to all-atom model potentials. A shifted Lennard-Jones 12-6 potential is used to describe nonbonded pair interactions,

$$V_{vdW}(r) = 4\epsilon_{ij}\left\{\left(\frac{\sigma_{ij}}{r}\right)^{12} - \left(\frac{\sigma_{ij}}{r}\right)^{6}\right\}, \tag{2.31}$$

where σ_{ij} represents the equilibrium distance between two particles and ϵ_{ij} is the strength of their interaction. The effective size, $\sigma_{ij} = 0.47$ nm, is assumed for each interaction pair, except in a few special cases (see ring and antifreeze particles). The complete table of interactions could be found in Ref. [51].

The charge groups (type Q particles) bear full charges q_i and q_j, and the electrostatic interaction is described by a Coulombic potential

$$V_{el}(r) = \frac{q_i q_j}{4\pi\varepsilon_0\varepsilon_r r} \ , \tag{2.32}$$

with relative dielectric constant ϵ_r for explicit screening. To balance the the increased hydration strength of many of the CG particle types, the dielectric constant ϵ_r is reduced to 15. For small hydrated atoms (e.g., ions) a reduced charge is used to balance the effect of an implicit hydration shell.

Bonded Interactions

Harmonic potential (V_{bond}^{CG}) is used to describe the bonded interactions between chemically connected sites (similar to atomistic description Equation 2.23)

$$V_{bond}^{CG} = \frac{1}{2} K_{bond}^{CG} (b^{CG} - b_0^{CG})^2, \tag{2.33}$$

where the equilibrium distance b_0^{CG} is $b_0^{CG} = \sigma = 0.47$ nm and a force constant of $K_{bond}^{CG} = 1250$ kJ mol^{-1} nm^{-2}. The LJ interaction is excluded between bonded particles.

A weak harmonic potential $V_{angle}^{CG}(\theta)$ of the cosine type is used to represent the angles

$$V_{angle}^{CG}(\theta) = \frac{1}{2} K_{angle}^{CG} (\cos\theta^{CG} - \cos\theta_0^{CG})^2 \ . \tag{2.34}$$

For aliphatic chains, the force constant is $K_{angle}^{CG} = 25$ kJ mol^{-1} with an equilibrium bond angle of $\theta_0^{CG} = 180°$. For angles with a *cis* double bond involved, the force constant is set $K_{angle}^{CG} = 45$ kJ mol^{-1} and the equilibrium angle θ_0^{CG} equals to 120° [51]. LJ interactions between second nearest neighbors are not excluded.

Ring Particles

A four-to-one mapping procedure is inadequate to preserve the geometry of small ring compounds. Therefore, a two-to-one or three-to-one mapping is used to keep the ring geometry. As a consequence of the large density of CG beads, the interaction parameters for ring particles need to be modified. The σ of the LJ potential is changed to 0.43 rather than 0.47 nm and the ϵ is scaled to 75% of the original value. As a result the ring particles pack more closely without freezing, which allows reproduction of the liquid densities of small ring compounds while retaining the correct partitioning behavior.

Antifreeze Particles

The freezing temperature of CG water, modeled as P_4, is somewhat high compared to real water. The freezing process is nucleation limited which means that the CG water can remain fluidic for a very long time. But, once a nucleation site has formed at a low enough temperature, the water starts to freeze and the transition from a liquid state to a solid state is rapid and largely irreversible at the low temperature.

In order to prevent this freezing of CG water, we add antifreeze particles (modeled as BP_4). The LJ parameter σ for BP_4 - P_4 is increased to 0.57 nm to disturb the lattice packing of the uniformly sized solvent particles and the strength of the BP_4 - P_4 interaction is raised to level

"O" to avoid the phase separation between the antifreeze and solvent particles. The interactions of the BP_4 with any other type of particle, including the self-interaction, remain the same in the normal CG water.

2.5.2 Simulation Parameters

In order to account for the increased bead size, various parameters related to linear sizes of the systems have to be larger. The *cutoff* distance for vdW and Coulomb potentials is 10 Å and 14 Å in atomistic and CG simulations, respectively. The parameter *pairlistdist* is 12 Å and 16 Å for atomistic and CG simulations, respectively. As the distances between the beads are large and the used potential is smooth, bigger time steps can be used ($\approx$ 20 fs) for MD integrations (compare to 1 fs for atomistic simulations). Two- to six-fold speed-up of dynamics have been observed in CG simulations [51] compare to atomistic simulations. The combination of longer time steps and faster relaxation results in a *computational* speed-up of 50-150 times from an all-atom to a CG description.

2.6 Hybrid QM/MM Molecular Dynamics

Quantum mechanical (QM) methods are used to describe chemical reactions and other complex interactions between atoms. However, QM methods are computationally expensive for relatively large systems. On the other hand, classical or molecular mechanics (MM) methods cannot be used to simulate reactions where covalent bonds are broken/formed. Therefore, large systems may be partitioned into an electronically important region which requires a quantum chemical treatment and a remainder (where no chemical reactions take place) which can be described classically. Based on this idea, a new class of method has emerged which is

a combination of QM and MM calculations. These methods are known as mixed or hybrid quantum-mechanical and molecular mechanics methods (hybrid QM/MM). The Nobel prize in Chemistry 2013 was awarded jointly to M. Karplus, M. Levitt, and A. Warshel for the development of QM/MM methods for complex chemical systems [52, 53]. In QM/MM methods, the region of the system in which the chemical process takes place (for example, active-site of an enzyme) is treated quantum mechanically and rest of the system is treated classically. Several software packages are available for these types of hybrid calculations, such as QChem [54], TeraChem [55].

In this thesis, we have used QM/MM methods to describe the interactions between ions and graphene flakes in water, as implemented in TeraChem [55]. The graphene flakes and the ions were treated quantum mechanically and water was treated classically (calculations were performed by Mr. Dominic Esan).

2.7 Ab-initio Molecular Dynamics

Classical MD simulations using "fixed and predefined potentials", based on empirical data or on independent electronic structure calculations, are a well established tool to investigate physical properties of large systems. Despite an overwhelming success of classical MD simulations, they have some serious drawbacks. For example, they can not be used to model chemical reactions. On the other hand, *ab-initio* molecular dynamics (AIMD) explicitly describe all the electrons which are necessary to model chemical reactions or the processes which involve multiple electronic states. Thus, AIMD allows chemical bond breaking and forming events to occur and accounts for electronic polarization effects. In AIMD simulations, the potential energy sur-

face (PES) is constructed using electronic structure calculations. The classical forces on atoms are calculated from the gradient of the PES and are used to solve the equations of motion. Here, we have used HF and DFT (B3LYP) methods for electronic structure calculations. In this thesis, we have used BO AIMD to describe the interactions between ions and hydrogen passivated graphene flakes, as implemented in TeraChem [55].

CHAPTER 3

NANODROPLET ACTIVATED AND GUIDED FOLDING OF GRAPHENE NANOSTRUCTURES

3.1 Introduction

In this chapter, we demonstrate by classical MD simulations that water nanodroplets can activate and guide the folding of planar graphene nanostructures. We show that nanodroplets can induce rapid bending, folding, sliding, rolling and zipping of the planar nanostructures, which can lead to the assembly of nanoscale sandwiches, capsules, knots and rings. This research was conducted by myself and (currently Dr.) Boyang Wang. I performed most of the simulations and analysis. The following contents are reproduced with permission from Nano Lett., 9(11):3766-3771, 2009. Copyright (2009) American Chemical Society (see appendix).

The essence of "bottom-up" material preparation techniques is to guide the self-assembly of material units toward the final structures [56, 57]. Although they can be far less energy and material demanding than the popular "top-down" techniques, their use is mostly limited to biomineralization and other biologically guided processes [58]. In order to overcome the lack of guidance at the nanoscale, we might receive help from biological systems, as recently shown by Belcher on the preparation of battery electrodes by viruses [59]. Alternatively, we need to learn how to precisely control the competition of van der Waals (vdW), Coulombic, entropic and other forces [60], in order to tailor precisely ordered structures. Once mastered,

the guided assembly processes should allow reproducible preparation of complex structures, such as nanoparticles [61–64] and nanorod [65, 66] superlattices.

Recently, graphene monolayers have been prepared and intensively studied [19, 67–69]. Graphene nanoribbons have also been synthesized [70–72], and etched by using lithography [73, 74] and catalytic [75, 76] methods. *Graphene flakes* with strong interlayer vdW binding can self-assemble into larger structures [77–79]. Individual flakes with high elasticity [80–82] could also fold into a variety of 3D structures, such as carbon nanoscrolls [83, 84]. These nanoscrolls could be even prepared from single graphene sheets, when assisted by certain gases or alcohols [85, 86]. In order to reproducibly prepare such stable or metastable structures of different complexity, (1) the potential barriers associated with graphene deformation need to be overcome, (2) the folding processes should be guided and (3) the final structures need to be well coordinated and stabilized by vdW or other coupling mechanisms.

Carbon nanotubes (CNT) can serve as a railroad for small water droplets [87]. CNTs submerged in water can assemble into micro-rings around bubbles formed by ultrasonic waves [88]. Similar assembly effects might work in 2D graphene-based systems. For example, liquid droplets can induce wrinkles on thin polymer films by strong capillary forces [89]. Droplets can also guide folding of 3D microstructures from polymer (PDMS) sheets [90]. The question is if nanodroplets (ND) can activate and guide folding of graphene flakes into complex shapes, analogously like chaperones fold proteins [91].

3.2 Computational Methods

We model this system by molecular dynamics (MD) simulations with the NAMD package with CHARMM27 force field [29, 30, 92]. Here, the (non-bonding) vdW coupling between ith and jth atoms is described by the Lennard-Jones potential,

$$V_{i,j} = \epsilon_{i,j} \left[(R_{min,i,j}/r_{i,j})^{12} - 2\,(R_{min,i,j}/r_{i,j})^{6} \right],$$
$$\epsilon_{i,j} = \sqrt{\epsilon_i\,\epsilon_j}, \qquad R_{min,i,j} = \frac{1}{2}\,(R_{min,i} + R_{min,j})\,, \tag{3.1}$$

where the parameters for graphene carbon are set to be $\epsilon_C = -0.07$ kcal/mol, $R_{min,C} = 3.98$ Å, for water oxygen, $\epsilon_O = -0.12$ kcal/mol, $R_{min,O} = 3.4$ Å, and for water hydrogen, $\epsilon_H = -0.046$ kcal/mol, $R_{min,H} = 0.44$ Å.

We calculate the flexural rigidity D of our graphene sheets and compare it with theoretical results [93–95]. We simulate a graphene sheet, with the size of $a \times b = 3.7 \times 4.0$ nm^2, which is rolled into a cylinder with the radius of $R = a/2\,\pi$; we use the force field parameters from CHARMM27 ($k_{bond} = 322.55$ kcal/a^2, $k_{angle} = 53.35$ kcal/mol-rad^2 and $k_{dihedral} = 3.15$ kcal/mol). From the simulations, we calculate the energy associated with the cylindrical deformation of the graphene sheet, to obtain its strain energy density σ_{ela}. This allows us to calculate the flexural rigidity D, by using the formula $\sigma_{ela} = \frac{1}{2}\,D\,\kappa^2$, where $\kappa = 1/R$ is valid in the linear elastic regime [96]. The obtained value of $D = 0.194$ nn nm (27.9 kcal/mol) is in close agreement with *ab-initio* results, $D_1 = 0.238$ nn nm [94], and other model studies,

giving $D_2 = 0.11$ nn nm [95] and $D_3 = 0.225$ nn nm [96]. Therefore, our simulations should be reasonably close to potential experiments.

3.3 Results and Discussion

First, we study the interaction of a water nanodroplet, of $N_w = 1300$ waters, with a graphene sheet, of the size of 15×12 nm^2. It turns out that the nanodroplet, equilibrated at $T = 300$ K, induces a shallow dent in the graphene sheet, with the curvature radius of $R \approx 5$ nm. The hole formation is driven by vdW coupling, which tends to minimize the surface of the naked droplet but maximize the surface of the graphene-dressed droplet. As shown in Figure 2, two such droplets adsorbed on the opposite sides of the graphene sheet couple to minimize the dent formation energy. The two droplets stay together during a correlated diffusion motion on the graphene surface.

3.3.1 Folding of flakes

Intrigued by the action of NDs on graphene, we test if they can activate and guide folding of graphene flakes of various shapes. As shown in Figure 3a, we first design a graphene nanoribbon, where two rectangular 3×5 nm^2 flakes are connected by a narrow stripe of 2.5×0.73 nm^2. In the simulations, we fix a few stripes of benzene rings on the right flake, which could be realized if the graphene is partly fixed at some substrate, and position a water nanodroplet ($N_w = 1300$) above the center of the two flakes ($T = 300$ K). (b) After $t \approx 250$ ps, both flakes bind with the droplet and bend the connecting bridge to form a metastable sandwich structure. (c) When the temperature is raised to $T = 400$ K, the droplet becomes more mobile and fluctuating. Within $t \approx 50$ ps, the two flakes start to bind each other, and the water droplet is squeezed away. (d)

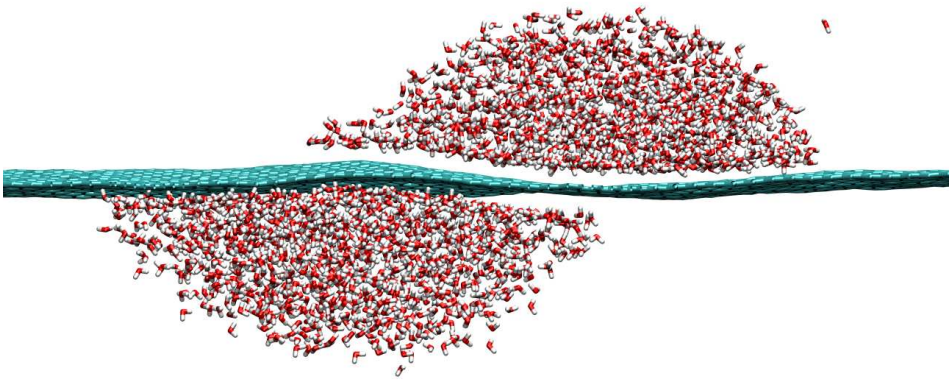

Figure 2. Side view on two water nanodroplets, each with $N_w = 1300$ molecules, adsorbed on the opposite sides of a graphene sheet. The nanodroplets create two shallow holes in the graphene. Eventually, the nanodroplets become adjacent but stay highly mobile. Their dynamical coupling is realized by the minimization of the graphene bending energy associated with the two holes.

After another $t \approx 60$ ps, the flakes join each other into a double layer, and the droplet stays on the top of one flake. When a smaller water droplet with $N_w = 800$ is placed on the nanoribbon, it induces its folding in a similar way and becomes squeezed out even faster in (c-d).

Similarly, we study the folding of a star-shaped graphene nanoribbon with four blades connected to a central flake, as shown in Figure 3e,f. At $T = 300$ K, a water droplet ($N_w = 1300$) is initially positioned at the height of $h \approx 0.5$ nm above the central flake. (g) The droplet binds by vdW coupling with the central flake, and induces bending of the four blades. (h) After $t \approx 1$ ns, the four blades fold into a closed structure, with waters filling its interior. This effect resembles the action of a "meat-eating flower" [97], where the graphene capsule can store

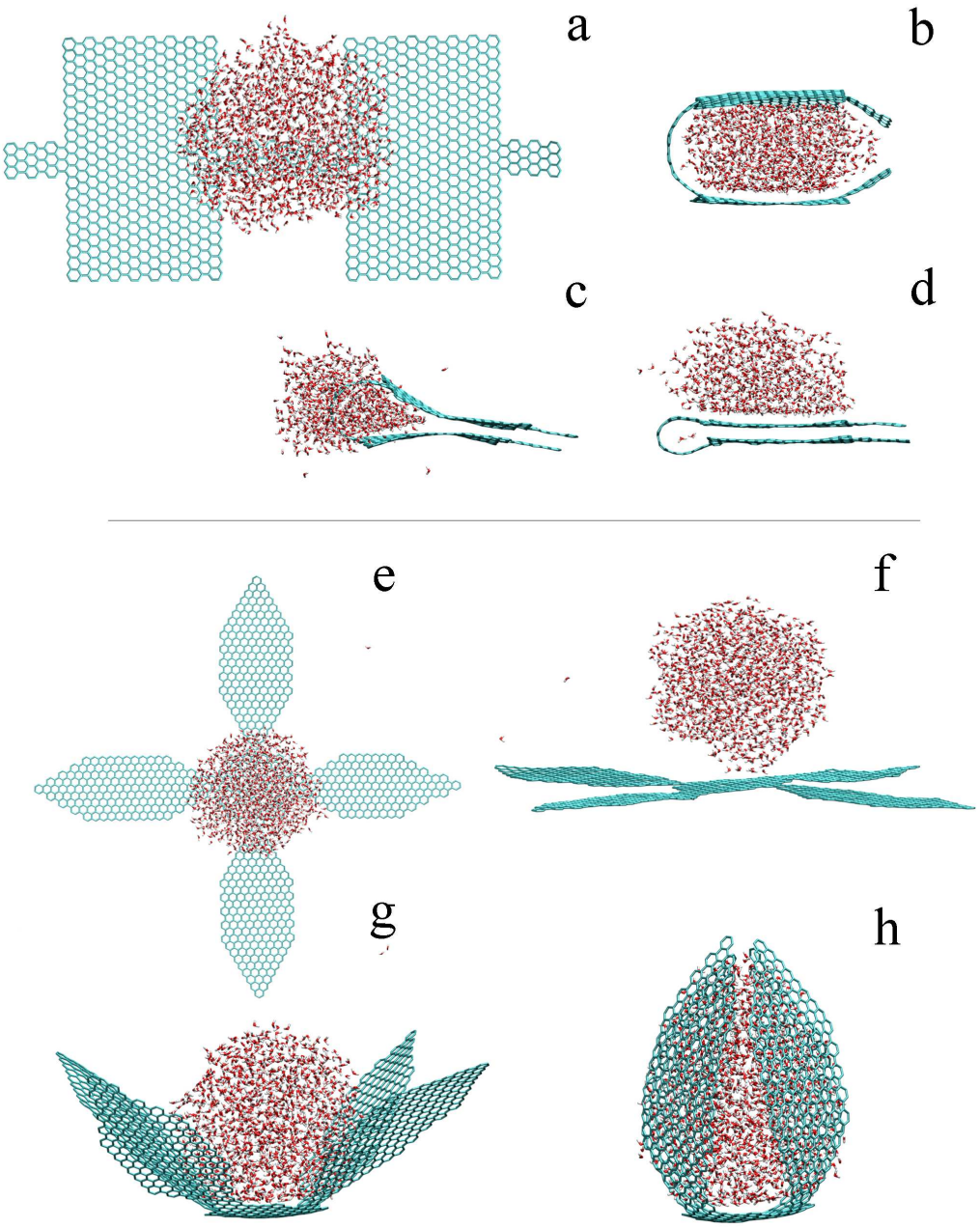

Figure 3. (a-d) Water nanodroplet activated and guided folding of two graphene flakes connected by a narrow bridge. The nanodroplet is squeezed away when the system is heated to $T = 400$ K. (e-h) Nanodroplet assisted folding of a star-shaped graphene flake, resembling the action of a "meat-eating flower".

and protect the liquid content in various environments. Notice that slight asymmetry of the flake does not change the character of the assembly process. In real systems, other molecules might also be adsorbed on the graphene flakes. Although these molecules are not considered here, they might coalesce with the water droplets and modify their properties in the assembly process. Experimentally, the droplets could be deposited by Dip-Pen nanolithography [98] or AFM [99]. This deposition can also cause side effects not considered here, such as passage additional momentum to the folding sheet.

Folding of the two flakes into the sandwich, shown in Figure 3a,b, is driven by the decrease of the water-graphene binding energy, $E_{g-w} = -\sigma_{g-w} A_{g-w}$. Here, we estimate the density of the binding energy from our MD simulations [92] to be $\sigma_{g-w} \approx 20.8$ kcal/(mol nm^2). The water-graphene binding area of the narrow stripe (initial area) and the two flakes (final area) are $A_{g-w}^{ini} = 2.5 \times 0.7 = 1.75$ nm^2 and $A_{g-w}^{end} = 3 \times 5 \times (2) = 30$ nm^2, respectively. The elastic bending energy of the connecting stripe is $E_{ela} = \sigma_{ela} A_{ela}$, where $A_{ela} \approx A_{g-w}^{ini}$ is the bending area, and $\sigma_{ela} = \frac{1}{2} D \kappa^2$ is calculated for $D = 27.9$ kcal/mol and $\kappa = 1/R_g$, where R_g is the graphene ribbon radius. In this case, $R_g \approx 1$ nm, so $\sigma_{g-w} > \sigma_{ela} \approx 14$ kcal/(mol nm^2). This, together with $A_{g-w} \approx A_{ela}$, valid at the beginning of the folding process, means that $E_{g-w} + E_{ela} < 0$. During the folding process, the sandwich configuration becomes further stabilized, since E_{g-w} decreases by an order of magnitude, due to $A_{g-w} = A_{g-w}^{end}$. The final squeezing of the nanodroplet out of the sandwich, shown in Figure 3c,d, means that graphene-graphene vdW binding is preferable to graphene-water vdW binding.

3.3.2 Folding of ribbons

We now test if NDs can induce folding of graphene nanoribbons. As shown in Figure 4a, we use a 30×2 nm^2 graphene nanoribbon, with one end fixed. At $T = 300$ K, a ND with $N_w = 1300$ waters is positioned above the free end of the ribbon. (b) The free end starts to fold fast around the droplet. (c) After $t = 0.6$ ns, the free end folds into a knot structure, touches the ribbon surface and starts to slide fast on it, due to strong vdW binding. (d) While the knot is sliding on the ribbon, the droplet is deformed into a droplet-like shape that slips and rolls inside the knot [87]. After sliding over $l = 20$ nm, the water filled knot gains the velocity of $v_w \approx 100$ m/s. This velocity is controlled by the rate of releasing potential energy, due to binding but reduced by bending, into the kinetic degrees of freedom, damped by friction. (d) The sliding ribbon reaches the fixed end and overstretches into the space, due to its large momentum. (e) It oscillates back and forth 2-3 times before the translational kinetic energy is dissipated.

The existence of CNTs raises the question if we could also "roll" graphene ribbons. This might happen when the droplet is larger and thus when it controls more of the ribbon dynamics. In Figure 5a, we simulate the folding of a 90×2 nm^2 graphene ribbon (one end is fixed) at $T = 300$ K, when a droplet of $N_w = 10,000$ is initially positioned above the tip of the ribbon. (b-c) As before, within $t = 2$ ps, the ribbon tip folds around the spherical droplet into a closed circular cylinder. (d) This time, the approaching free end touches the surface at a larger angle and forms a cylinder around the droplet that starts to roll fast on the ribbon surface, like a contracting tongue of a chameleon. After rolling over $l = 60$ nm, the translational and rolling

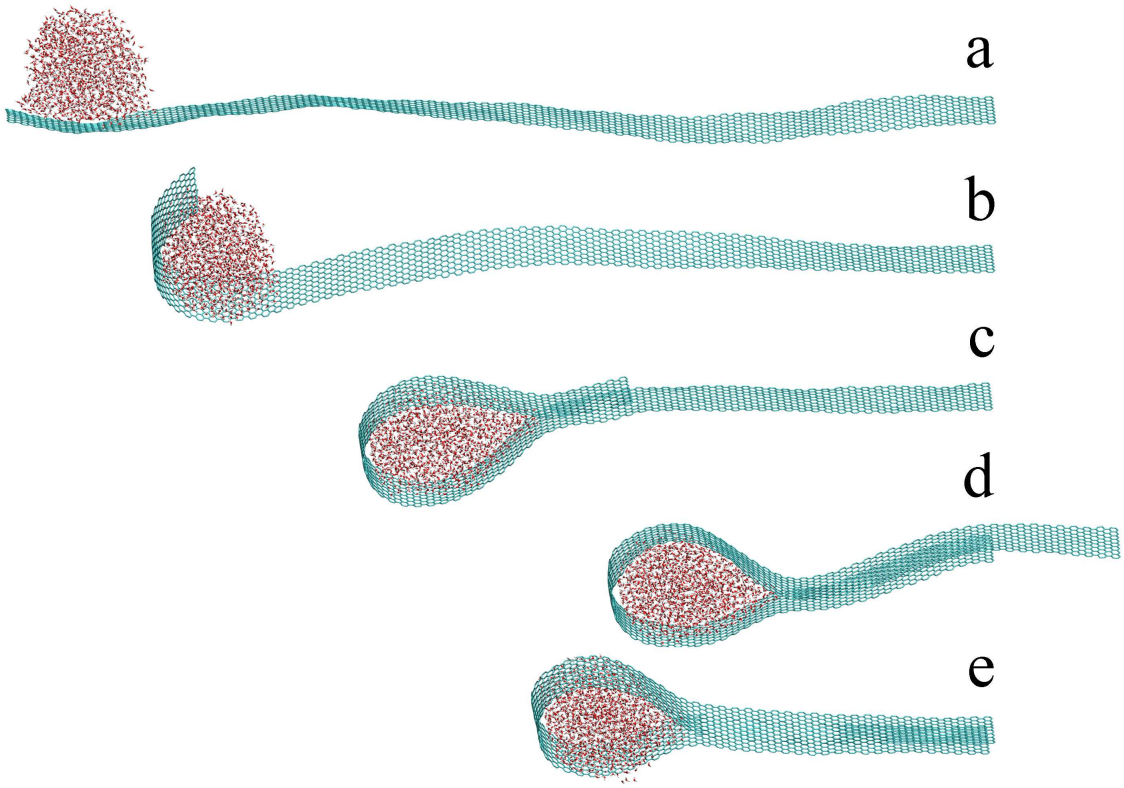

Figure 4. Folding and sliding of a graphene ribbon with the size of 30×2 nm^2, which is activated and guided by a nanodroplet with $N_w = 1300$ waters and the radius of $R_d \approx 2.1$ nm. (a-c) The free ribbon end folds around the droplet into a knot structure that slides on the ribbon surface (d-e).

velocities are $v_t \approx 50$ m/s and $\omega_r \approx 12$ rad/ns, respectively. (e) The cylinder rolls until the fixed end of the ribbon, where the rolling kinetic energy is eventually dissipated. The folded ribbon forms a multilayered ring structure, similar to multiwall nanotube, which is filled by water.

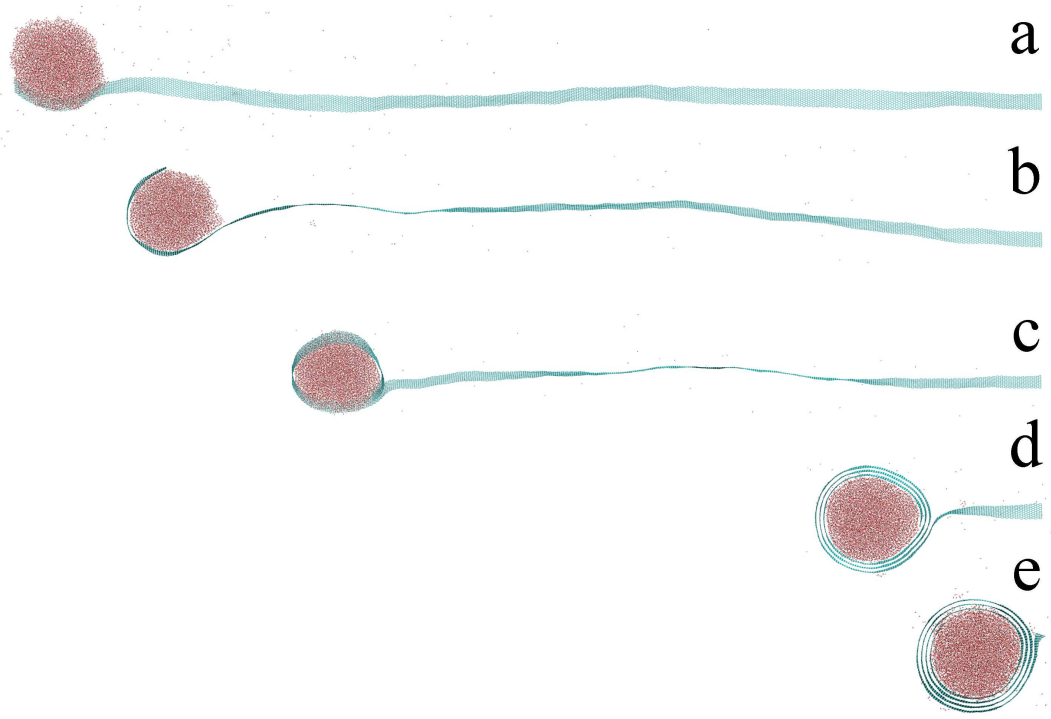

Figure 5. Folding and rolling of a graphene ribbon with the size of 90×2 nm^2, which is activated and guided by a nanodroplet with $N_w = 1,0000$ waters and the radius of $R_d \approx 4.2$ nm. (a-b) The ribbon tip folds around the water droplet into a wrapped cylinder, and (c-e) the wrapped cylinder is induced to roll on the ribbon surface (c-e).

Let us analyze the conditions under which a graphene ribbon folds. Analogously to the folding of flakes, shown in Figure 3, the folding of ribbon is driven by the competition between the graphene-water binding energy, $E_{g-w} = -\sigma_{g-w}\, A_{g-w}$, and the graphene bending energy, $E_{ela} = \sigma_{ela}\, A_{ela}$. From the energy condition, $E_{g-w} + E_{ela} < 0$, we obtain

$$\frac{A_{g-w}}{A_{ela}} > \frac{\sigma_{ela}}{\sigma_{g-w}}\,. \tag{3.2}$$

In Figure 4, the water droplet has the radius $R_d \approx 2.1$ nm. Assuming that $R_g \approx R_d$, we obtain from the above formula for σ_{ela} that $\sigma_{ela} = 3.2$ kcal/ (mol nm^2) and $\sigma_{ela}/\sigma_{g-w} \approx 0.15$. Since, $A_{g-w}/A_{ela} \approx 1$, we see that this case easily fulfills the condition in Equation 3.2. The graphene ribbon slides on itself, and this situation can be called the "sliding phase".

The ratio A_{g-w}/A_{ela} and indirectly also σ_{ela} depend on the ratio of the ribbon width w to the droplet radius R_d, which thus controls the character of the folding process. When $w < 2\,R_d$, the droplet can bind, in principle, on the whole width of the ribbon, so $A_{g-w} \approx A_{ela}$. For even larger droplets, we eventually get $w < 0.5\,R_d$, where our simulations show that the ribbon binds fully to the droplet surface. In this limit, we observe that after folding once around the droplet circumference the ribbon approaches itself practically at the wetting angle, and gains the dynamics characteristic for the "rolling phase", shown in Figure 5.

When $w > 2\,R_d$, it becomes very difficult for the small droplet to induce folding of the wide ribbon. Then, the droplet binds to the ribbon at an approximately circular area, with a radius $\approx R_d$, because the water contact angle on graphene is about 90° and the droplet has

almost the shape of a half-sphere [100]. If we assume that $R_g \approx R_d$, we have $A_{g-w} \approx \pi R_d^2$ and $A_{ela} \approx 2R_d\, w$. From Equation 3.2 and $\sigma_{ela} = \frac{1}{2} D \kappa^2 = \frac{1}{2} D \frac{1}{R_d^2}$, we then obtain the condition for the ribbon folding

$$R_d^3 > \frac{D\, w}{\pi\, \sigma_{g-w}}\,. \tag{3.3}$$

On the other hand, this means that the ribbon does not fold when $w \geq C\, R_d^3$ ($C = \pi\, \sigma_{g-w}/D \approx 4$ nm^{-2}), and this situation can be called the "nonfolding phase".

In Figure 6, we summarize the results of our simulations in a phase diagram. We display four "phases" characterizing the ribbon dynamics, separated by phase boundary lines. They are called nonfolding, sliding, rolling and zipping, where the first three were described and briefly analyzed above. The nonfolding phase, where the ribbon end does not fold around the droplet, is characterized by the cubic boundary derived above and shown in Figure 6 (left). In the simulations, we obtain the value $C \approx 2.8$ nm^{-2}, in close agreement with the above prediction. The nonfolding phase is adjacent with the sliding phase, which is separated from the rolling phase by the boundary line $w \approx \frac{1}{2} R_d$.

When the graphene ribbon becomes several times wider than the droplet diameter, it may fold around it in the orthogonal direction. Then, the folding dynamics of the graphene ribbon has a character of zipping. This situation corresponds to the "zipping phase", shown in the right top corner of the phase diagram in Figure 6 and explained in detail in Figure 7. (a) We place a droplet of $N_w = 17,000$ at the free end of the ribbon of the size of 60×16 nm^2. (b) The ribbon folds from the two sides of the droplet within $t \approx 250$ ps. (c) At $t \approx 450$ ps, the ribbon starts to "zip", where its two sides touch each other. (d) The zipping process continues, and

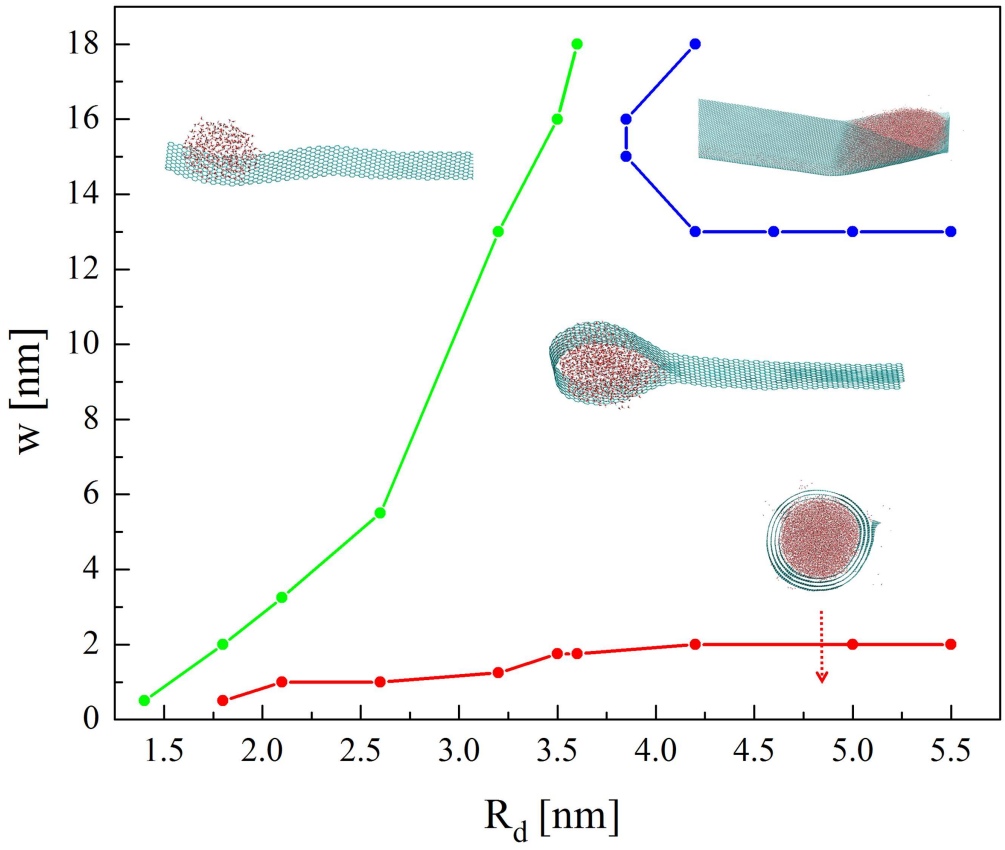

Figure 6. The phase diagram of a nanodroplet and graphene nanoribbon with different folding dynamics. We display the nonfolding, sliding, rolling and zipping phases.

the droplet is transported along the ribbon. After zipping over $l \approx 40$ nm, the droplet gains a translational velocity of $v_t \approx 63$ m/s. In the zipped region, a chain of water molecules resides inside the turning line of the zipped ribbon. This region can be used like an artificial channel, similarly like CNTs.

We have also observed that the folding dynamics can be in some cases influenced by the initial position of the droplet on the graphene ribbon. This is particularly true if the ribbon is significantly wider than the droplet. Then, if the droplet is, for example, placed at the ribbon corner, the system can get to either the zipping or sliding phases. On the other hand, only the zipping phase is observed when the droplet is placed more towards the center of the ribbon edge. These examples show the rich possibilities for droplet controlled folding of graphene systems.

Finally, we briefly characterize coupling of the graphene-ribbon ring, shown in Figure 5, to larger droplets, which might have potential applications. Here, we consider cases with a hydrophobic ring, solely made of a graphene nanoribbon of 30×2 nm^2, and a hydrophilic ring, where we replace a flake of 1×2 nm^2 at the tip of the 30×2 nm^2 graphene ribbon by a boron-nitride (BN) ribbon [92]. As show in Figure 8, (a) the hydrophobic ring is stable in a "capping" configuration, where it sits on the droplet with $N_w = 10,000$ at $T = 300$ K. (b) The hydrophilic ring, with a BN region folded inside, can have a metastable "locking" configuration, in addition to the stable capping configuration on the droplet surface with $N_w = 18,000$ (not shown but similar to a). In the locking configuration, the hydrophilic ring is pierced inside the droplet, and partly exposes its external surface outside the droplet.

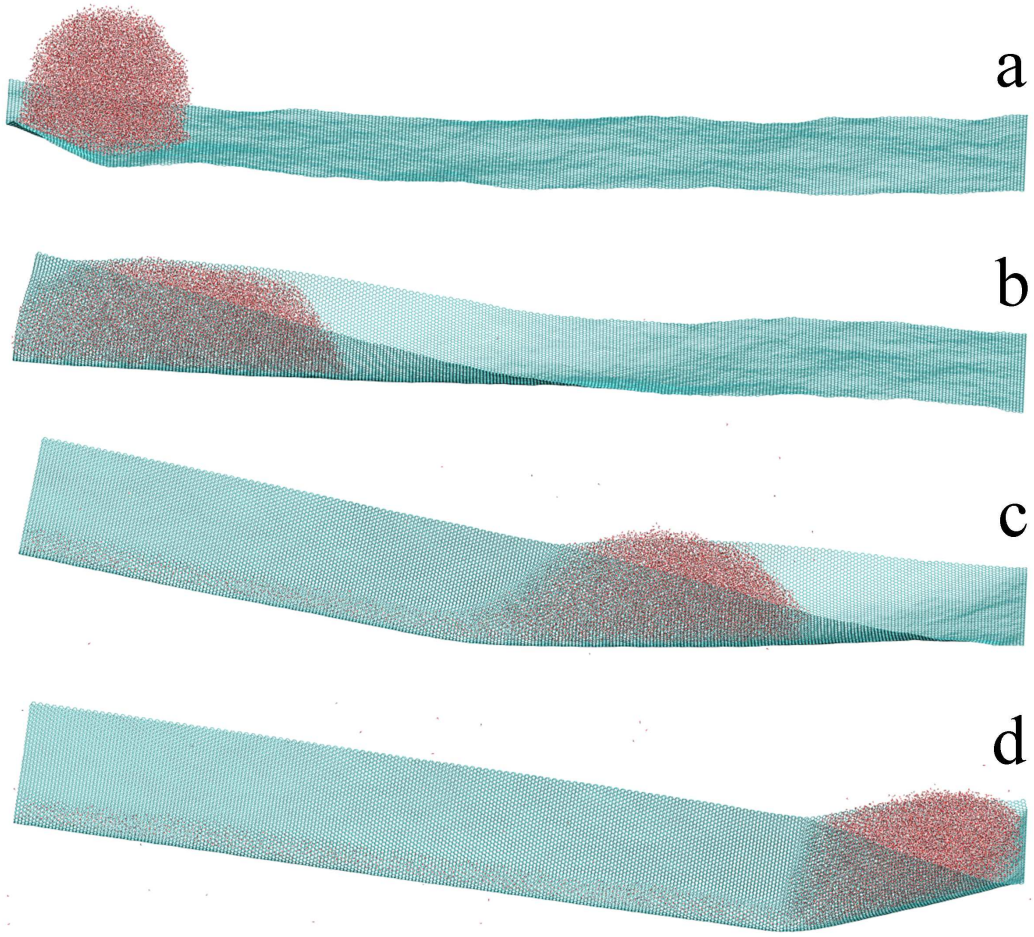

Figure 7. Folding and zipping of a graphene ribbon with the size of 60×16 nm^2, which is activated and guided by a nanodroplet with $N_w = 17,000$ waters and the radius of $R_d \approx 5$ nm. (a-b) The ribbon end folds around the droplet. (c-d) The zipping propagates along the ribbon until the fixed end, while water channel is formed in the graphene sleeve.

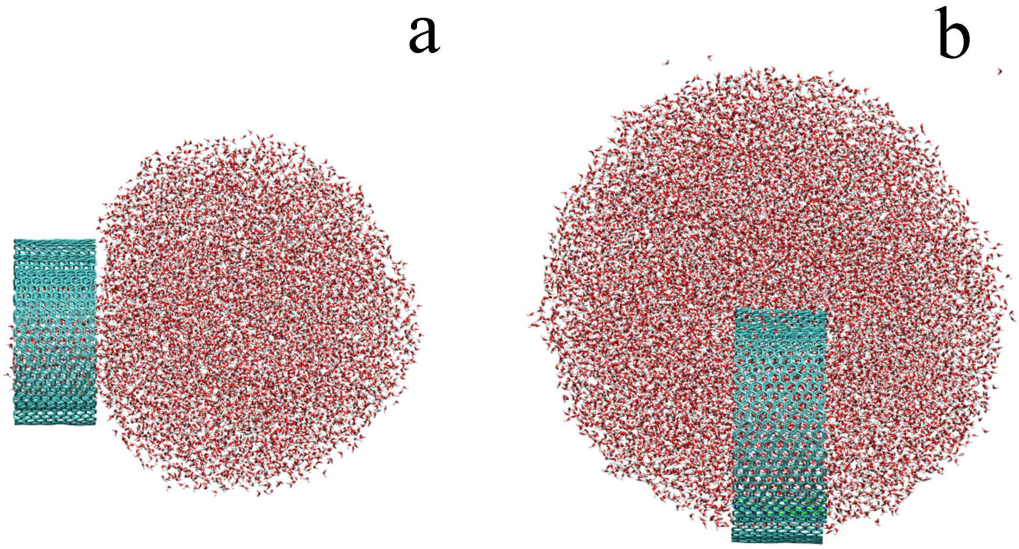

Figure 8. Binding modes of graphene rings based on a ribbon with the size of 30×2 nm^2, inside water droplets. (a) The stable "capping" configuration of a hydrophobic ring with $N_w = 10,000$ waters. (b) The metastable "locking" configuration of a hydrophilic ring with $N_w = 18,000$ waters.

3.4 Conclusion

In this chapter, we have demonstrated that water nanodroplets can activate and guide folding of graphene nanostructures. The folding can be realized by different types of motions, such as bending, sliding, rolling or zipping that lead to stable or metastable structures, such as sandwiches, capsules, knots and rings. These structures can be the building blocks of functional nanodevices, with unique mechanical, electrical or optical properties [101]. We also studied the self-assembly of other graphene systems, as we discuss in the next chapter.

CHAPTER 4

SELF-ASSEMBLY OF GRAPHENE NANOSTRUCTURES ON NANOTUBES

4.1 Introduction

In this chapter, we demonstrate by classical MD simulations that carbon nanotubes can activate and guide on their surfaces and in their interiors the self-assembly of planar graphene nanostructures of various sizes and shapes. We show that nanotubes can induce bending, folding, sliding, and rolling of the nanostructures in vacuum and in the presence of solvent, leading to stable graphene rings, helices, and knots. We investigate the self-assembly conditions and analyze the stability of the formed nanosystems, with numerous possible applications. This research was conducted by myself and Mr. Yuanbo Song. While both of us participated in all the aspects of research (preparing the systems, carrying out the simulations, analyzing data, writing the manuscript), I performed most of the simulations and analyses. The following contents are reproduced with permission from ACS Nano, 5(3):1798-1804, 2011. Copyright (2011) American Chemical Society (see appendix).

Recently, graphene monolayers have been prepared and intensively studied [19, 67–69]. Graphene nanoribbons (*GNRs*) have also been synthesized [70–72, 102], and prepared from graphene monolayers and carbon nanotubes (*CNT*) by lithographic [73, 74] and catalytic methods [75, 76]. Graphene flakes with strong interlayer van der Waals (*vdW*) coupling and chemical

functionalization at their edges can self-assemble into larger structures [77–79]. Highly elastic graphene [80–82] could fold under suitable conditions into nanoscrolls [83–86] and a variety of other 3D nanostructures [103].

Novel composite functional materials could be prepared if planar graphene nanostructures of various shapes and sizes are self-assembled on the surfaces of nanoscale materials. Highly rigid *CNTs*, with selective and strong vdW coupling to planar graphene surfaces [104, 105] and to molecules adsorbed on them [106], might form suitable substrates for this graphene self-assembly. Here, we test by atomistic molecular dynamics (*MD*) simulations if planar graphene nanostructures could self-assemble on *CNT* surfaces and in their interiors.

4.2 Computational Methods

We model the self-assembly processes by atomistic molecular dynamics (*MD*) simulations with the *NAMD* package and the *CHARMM27* force field [29, 30]. The (non-bonding) *vdW* coupling between the ith and jth carbon atoms in the *CNTs* and graphene is described by the Lennard-Jones potential,

$$V_{i,j} = \epsilon_C \left[\left(\frac{r_{min,C}}{r_{i,j}} \right)^{12} - 2 \left(\frac{r_{min,C}}{r_{i,j}} \right)^{6} \right], \tag{4.1}$$

where $\epsilon_C = -0.07$ kcal/mol and $r_{min,C} = 3.98$ Å. The *vdW* coupling of other atoms is described in the *CHARMM27* force field [29]. The systems are modeled in *NVT* ensembles at $T = 300$ K, and the time step is 1 fs. The Langevin damping [42] is used to thermalize the systems and mimic the missing electron coupling, while the phonon coupling is largely present in these

simulations. We use a small damping coefficient of $\gamma = 0.01$ ps^{-1} that should be sufficient to this purpose [103]. The value of γ should be kept small, since the Langevin dynamics does not preserve momentum during the self-assembly. In most cases, its value is not expected to significantly influence the observed folding dynamics, except of the folding speed. Electronic polarization of the studied systems is neglected. In all the studied systems, *GNRs* have armchair structures along their long edges and *CNTs* have zigzag structures.

4.3 Results and Discussion

4.3.1 GNR folding outside and inside CNTs

In Figure 9, we show how a *GNR* of the length of $l_G = 40$ nm and the width of $w = 3$ nm rolls on a (60,0) *CNT* of the length of $l_C = 20$ nm, with its two ends fixed. Initially, the *GNR* tip is positioned perpendicularly ($\varphi = 0$) to the *CNT* axis close to its surface. As shown in Figure 9a, the tip immediately starts to fold on the *CNT*, due to large *vdW* coupling. After $t \approx 0.5$ ns, the *GNR* forms a single layer around the *CNT* (Figure 9b). Within another $t \approx 1$ ns, it forms a multilayered ring structure (Figure 9c,d).

We investigate further how the initial angle φ of the *GNR* with respect to the *CNT* axis affects the self-assembly processes. In Figure 10a-c, the tip of the *GNR* (40×2 nm^2) is initially positioned on the same *CNT* at the angle of $\varphi = 60°$. The tip again folds fast around the *CNT* (Figure 10a). After $t = 0.5 - 1$ ns, it starts to fold around the *CNT* in a spiral manner (Figure 10b,c). The spiral becomes denser, where the neighboring edges close to each other, and the *GNR* eventually forms a stable helical structure. The self-assembly speed is determined

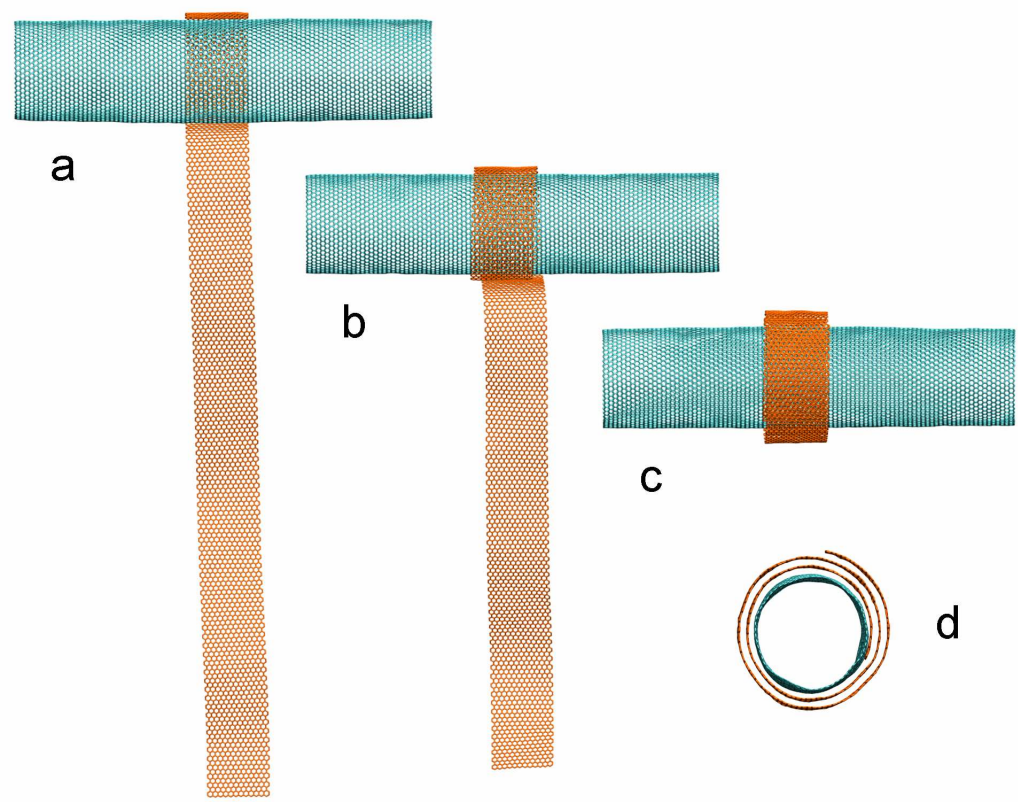

Figure 9. Rolling of a *GNR* (40×3 nm^2) on a (60,0) *CNT* when placed close to the *CNT* perpendicular to its axis.

by the strength of vdW forces acting on the *GNR*, and the rate of its momentum dissipation, due to friction with the *CNT*.

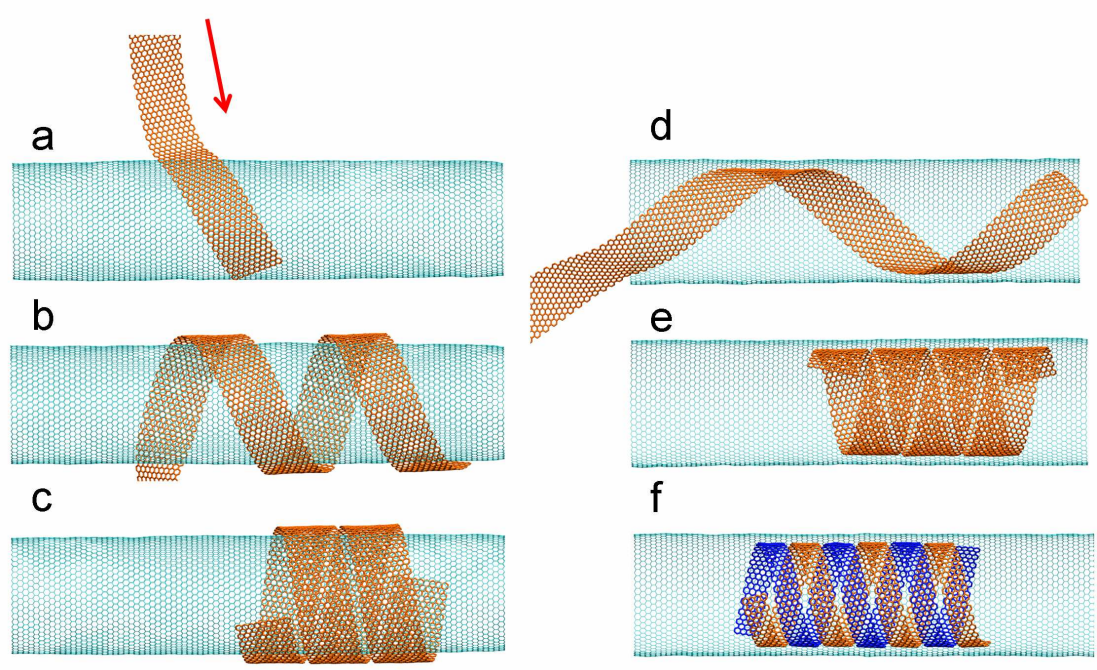

Figure 10. (a-c) Helical rolling of a *GNR* (40×2 nm^2) when placed at the angle of $\varphi = 60°$ with respect to the axis of the $l = 20$ nm (60,0) *CNT*. (d-e) The same when this *GNR* is placed inside this *CNT* (front part of the *CNT* is removed for better visualization). (f) The final structure of two *GNRs* (40×1 nm^2) when placed inside this *CNT* .

We test if *GNRs* can also fold inside *CNTs*. As shown in Figure 10d,e, we put a *GNR* (40×2 nm^2) inside the above *CNT*. Initially, the ribbon is placed at the *CNT* entrance and its orientation is parallel with the *CNT* axis. First, the *GNR* sticks to the interior surface of *CNT*

and starts to enter the *CNT* in a straight motion (Figure 10d). Within $t \approx 0.5$ ns, it reaches the other *CNT* end, overstretches it, and comes back. The *GNR* motion eventually loses its straight symmetry and gains a helical form, with a randomly oriented rotation direction. Within several ns, the helical pitch becomes denser, until it is so dense that the *GNR* edges touch each other (Figure 10e). The helical structure equilibrates and stays in a folded form inside the *CNT*. We always observe formation of the same helical structure, independently on the initial position of the *GNR* with respect to the *CNT* center. However, we can control the helicity of the folded *GNR* by the initial angle φ.

We also study folding of two *GNRs* (40×1 nm^2) inside this *CNT*. Initially, the *GNRs* are placed on the top of each other and placed at one *CNT* entrance. Upon release, both *GNRs* start to move in parallel inside the *CNT*. After $t \approx 1$ ns, they start to fold in a helical manner in the same direction. Within $t \approx 3$ ns, the two *GNRs* form a double helical structure, as shown in Figure 10f. While the helical orientation of the two *GNRs* can be controlled by the initial angle φ, the two equilibrated *GNRs* always end up having the same orientations. When we simultaneously place more *GNRs* on the surface or in the interior of *CNT*, the *GNRs* tend to fold side by side rather than on the top of each other. This is caused by smaller *GNR* deformation energies and larger *GNR-CNT vdW* attractions (geometrical overlap). However, *GNRs* can fold on each other if we release the second *GNR* later.

In Figure 11, we summarize in phase diagrams the structures obtained in *MD* simulations of *GNR* folding outside *long CNTs* ($l_C \gg l_G$). All these (stable or metastable) structures are obtained by initially placing the *GNRs* in contact with the *CNTs* and then releasing them. The

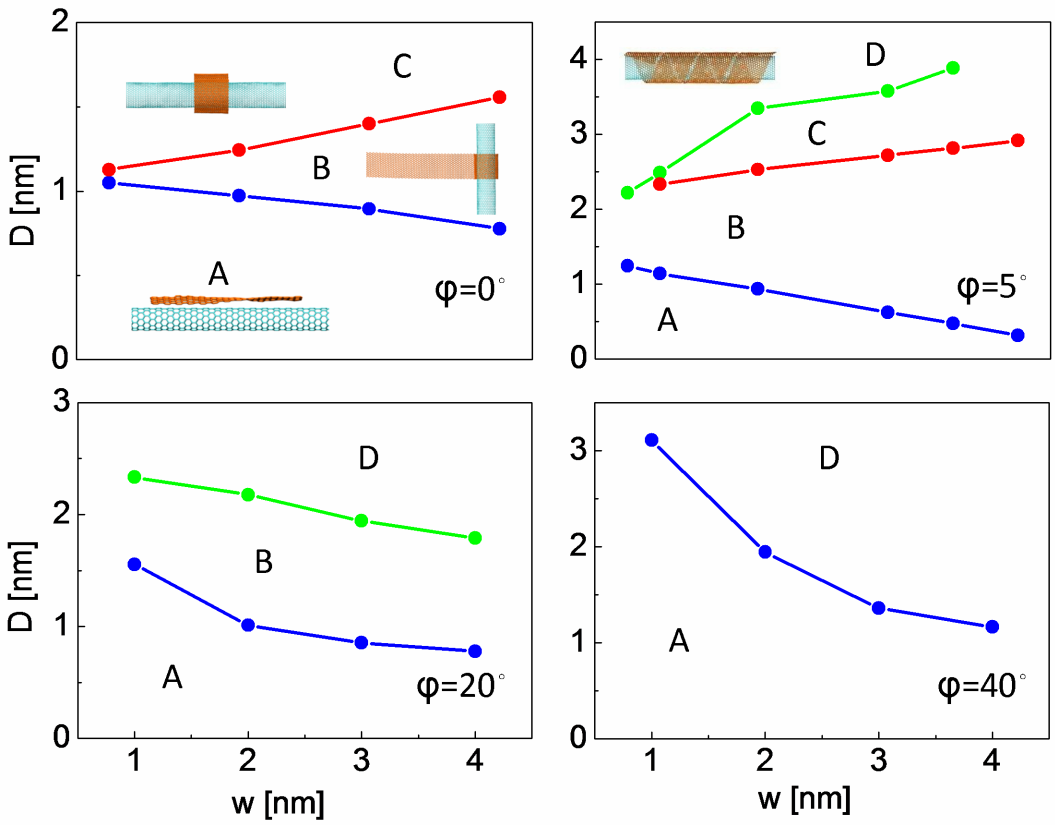

Figure 11. Phase diagrams of *GNRs* of the width w self-assembled on long *CNTs* of the diameter D_C, shown for different initial angles φ with respect to the *CNT* axis. The *GNRs* self-assemble into nanostructures called the (A) straight, (B) nonfolding, (C) rolling, and (D) helical phases.

structures are presented in dependence on the *CNT* diameter, D_C, the *GNR* width, w, and the initial angle, φ, of the *GNR* with respect to the *CNT* axis. We display four types of structures, called the (A) straight, (B) nonfolding, (C) rolling, and (D) helical phases. For small angles, $\varphi < 5°$, we obtain the A, B, and C phases, as shown in Figure 11 (top left). When we increase the angle to $\varphi \approx 5 - 15°$, the D phase appears for large *CNTs*, as shown in Figure 11 (top right). At larger angles, $\varphi > 20 - 30°$, the C phase disappears, as seen in Figure 11 (bottom left). When the angle is further increased, $\varphi > 30°$, the B phase disappears as well, as seen in Figure 11 (bottom right). Analogously, we can obtain phase diagrams for the self-assembly of *GNRs* inside *CNTs* and in other cases of interests.

4.3.2 Analytical model

We use a simple analytical model to understand the conditions under which *GNRs* self-assemble into different structures outside and inside *CNTs*. We describe the total *CNT–GNR* coupling energy in the form

$$\begin{aligned} E_{total} &= E_{ela} + E_{C-G} + E_{G-G}\,, \\ E_{C-G} &= \sum_{i-CNT, j-GNR} V_{i,j} = \langle E_{C-G} \rangle + E_{sym}\,, \\ E_{G-G} &= \sum_{i,j-GNR} V_{i,j}\,. \end{aligned} \tag{4.2}$$

Here, E_{ela}, E_{C-G}, and E_{G-G} are the bending energy of *GNRs*, the *vdW* binding energy between *CNTs* and *GNRs*, and the *vdW* energy for coupling of neighboring layers or edges of

GNRs, respectively. The i, j-indices in the Lennard-Jones potential, $V_{i,j}$, of the form shown in Equation 4.1, run over atoms in the two subsystems.

The bending energy is given by $E_{ela} = \sigma_{ela}\, A_{ela}$, where σ_{ela} is the strain energy density and A_{ela} is the total bending area [96, 107]. In the linear elastic regime, $\sigma_{ela} = D\,\kappa^2/2$, where $\kappa = (\kappa_1 + \kappa_2)/2$ is the local mean curvature and D is the flexural rigidity. When a *GNR* folds on a *CNT*, one of the two curvatures is $\kappa_{1(2)} \approx 0$. Then, the curvature is given by $\kappa = R_G^{-1}$, where R_G is the radius of the folded *GNR*.

As shown in Equation 4.2, the coupling energy, E_{C-G}, can be split into the "mean-field" term, $\langle E_{C-G} \rangle$, and the "symmetry-related" term, E_{sym}. The first term represents the *vdW* coupling between *CNT* and *GNR* lattices that is averaged over the angle describing mutual orientation of the two sub-systems (smearing of their hexagonal lattices). The symmetry-related term accounts for the difference between the actual and smeared coupling (interferences) of the lattices in the *CNT* and *GNR* structures [104, 105]. Due to the last term, the *GNR* might have local potential energy minima for certain orientations with respect to the *CNT* (symmetry locking).

The full *CNT–GNR* coupling energy can be expressed as $E_{C-G} = -\sigma_{C-G}\, A_{C-G}$, where σ_{C-G} is the related (positive) energy density and A_{C-G} the related coupling area. Analogously, we can write the averaged and symmetry terms as $\langle E_{C-G} \rangle = -\langle \sigma_{C-G} \rangle A_{C-G}$ and $E_{sym} = -\sigma_{sym}\, A_{C-G}$, respectively. We estimate the σ_{sym} coefficient by placing a graphene flake with a hexagonal shape on a large graphene sheet [108]. Their binding energies E_{C-G} and E_{sym} have a C_6 symmetry with respect to rotation of the flake around the axis going through its

center and orthogonal to the graphene. The *GNR–GNR vdW* coupling energy (in the case of sidewise coupling) is $E_{G-G} = -\sigma_{G-G}\, L_{G-G}$, where σ_{G-G} and L_{G-G} are the (positive) sidewise *vdW* binding energy density and the *GNR* edge length, respectively. From our *MD* simulations and $D \approx 27.9$ kcal/mol [103], we estimate that $\langle \sigma_{C-G} \rangle \approx 56$ kcal/mol/nm^2, $\sigma_{sym} \approx 0.25$ kcal/mol/nm^2, and $\sigma_{G-G} \approx 2.9$ kcal/mol/nm [108].

4.3.3 Testing of the analytical model

We apply Equation 4.2 to several phases observed above. The necessary condition for the realization of the *CNT*-assisted self-assembly of *GNRs* is that the total energy in the self-assembled state is smaller than at the beginning, *i.e.*, $E_{total} < 0$ or $E_{C-G} + E_{G-G} < -E_{ela}$. More precisely, the energy should drop in every infinitesimal distortion of the system along the self-assembly trajectory. Therefore, local barriers may prevent the self-assembly in some cases even if $E_{total} < 0$.

First, we find the boundary of the B and C phases shown in Figure 11 (top left), *i.e.*, we estimate what is the minimum radius of *CNT*, $R_C = D_C/2$, on which a *GNR* can fold for $\varphi = 0$. The folding is driven by the competition between the E_{C-G} and E_{ela} energies. If we neglect the symmetry locking term, E_{sym}, we get $E_{C-G} \approx \langle E_{C-G} \rangle$ and from the folding condition, $E_{tot} = E_{C-G} + E_{ela} < 0$, we obtain that

$$\frac{A_{C-G}}{A_{ela}} > \frac{\sigma_{ela}}{\langle \sigma_{C-G} \rangle}\,. \tag{4.3}$$

Here, the area where the *GNR* couples to the *CNT* is also the bending area of the *GNR*, $A_{C-G} \approx A_{ela}$. If we assume that $R_C \approx R_G$, we obtain from Equation 4.3 and $\sigma_{ela} = D/2\,R_C^2$ the condition for the folding of *GNR*

$$R_C > \sqrt{\frac{D}{2\,\langle \sigma_{C-G} \rangle}}\,. \tag{4.4}$$

For the above values of D and $\langle \sigma_{C-G} \rangle$, Equation 4.4 gives that $R_C > 0.5$ nm, in a reasonable agreement with our simulations, giving the minimum value of $R_C \approx 0.7$ nm.

Next, we analyze the A (straight) and D (helical) *GNR* phases formed inside *CNTs*. Stabilization of these phases is similar to the cases with external *GNR* self-assembly, shown in Figure 11. To reproducibly obtain the A phase in the simulations, we need to remove the large initial potential energy of the system, otherwise the *GNR* acquires large oscillations which often lead to the helical D phase. We can do so by either placing the *GNR* (in a straight way) fully inside (outside) the *CNT* or by using a large Langevin damping constant (> 0.1 ps^{-1}).

We evaluate the binding energy in the A phase from Equation 4.2, where we consider a *GNR* (40×3 nm^2) placed in a straight way inside a (much longer) (60,0) *CNT*. When the *GNR* forms a monolayer on the *CNT* interior, its curvature is roughly the same in all the phases. Using the values of $R_G \approx 2$ nm and $A_{ela} = 120$ nm^2, the *GNR* bending energy is $E_{ela} = \sigma_{ela}\,A_{ela} = (D/2\,R_G^2)\,A_{ela} = 420$ kcal/mol. In the A phase, the *GNR* and *CNT* lattices are oriented in the same way, which gives the symmetry locking energy of $E_{sym} \approx -0.25 \times 120 \approx$

-30 kcal/mol. Then, considering the fact that $E_{G-G} = 0$, we obtain the total coupling energy of $E_{total} \approx E_{ela} + \langle E_{C-G} \rangle + E_{sym} \approx 420 - 56 \times 120 - 30 \approx -6330$ kcal/mol.

The coupling energy of the (internal) D phase in this *CNT* can be obtained in the same way. Here, $E_{G-G} \approx -2.9 \times 30 = -87$ kcal/mol, due to partial overlap of the *GNR* edges, and the symmetry term is $E_{sym} \approx 0$, due to unfavorable angle φ [108]. Therefore, the total coupling energy is $E_{total} \approx E_{ela} + \langle E_{C-G} \rangle + E_{G-G} \approx 420 - 6720 - 87 \approx -6387$ kcal/mol.

From these results, it would seem that the system in the internal A phase is by ≈ 60 kcal/mol less stable than the D phase. In fact, direct evaluation by *VMD* [43] of the total energies in these two simulated systems, shows that the system in the A phase is by ≈ 70 kcal/mol more stable than in the D phase. Therefore, the phase A is thermodynamically stable, while the phase D is only kinetically stable. The reason of this inversion might be due to slightly different *GNR* curvature, *CNT* deformations, symmetry coupling, and other phenomena not captured in Equation 4.2. For example, if we assume that the radius R_G of the *GNR* in the A phase is $\approx 18\%$ larger than that in the D phase, then Equation 4.2 gives the same energy difference between these phases as the simulations.

Next, we test if the previous system can be prepared with a locking angle shifted by 60° from that in the A phase. Since $E_{sym}(2.5 \text{ nm}^2) \approx k\,T = 0.597$ kcal/mol at $T = 300$ K, small *GNRs* can be easily thermally decoupled from their symmetry-locked positions. Therefore, we simulate the systems at $T = 200$ K and use the Langevin damping coefficient of 0.05 ps^{-1}.

As shown in Figure 12a,b, we can stabilize helical structures with a larger pitch of *GNRs* locked on the interior (exterior) surface of the (60,0) *CNT*. The model coupling energy of the

locked helical structure in Figure 12a, $E_{total} \approx E_{ela} + \langle E_{C-G} \rangle + E_{sym} \approx 420 - 6720 - 30 \approx -6330$ kcal/mol, is the same as in the A phase. Therefore, the locked helical phase is by ≈ 60 kcal/mol less stable than the D phase, while *VMD* gives (at $T = 300$ K) the energy difference for these systems of ≈ 80 kcal/mol. When we increase the temperature in the simulations to $T \approx 500$ K, this helical locked structure switches to the D phase.

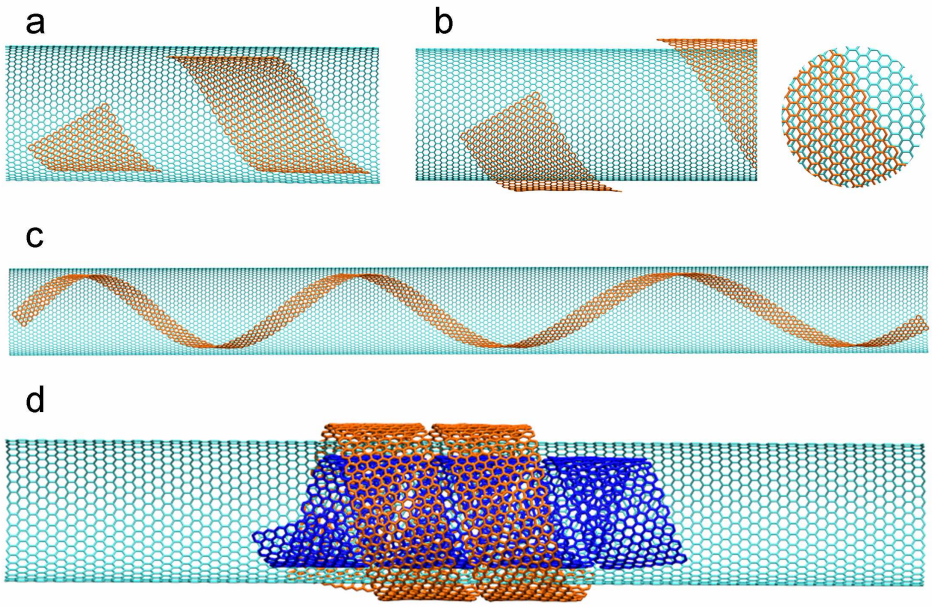

Figure 12. (a) Helical locked *GNR* (40×3 nm^2) inside a (60,0) *CNT*. (b) The same outside this *CNT* and detail of the locked structures. (c) Loosely helical folded *GNR* (60×1 nm^2) when it is placed inside the $l_C = 50$ nm long (60,0) *CNT*. (d) Two *GNRs* (25×2 nm^2) helical folded and *vdW* coupled over the wall of the (60,0) *CNT* (front parts of all the *CNTs* and *GNRs* (a-b) are removed for better visualization).

We continue by examining how *GNRs* self-assemble inside *CNTs* of finite lengths, when $l_G > l_C$. We place a *GNR* (60×1 nm^2) straight inside a (60,0) *CNT* ($l_C = 50$ nm). The *GNR* tends to maximize its overlap with the shorter *CNT*, due to *vdW* binding. Therefore, it forms a loose helical structure with both *GNR* ends present inside the *CNT*, as shown in Figure 12c. In contrast to the helical locked cases seen in Figure 12a,b, this structure with a large pitch is stabilized by the finite length of *CNT*. Therefore, when the *CNT* length is shorter, so is the pitch of the helice, until it becomes so dense that the *GNR* switches to the more stable D phase. The same structures are also formed outside finite *CNTs*.

We also explore the self-assembly of two *GNRs* (25×2 nm^2) initially placed on the opposite sides of the (60,0) *CNT* wall. Since the *GNRs* weakly interact by *vdW* coupling over the *CNT* wall, their self-assembly is correlated. As shown in Figure 12d, the *GNRs* form *overlapping* helical structures on both sides of the wall. It turns out that the external *GNR* induces the folding of the internal *GNR*, including its helicity. When the external *GNR* is removed from the system, the internal *GNR* does not even fold.

4.3.4 More complex nanostructures

In the above described manner, one could in principle assemble arbitrary planar graphene nanostructures on the surfaces or in the interior of *CNTs*. Here, we test this idea on the self-assembly of a "hair-brush" like graphene nanostructure with four *GNRs* (60×2 nm^2). One end of all four *GNRs* are connected to the remaining part (40×100 nm^2) of the graphene sheet, and the distance between the adjacent *GNRs* is 5 nm, as shown in Figure 13a. Initially, the tips of all four *GNRs* are placed on the (20,0) *CNT*. They start to fold around it, and after

$t \approx 4$ ns, they form a single layer ring structures on the *CNT*. Within another $t \approx 3$ ns, the *GNRs* make a multilayered ring structure. The rest of the graphene sheet also folds on the multilayered ring structures, and eventually completely wraps around the *GNRs*, as shown in Figure 13b,c. Then, we equilibrate the self-assembled structure, remove the *CNT* from its core, and equilibrate the remaining folded graphene. Upon removal, the diameter of the four rings slightly expands by 0.2 nm, as shown in Figure 13d,e, but the system retains the same shape, stabilized by the top graphene monolayer.

It is interesting to explore the self-assembly dynamics of such hair-brush structures when the *CNT* is positioned differently. For simplicity, we use two (20×1 nm^2) *GNRs*, connected to a (5×1 nm^2) graphene sheet, where the distance between the *GNRs* is 3 nm. Initially, we place a (20,0) *CNT* with fixed ends perpendicularly between the two *GNRs*, close to their tips. Within $t \approx 0.5$ ns, the *GNRs* fold around the *CNT*. After another $t \approx 1.5$ ns, the *GNRs* cross each other and make a knot around the *CNT*. Then the ends of the two *GNRs* propagate on the *CNT* surface in a spiral manner and eventually make a tight knot on the *CNT*, as shown in Figure 13f. This example illustrates that *GNR* self-assembly can be controlled by positioning the *CNTs* differently.

GNRs might be also used as nanomechanical connecting materials. We test if such "nanoglue" formed by a *GNR* (60×2 nm^2) can hold together two crossed (20,0) *CNTs*. Initially, the *GNR* is folded around two parallel *CNTs* (one with fixed ends) in a form of multilayered ring structure. After equilibration, we start to rotate one *CNT* with respect to the other by applying the force of $f = 0.01$ kcal/mol/Å to one of the edge atoms of the *CNT* with free ends. As the chosen

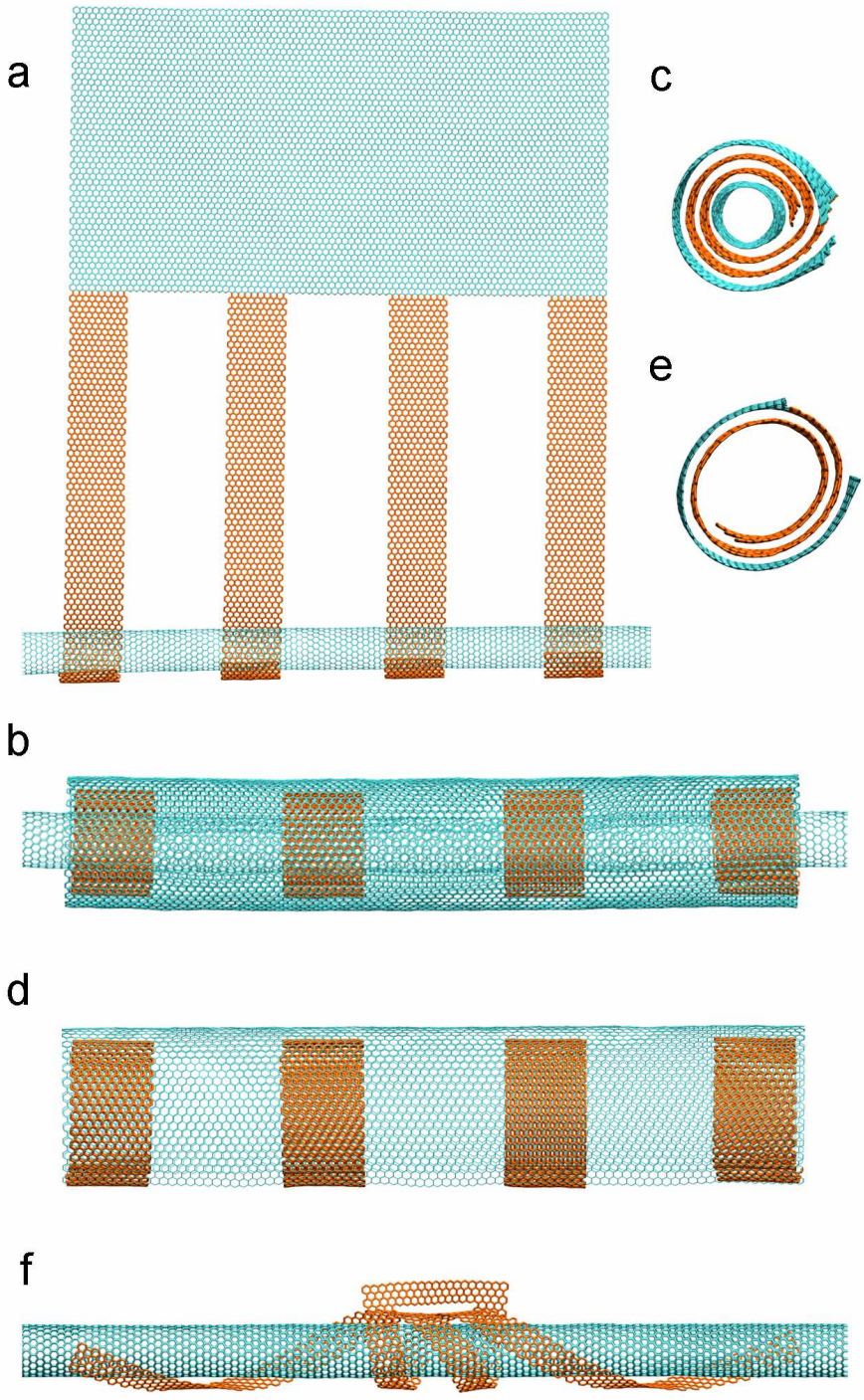

Figure 13. Graphene rings and knot formations from structured graphene flakes self-assembled on the *CNT* surface. (a-c) The formation of multiple *GNR* rings, covered with a single layer graphene sheet, on the (20,0) *CNT*. (d-e) After removal of the *CNT*, the multi-ring structure, covered with a single layer graphene sheet, is stabilized. (f) When the (20,0) *CNT* is placed between two connected *GNRs* a complex knot is formed.

CNT rotates, the *GNR* ring starts to slightly unfold. Once the *CNTs* are perpendicular to each other ($t \approx 1.5$ ns), we fix their mutual rotation and obtain the system shown in Figure 14a,b.

Next, we apply the force of $f = 0.01$ kcal/mol/Å, oriented upwards, to the edge atoms at both ends of the relaxed *CNT*. This is the minimum force under which the *CNT* moves upwards. Under this force, the *GNR* starts to unfold and a 5 nm gap is formed between the two perpendicular *CNTs* within $t \approx 1$ ns. At this position, we remove the force and allow spontaneous vertical translation of the relaxed *CNT*. Within $t \approx 1$ ns, the system comes back to its starting position, shown in Figure 14a,b. In order to reproduce the original structure, we should not separate the *CNTs* by more than ≈ 5 nm, due to *GNR* restructuring. We might strengthen the *GNR-CNT* wrapping by using structured or chemically functionalized *GNRs* [109].

We also test if *GNRs* can wrap around other materials to functionalize, strengthen, or glue them. We take thirty six parallel polyethylene $[-(CH_2)_n-]$ chains, each with 200 ethylene units. After equilibration for $t = 10$ ns at $T = 300$ K, the polyethylene chains form a bundle. Then we place a $(40 \times 2$ nm$^2)$ *GNR* tip at the bundle, perpendicularly to its orientations. Initially, the tip starts to form a *GNR* helix on the bundle. After $t \approx 5-10$ ns, the helical *GNR* refolds on the bundle, resembling a roll shown in Figure 9. The *GNR* also become covered with the loose polyethylene chains. As the *GNR* rolling continues, the polyethylene chains start to roll with the *GNR* and, within $t \approx 10$ ns, the system acquires the form shown in Figure 14c,d.

Finally, we investigate the self-assembly of *GNRs* on *CNTs* solvated in hexane and ethyl alcohol. Initially, a *GNR* (30×3 nm^2) is placed perpendicularly to the surface of solvated (60,0)

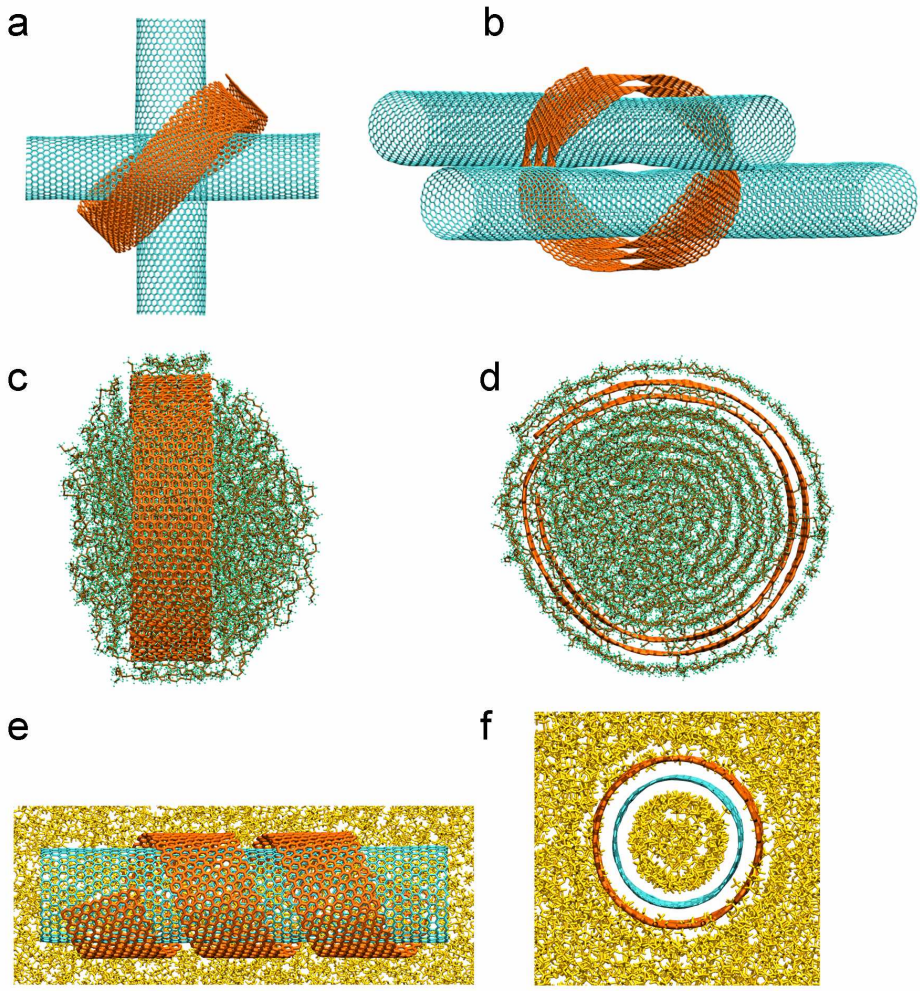

Figure 14. Binding of *CNTs* and polyethylene by graphene nanoribbons. (a) Top view and (b) side view of two crossed *CNTs* (20,0), tied by a 60×2 nm^2 *GNR*. (c-d) Polyethylene chains wrapped by a (40×2 nm^2) *GNR*. (e-f) Helical rolling of a *GNR* (20×2 nm^2) when placed at the angle of $\varphi = 60^\circ$ with respect to the axis of the $l = 15$ nm (30,0) *CNT* in hexane (front part of solvent is removed for better visualization).

CNT at $T = 300$ K (*NPT* ensemble). The *GNR* tip starts to fold on the *CNT*, and after $t \approx 1$ ns, it goes once around its circumference. To proceed in hexane (not in ethyl alcohol) further, and form a multilayered ring, as in Figure 9a-d, we need to heat the system to $T = 375$ K. Next, we test folding of the helical structure with the *GNR* (20×2 nm^2) on (30,0) *CNT* at an angle of $\varphi = 60^0$ with respect to *CNT* at $T = 300$ K. The *GNR* folds in a spiral manner, as in Figure 14e,f, without the necessity of heating. The formed helical structure is looser than in vacuum, since the solvent molecules fill the gaps between the individual *GNR* stripes. Very recently, spontaneous formation of carbon nanoscrolls on *CNTs* has been also simulated on a substrate [110].

4.4 Conclusion

In this chapter, we have demonstrated that carbon nanotubes can activate and guide the self-assembly of planar graphene nanostructures on their surfaces and in their interiors in vacuum and in solvents. Since the presented processes depend on the initial conditions, we can call them more precisely a controlled or guided self-assembly. The self-assembly can proceed by sliding, folding, and rolling motions, leading to stable or metastable bulky nanostructures, such as knots, rings, and helices. In the case of *GNRs* self-assembled on *CNTs*, the *GNR-CNT* coupling energy increases from the least stable helical locked phase, to the helical phase and the stable straight phase. For *GNRs* and *CNTs* with different symmetries, other possible arrangements might be formed and stabilized differently. The *GNRs* can also hybridize with other nanostructures. The novel hybrid materials are expected to have unique mechanical, electrical and optical properties [101], and numerous potential applications.

CHAPTER 5

CONTROLLED SELF-ASSEMBLY OF FILLED MICELLES ON NANOTUBES

5.1 Introduction

In this chapter, we have used coarse-grained MD simulations to show that hydrated lipid micelles of preferred sizes and amounts of filling with hydrophobic molecules can be self-assembled on the surfaces of carbon nanotubes. We simulate micelle formation on a hydrated carbon nanotube with an open end that was covered with amphiphilic double-headed or single-headed lipids and filled with hexadecane molecules. We show that kinetically stable micelles filled with hexadecane molecules are sequentially formed at the nanotube tip when the hexadecane molecules inside the nanotube are pressurized and the lipids on its surface were dragged by the water flowing around it. We investigate the stability of the thus-formed kinetically stable filled micelles and compare them with thermodynamically stable filled micelles that were self-assembled in the solution. This research was conducted by myself. The following contents are reproduced with permission from J. Am. Chem. Soc., 133(16):6146-6149, 2011. Copyright (2011) American Chemical Society (see appendix).

In recent years, nanomedicines with unique characteristics have been developed [61, 111]. Among the many tested systems, lipid and polymeric micelles [112] and nanoparticles self-assembled from amphiphilic block copolymers [113] have become particularly promising drug

nanocarriers. Typically, the micelle carriers have multishell molecular structures with compact hydrophobic cores separated by narrow charged layers from loosely ordered hydrophilic external shells [114]. These chemically distinct layers allow nesting and delivery of different drugs [80], proteins [115], and other molecules that are poorly soluble in water [116, 117].

Hydrated amphiphilic molecules, such as phospholipids or surfactants, tend to self-assemble into *thermodynamically stable* micelles above their critical micelle concentrations (CMCs) [118]. The micelles can be filled in a stepwise manner with hydrophobic molecules [114], but their stabilization may be a relatively complex process. Moreover, the average sizes and shapes of these micelles and the amounts of molecular cargo filling them are determined by the character of the monomers and the solutions used in their preparation. In various applications, it might be of interest to prepare kinetically stable micelles with relatively long lifetimes that can have controllable sizes and be filled with different types and numbers of molecules.

In this work, we investigated the possibility of controlling the self-assembly of kinetically stable micelles prepared and filled with a molecular cargo at nanoscale material surfaces. We used the fact that hydrated lipids spontaneously form hemimicelles [119] or cylindrical micelles [120], depending on the type of lipids used [121–123], on the hydrophobic surfaces of carbon nanotubes (CNTs) [124, 125]. These premicelles might be dragged on the CNT surfaces [103, 126, 127], filled with molecules at the CNT tips, and sequentially released, in close analogy to microsyringes or nanoscopic jets [128]. The amphiphilic lipids forming the micelles can be adsorbed on the CNTs from the solution, and the molecules filling the micelles could be

continuously supported through the CNT interior. In dip-pen nanolithography [129], various molecules can be analogously deposited on material surfaces by nanoscopic tips.

5.2 Computational Methods

We studied the self-assembly of filled micelles on CNT surfaces by classical molecular dynamics (MD) simulations. In order to describe these large systems with long and complex dynamics [130, 131], we performed coarse-grained MD (CGMD) simulations [50, 51, 132, 133], with the NAMD package [30] and the Martini 2.0 force field [51]. We modeled two types of amphiphilic lipids that potentially can form different micelles [122], having either one $[CH_3(CH_2)_{14}CH_2((CH_2OCH_2CH_2)_2\ (CH_2COCH_2))_4H]$ or two $[CH_3(CH_2)_{14}CH(((CH_2OCH_2CH_2)_2\ (CH_2COCH_2))_2H)_2]$ hydrophilic heads and a single hydrophobic tail.

Coarse graining of the lipids was performed through a four-to-one atom-mapping procedure [51] where every four non-hydrogen atoms in the lipids were modeled as a single bead. The CG hydrophobic tails were represented by C_1-type beads [$CH_3(CH_2)_2CH_3$, butane] [51], while the hydrophilic heads were represented by Na-type (C_3=O, 2-propanone) and N_0-type (C-O-C_2, methoxyethane) beads. We used 2:1 mapping of the carbon atoms in the considered (40,0) CG CNT in order to preserve its hexagonal symmetry [51]. Every two neighboring carbons in the allatom CNT were modeled as an SC_4-type bead. Similarly, every four water molecules were united into a single P_4-type bead [51], and the hydrophobic hexadecane molecules filling the CNT were modeled by C_1-type beads [51].

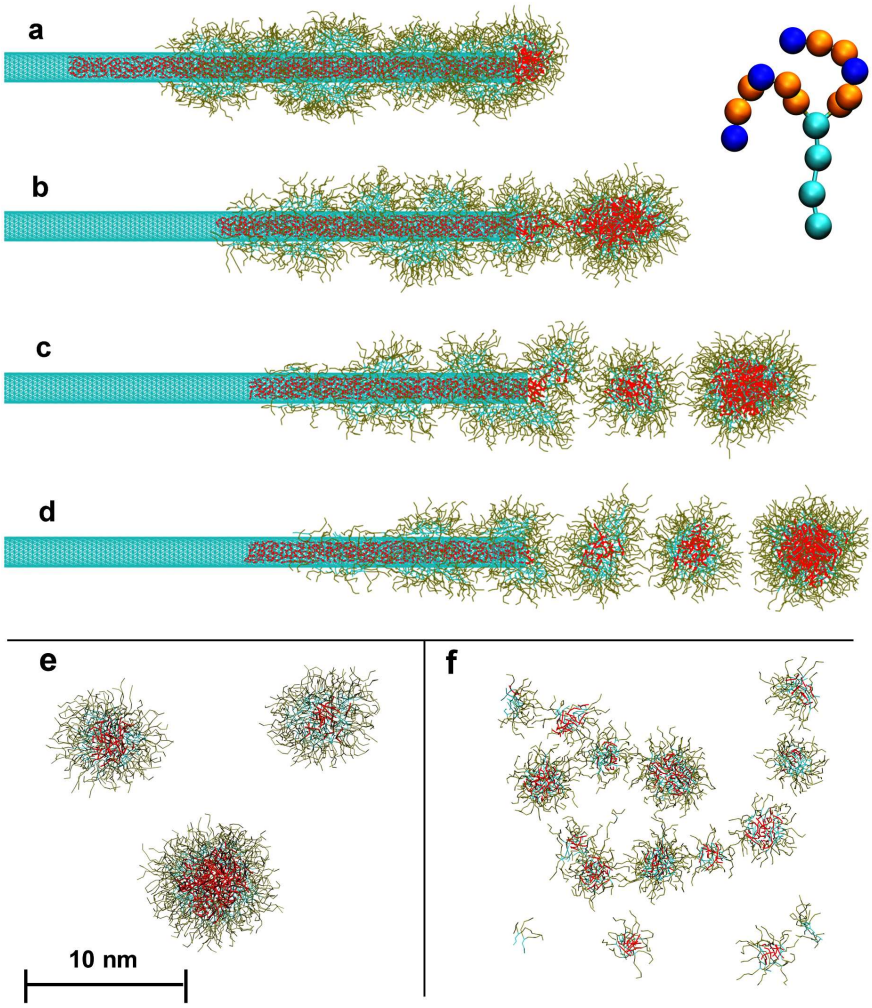

Figure 15. Controlled self-assembly of hydrated double-headed lipid micelles filled with hexadecane. (a) Lipids deposited on the CNT form random hemimicelles after 20 ns. (b-d) Micelles with kinetically controlled sizes and filling are sequentially formed at the CNT tip when the hexadecane molecules in the CNT interior are pressurized and the lipids on its surface are dragged by the water flowing around it. The inset shows a single biheaded lipid molecule. Color scheme: red, CG hexadecane; gray, hydrophilic lipid head; cyan, hydrophobic lipid tail. (e) Three hexadecane-filled micelles from (d) after 400 ns of equilibration. (f) Thermodynamically driven self-assembly of double-headed lipid monomers and hexadecane in water for the same system as in (d). After 300 ns of equilibration, the sizes of the micelles and their filling are largely random.

5.3 Results and Disussion

5.3.1 Double-headed lipid micelles

First, we studied the self-assembly of biheaded lipids, shown in the inset of Figure 15. The large size (two chains) of their polar heads relative to their hydrophobic tails means that these hydrated lipids (alone) prefer to self-assemble into smaller micelles [122]. In our simulations, we fixed the CNT, covered it with 450 lipids, and filled it with 400 hexadecane molecules. The system was hydrated, placed in a cell of dimensions $16 \times 16 \times 70$ nm^3 with periodic boundary conditions applied, and simulated at $T = 350$ K in the NPT ensemble. We used the Langevin piston method [134] with a damping coefficient of 1 ps^{-1}. In order to prevent artificial freezing of CGMD water at low damping, we used antifreeze water beads (8% of the total normal water beads) [51].

Figure 15 shows the sequential self-assembly of lipid micelles with a controllable amount of hexadecane filling on the (40,0) CNT. Upon deposition on the CNT, these lipids formed random hemimicelles within 20 ns [110, 124, 135], as shown in Figure 15a. Next, we applied on each water bead the force $f_1 = 2.08$ pN oriented toward the CNT right tip. As a result, water flowed with average velocity $v_t = 1.5$ m/s and dragged the lipids adsorbed on the CNT surface. Hexadecane molecules inside the CNT were also pressurized by application of the force $f_2 = 1.39$ pN on each of their beads, oriented in the same way as f_1. In experiments, loosely separated CNTs may be fixed and their entrances and exits may be immersed in two separated solutions. The external solution might be pumped to flow around the adsorbed lipids, while the intercalated molecules could be driven by pressure.

Upon application of these forces, the lipid and hexadecane molecules started to move toward the CNT tip, and soon the first hemimicelle covered the CNT tip. Within 4 ns, a micelle of diameter $d \approx 5$ nm containing ≈ 100 hexadecane molecules formed and detached from the CNT tip, as shown in Figure 15b. When it left, the remaining lipids and hexadecane molecules moved forward, and the next hemimicelle covered the CNT tip in a similar fashion. The second filled micelle had $d \approx 3$ nm and contained ≈ 40 molecules. The third filled micelle was then created, and so on. The formed micelles had different sizes, since the progression of both sets of molecules did not remain steady as their amounts decreased. As the micelles formed and detached, fewer hexadecane molecules were present inside the CNT, which (in our simulations) exerted a smaller total force on the CNT closure. For the same reason, the progression of lipids on the CNT surface also became slower.

The sizes and filling of these kinetically stabilized micelles might be controlled by the CNT diameter and the forces applied on the two sets of molecules. In principle, the micelles should form already at very small velocities of the lipid and hexadecane molecules, which were beyond the reach of our simulations. When we increased the velocity of water ($f_1 = 2.78$ pN, $f_2 = 1.39$ pN), we observed the formation of small micelles with only a few hexadecane molecules. When we also increased the velocity of hexadecane, larger micelles with more hexadecane were formed. When the velocities of the hexadecane molecules were too high relative to that of water ($f_1 = 1.39$ pN, $f_2 = 3.77$ pN), the slowly moving lipids did not have time to cover the progressing hexadecane molecules, which started to pass through the partially formed micelles at the CNT

exit. These results show that kinetics, thermodynamics, and hydrodynamics all play a role in micelle formation, filling, and detachment from the CNT tip.

In order to test the stability of the thus-formed filled molecular assemblies, we separated the three micelles shown in Figure 15d and evolved them in an isolated cell ($20 \times 20 \times 40$ nm^3) as before. As shown in Figure 15e, the micelles were fully stable for 400 ns. In reality, the micelles could be stable for much longer times, during which they could be applied in various ways.

We compared these kinetically stabilized micelles with micelles formed by thermodynamic stabilization from hydrated lipid and hexadecane monomers. To do so, we heated the system in Figure 15e for a short time, until the micelles disintegrated into their hydrated components, i.e., 305 biheaded lipids (concentration of 3.8×10^{-2} M) and 206 hexadecane molecules. Next, we cooled the system back to $T = 350$ K and simulated it as before. We observed that within 10 ns, the lipids formed many small micelles of different sizes, filled with random numbers of hydrophobic hexadecane molecules. Within 20 ns, all of the hexadecane molecules were located inside the micelles. Later, smaller micelles merged and formed larger micelles, as shown in Figure 15f for 350 ns long simulations. The sizes of the formed micelles and the numbers of hexadecane molecules stabilized inside them fluctuated significantly in these simulations. In larger volumes, the micelle parameters should stabilize at longer times and depend on the used molecules and solution. Experimental preparation of such thermodynamically stabilized filled micelles allows only limited variation of the types and numbers of molecules present inside the

micelles. In contrast, the outlined approach allows controlled self-assembly of kinetically stable micelles with variable parameters.

5.3.2 Single-headed lipid micelles

To further extend these ideas, we also tested the self-assembly of hexadecane-filled micelles formed by single-headed lipids. In solutions, similar lipids (alone) at concentrations above the CMC tend to form tubular structures called bicelles or planar bilayers [122], as a result of the limited steric strain caused by the absence of the second hydrophilic head [122]. We prepared a system formed by 1000 lipid molecules adsorbed on the (40,0) CG CNT and 400 hexadecane molecules filling the CNT. The simulation conditions were the same as before.

In Figure 16a, we can see that after 20 ns of equilibration, these single-headed lipids cylindrically wrapped around the CNT. Once the self-assembled lipids were dragged by the flowing water, the CNT tip was covered within 5 ns by the first cylindrical hemimicelle. This time, a filled tubular bicelle was formed. About 20 ns later, a bicelle with $d \approx 3$ nm and length $l \approx 20$ nm was filled with ≈ 200 hexadecane molecules. As a result of initial fluctuations of the lipid density, the bicelle was eventually cut off and detached from the CNT tip, after which the formation of the second bicelle continued.

Although these lipids seemed to self-assemble into bicelles, it was not clear whether the molecular assemblies would retain their elongated shape. To estimate their stability, we separated the bicelle formed Figure 16d and evolved it in an isolated $20 \times 20 \times 37$ nm^3 cell as before. We observed that the bicelle was stable for 30 ns, at which point it started to gain a spherical shape. Eventually, a large filled micelle was formed, as shown in Figure 16e for 375

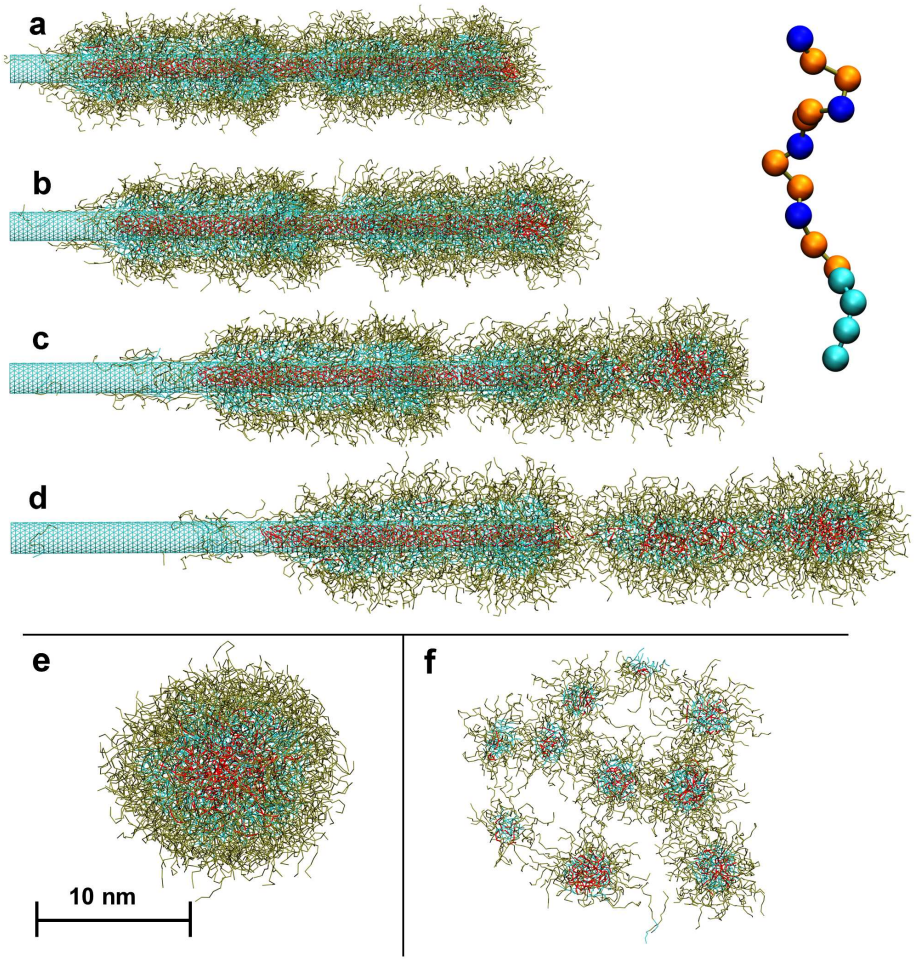

Figure 16. Controlled self-assembly of hydrated single-headed lipid bicelles filled with hexadecane. (a) Lipids deposited on the CNT form random tubular structures after 20 ns. (b-d) Bicelles with kinetically controlled sizes and filling are sequentially formed at the CNT tip when the hexadecane molecules in the CNT interior are pressurized and the lipids on its surface are dragged by the water flowing around it. The inset shows single single-headed lipid molecule. Color scheme: red, CG hexadecane; gray, hydrophilic lipid head; cyan, hydrophobic lipid tail. (e) Hexadecane-filled bicelle from (d) after 375 ns of equilibration. (f) Thermodynamically driven self-assembly of single-headed lipid monomers and hexadecane in water for the same system as in (d). After 450 ns of equilibration, the sizes of the micelles and their filling are largely random.

ns long simulations. These results indicate that single-headed lipids with the right structure might assemble on CNTs into kinetically stable bicelles. Using the described methodology, we could potentially control the sizes and filling of these kinetically stable molecular assemblies of single- and double-headed lipids.

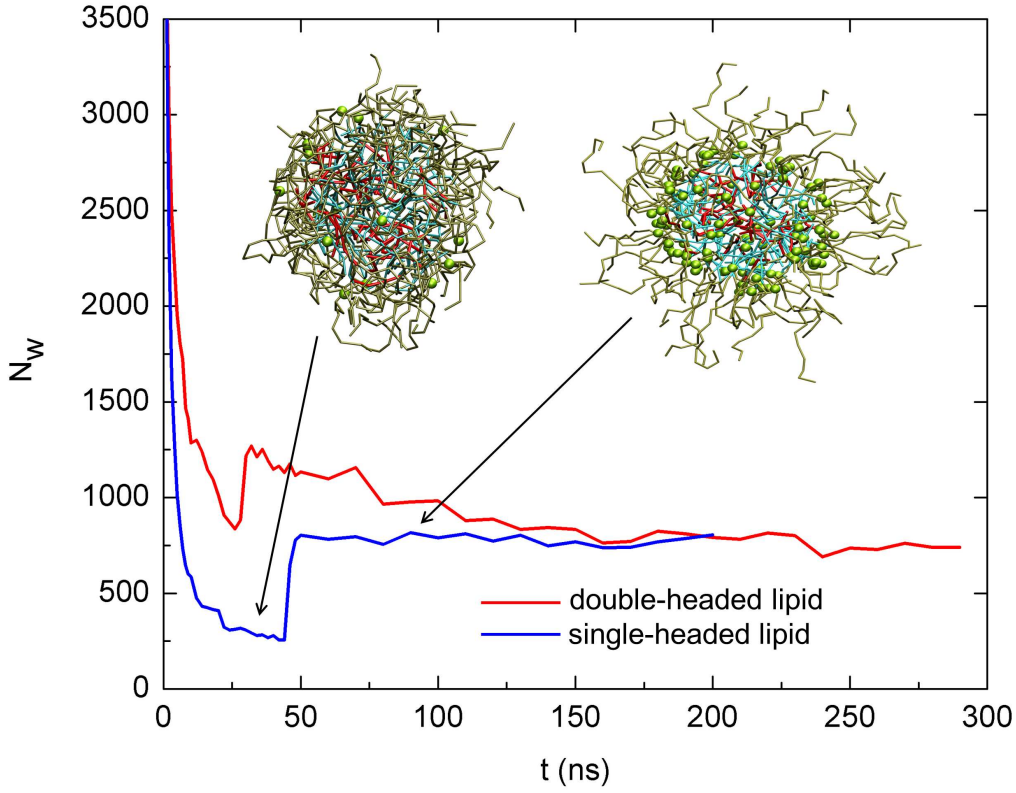

Figure 17. Number of water molecules present within 0.5 nm (first monolayer) of the hydrophobic micelle core during the self-assembly of hydrated double-headed (red) and single-headed (blue) lipid monomers into micelles filled with hexadecane. The inset shows different forms of one micelle selected from the system of self-assembling single-headed lipid monomers.

As in the previous case, we tested the thermodynamic stabilization of the filled micelles from the hydrated lipid and hexadecane monomers. We heated the hydrated micelle in Figure 16e until it disintegrated into 490 single-headed lipids (concentration of 7.2×10^{-2} M) and 184 hexadecane molecules. Next, we cooled the system back to $T = 350$ K and simulated it. Within 10 ns, the lipids formed small micelles of different sizes, and in the next 20 ns, all of the hexadecane molecules filled them. Eventually, smaller micelles merged and formed bigger micelles, as shown in Figure 16f, which were obtained for 450 ns simulations. Again, the micelle sizes and the numbers of hexadecane molecules inside them fluctuated significantly in these relatively short simulations. The parameters might later fluctuate less, but their absolute values could not easily be controlled in thermodynamic stabilization.

To test the equilibration of these micelles self-assembled from the two kinds of lipid monomers (Figure 15f and Figure 16f), we calculated the total numbers of water beads (N_w) within a distance of 0.5 nm (first layer) from their hydrophobic cores. Figure 17 shows that with progressing self-assembly, N_w initially largely decreased in both systems from the initial value of $N_w \approx 7000$. In the single-headed (double-headed) lipid system, N_w approached a minimum at 40 ns (25 ns) due to initial hydrophobic collapse [136] of the lipids. Next, the micelles started to swell, and some water beads reached the hydrophobic surface of the core. Eventually, the numbers of water beads (accessible surface) at the micelle cores stabilized, and the systems equilibrated.

5.4 Conclusion

In this chapter, we have shown that kinetically stable micelles filled with molecules that are poorly soluble in water could be prepared on CNT surfaces. The sizes and filling of the formed

micelles could be controlled by the preparation conditions, such as the sizes of the nanotubes and the preparation speed. The lifetimes of the formed micelles depend on their size, the monomers used, the molecules carried, and the solution. Other nanostructures might also potentially be used in the controlled self-assembly of filled micelles. The outlined methodology has potential applications in molecular storage, protection, manipulation, and delivery.

CHAPTER 6

POROUS CARBON NANOTUBES: MOLECULAR ABSORPTION, TRANSPORT, AND SEPARATION

6.1 Introduction

In this chapter, we use classical MD simulations to study nanofluidic properties of porous carbon nanotubes. We show that saturated water vapor, condensed on these nanotubes, can be absorbed by them and transported in their interior. We also show that porous carbon nanotubes can also be used as selective molecular sieves. This research was conducted by Ms. Irena Yzeiri and myself. While both of us participated in all the aspects of research (designing the systems, carrying out the simulations, analyzing data, writing the manuscript), Irena contributed more to several aspects of this research project.

Carbon nanotubes (CNTs) have many unique applications in nanofluidics, such as the possibility to drag molecules [126, 137], sense their flows [138, 139], separate molecules [140–143], and desalinate solutions [144, 145]. Recently, porous graphene (PG) with chemically functionalized nanopores has been introduced [146] and intensively tested for potential applications in molecular separation [147, 148], DNA sequencing [149, 150], and electronics [151].

In principle, one could also introduce nanopores of tunable sizes, shapes, and chemistries in CNTs with the goal to combine nanofluidic properties of PG and CNTs. Recently, such porous carbon nanotubes (PCNTs) were synthesized with nanopores of the diameters $d_p \approx 4 - 10$ nm,

arranged either randomly [152] or in high density arrays [153]. Mechanical properties of these PCNTs depend on the pore sizes, symmetries, and densities [154, 155].

In this work, we examine by molecular dynamics (MD) simulations if PCNTs can inherit the nanofluidic properties of both PG and CNTs, which might result in nanochannels with *transversal* molecular selectivity and high *longitudinal* passage rates. To illustrate this idea, we study simultaneous molecular (transversal) absorption by PCNTs and (longitudinal) transport in their interiors. We also explore the possibility of ionic and molecular separation by arrays of charged and neutral PCNTs.

6.2 Computational Methods

We model all the above processes by classical MD simulations with the NAMD package [30], the CHARMM27 force field [29], and the TIP3P model for water. The (non-bonding) vdW coupling between ith and jth atoms is described by the Lennard-Jones potential,

$$V_{i,j} = \epsilon_{i,j} \left[(R_{min,i,j}/r_{i,j})^{12} - 2\,(R_{min,i,j}/r_{i,j})^{6} \right],$$
$$\epsilon_{i,j} = \sqrt{\epsilon_i\,\epsilon_j}, \qquad R_{min,i,j} = \frac{1}{2}\,(R_{min,i} + R_{min,j})\,, \tag{6.1}$$

where we use (C, O, H, Na^+, Cl^-) $\epsilon_C = -0.07$ kcal/mol, $R_{min,C} = 3.98$ Å, $\epsilon_O = -0.12$ kcal/mol, $R_{min,O} = 3.4$ Å, and $\epsilon_H = -0.046$ kcal/mol, $R_{min,H} = 0.44$ Å, $\epsilon_{Na^+} = -0.047$ kcal/mol, $R_{min,Na^+} = 2.72$ Å, $\epsilon_{Cl^-} = -0.150$ kcal/mol, $R_{min,Cl^-} = 4.54$ Å . The non-bonded cut-off and the pair-list distance are 10 Å and 12 Å, respectively. We neglected the PCNT polarization and model the system with the Langevin dynamics [42], the damping coefficient

of 0.01 ps^{-1} (non-physical momentum dissipation) [134] and use the time step of 2 fs. The electrostatic interactions in the ionic systems are calculated using the Particle Mesh Ewald (PME) method [31]. PME is neglected in the other systems that lack ions.

6.3 Results and Discussion

6.3.1 Condensation and transport of water within PCNTs

PCNTs might simultaneously absorb molecules from gas or liquid phases, and transport them away. To test this possibility, we condense an saturated water vapor on the (28,28) PCNT, as shown in Figure 18. The hexagonal nanopores have a diameter of $d_p \approx 0.5$ nm, and they are hexagonally arranged with ≈ 0.7 nm separations. The water over-saturation is necessitated by the hydrophobic character of the CNTs, which could be modified by their chemical functionalization to guarantee water collection at low vapor pressures. Functionalized PCNTs might complement the spectrum of currently used desiccants, such as silica gel [156], calcium sulfate and chloride [157], and other molecular sieves [158].

We place the (28,28) PCNT (25 nm long with fixed edge atoms) and $40,000$ water molecules in a box ($25 \times 27 \times 25$ nm^3) with periodic conditions applied. Initially the system is heated to $T = 600$ K to quickly vaporize the water and prepare the initial state of the system. Once it is slowly cooled to $T = 300$ K with a damping coefficient of 0.01 ps^{-1}, the vapor saturates, and condenses in the form of nanodroplets on the outer and inner PCNT surfaces, as well as in vacuum. Within $t \approx 1$ ns, droplets on both interior and exterior PCNT surfaces coalesce and interact through the nanopores, as seen in Figure 18a. The outer droplets are drawn by the inner droplets through the nanopores inside the PCNT, as seen in Figure 18b at $t \approx 6$ ns.

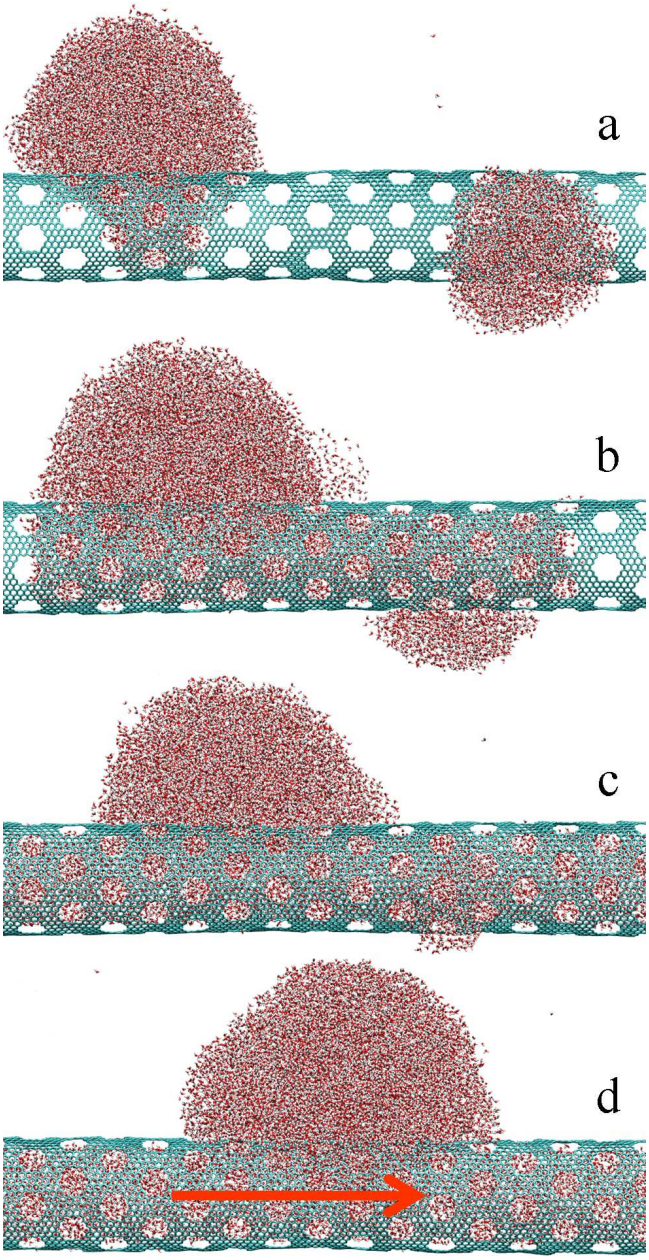

Figure 18. Condensation of 40,000 water molecules from an oversaturated vapor into a (28,28) PCNT: (a) $t = 1$ ns, (b) 6 ns, and (c) 10 ns. At $t = 10$ ns, a pressure of $P \approx 156$ atm is applied to water at the left PCNT entrance, causing the absorbed water to flow through the tube with a speed of $v_w \approx 1.86$ nm/ns, as shown in (d) at $t = 14$ ns. The droplet adsorbed onto the PCNT moves with the flow with its own velocity of $v_d \approx 0.88$ nm/ns.

Inside the PCNT, water has a lower energy due to additional van der Waals (vdW) coupling to the walls [159]. At $t \approx 10$ ns, the PCNT is filled with water and the remaining water forms droplets condensed on its surface, as seen in Figure 18c. Finally, we show in Figure 18d that the collected water can be pumped through the PCNT by a small force of $f = 0.001$ kcal/mol/Å ($P \approx 156$ atm), applied on all the water molecules (each O and H atom) at the first 2 nm of the PCNT entrance. The water stays within the PCNTs and flows with the average velocity of $v_w \approx 1.86$ nm/ns. The internal water remains within the PCNT upon this established flow and drags the outer nanodroplet with a velocity of $v_d \approx 0.88$ nm/ns. The same behavior is observed in PCNTs with diameters of $d_T \approx 2 - 6$ nm and pore diameters of $d_p \approx 0.5 - 1$ nm. Further simulations of PCNTs with triangular shaped pores also behave in the same way.

In Figure 19, we simulate a (40,40) CNT with one hexagonal pore $d_p \approx 1.5$ nm through which a nanodroplet with a diameter $d_w \approx 6$ nm is passing. To obtain these energies, we equilibrate the system while keeping different amounts of water inside the tube by fixing (upon local equilibration) a thin dome-like layer of water molecules around the pore. Each step is simulated for $t \approx 4$ ns, and the total energy is calculated from the last 500 frames by VMD [43]. The simulations reveal that the energy barrier for the water droplet to enter the PCNT pore (≈ 10 % of water inside) is $\Delta E_T \approx 50$ kcal/mol.

Although water nanodroplets can enter partly filled PCNTs relatively easily, these simulations show that they experience a barrier when entering an empty PCNT. In order to understand the barrier origin, we calculate the barrier energy for a water nanodroplet with a diameter of

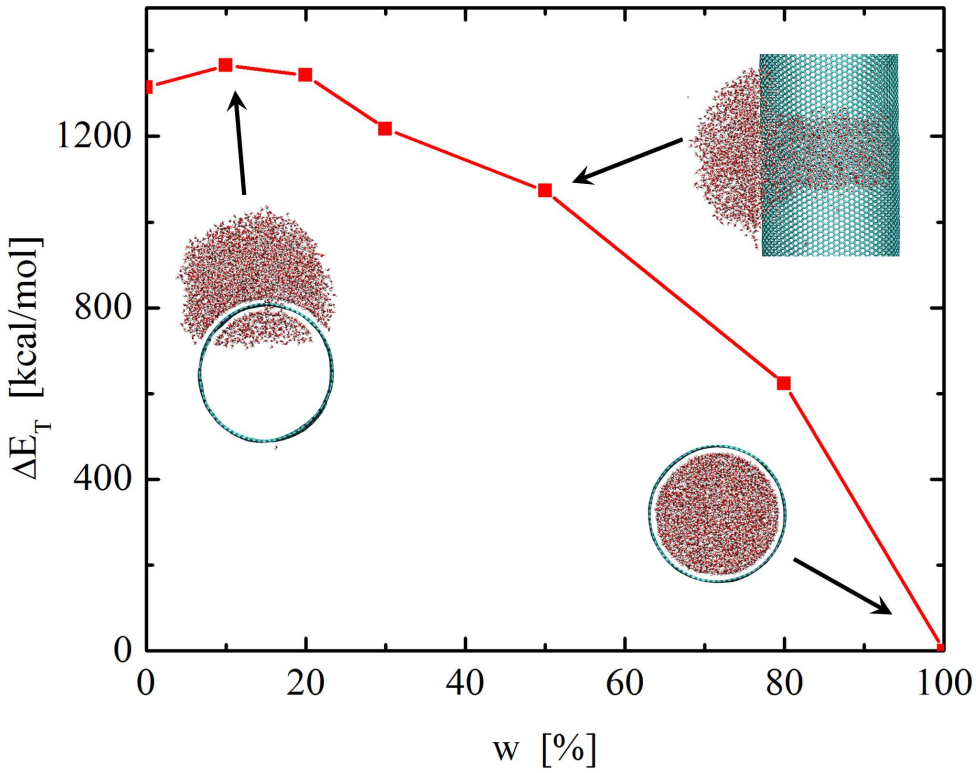

Figure 19. The total change in energy when a water nanodroplet ($d_w \approx 6$ nm) enters inside a (40,40) PCNT through a single pore ($d_p \approx 1.5$ nm). Here, w is the relative amount of water inside the CNT.

$d_w \approx 4$ nm passing through a single hexagonal pore ($d_p \approx 1.5$ nm) formed in a flat graphene sheet. We use the formula,

$$\Delta E_{total} = \gamma_{H_2O}\,\Delta A_s + \gamma_{w-c}\,\Delta A_{w-c} + \Delta E_{elec}\,, \tag{6.2}$$

where $\gamma_{H_2O} \approx 0.0715$ J/m^2 (≈ 10.36 kcal/mol/nm^2) is the free surface energy density of water [160], ΔA_s is the change in the free surface area of the water droplet (not in contact with graphene), $\gamma_{w-c} \approx -20.8$ kcal/mol/nm^2 is the vdW coupling energy density between water and graphene [103], ΔA_{w-c} is the change in the water-graphene contact area, and ΔE_{elec} is the difference in electrostatic energy of the system obtained from VMD (water rearrangement; graphene not polarizable). When we calculate the barrier using Equation 6.2, we assume that initially the droplet is adsorbed onto a graphene with a pore in its center and then one half of the droplet is passed through the pore. This gives the barrier energy of $\Delta E_{total} \approx 45$ kcal/mol, which is close to the value of $\Delta E_{total} \approx 40$ kcal/mol, obtained for the same system using VMD. When the droplet enters a PCNT, additional corrections need to be added due to the curvature of the tube. Therefore, due to this barrier liquid water can not enter initially empty PCNTs.

6.3.2 Exchange of ions using PCNTs

Charged CNTs can attract solvated ions onto their surfaces [161–164]. If PCNTs are charged and solvated in ionic solutions, they should attract ions, adsorb them into their interior, and potentially separate them from the solutions. This might be useful in batteries [165], supercapacitors [166], and other ion-exchange devices. We briefly illustrate this idea on ion separation

with two (20,20) PCNTs placed 4 nm apart in $C = 0.2$ M NaCl solution. The nanopores with a diameter of $d_p \approx 0.5$ nm are hexagonally arranged with ≈ 0.7 nm separations. We fix the atoms at the PCNT edges, oppositely and homogeneously charge the two PCNTs (± 0.02e per carbon atom), and apply periodic boundary conditions to the system, so that ions only enter through the pores. The system is equilibrated at $T = 300$ K using the constant pressure and temperature (NPT) ensemble.

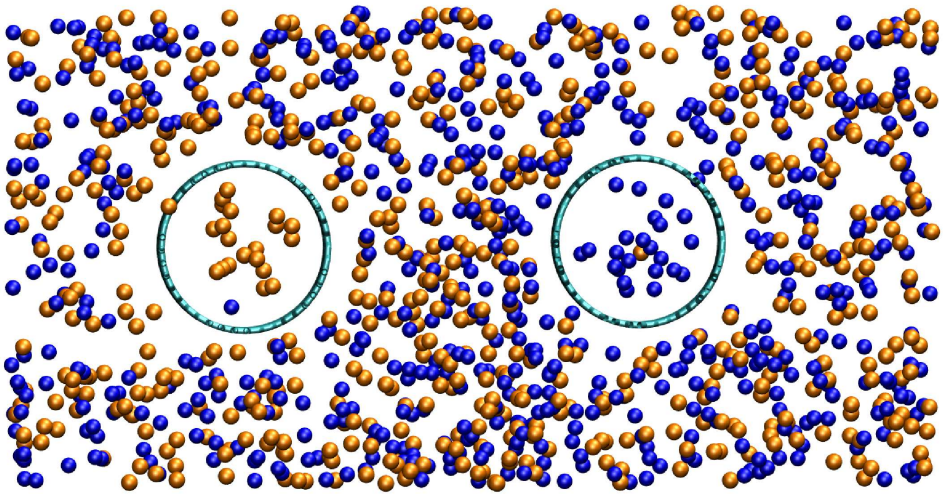

Figure 20. Separation of Cl^- and Na^+ ions from the 0.2 M NaCl solution using oppositely charged (± 0.02 e per carbon atom or ± 50.8 e per tube) (20,20) PCNTs, 10 nm in length, at $T = 300$ K.

In Figure 20, we show the system after $t \approx 10$ ns of equilibration. We can see that oppositely charged ions enter into different PCNTs, but only ≈ 44 % of the screening ions

enter each PCNT (curvature). The remaining screening ions are within the Debye length, $\lambda_D = \left(\epsilon\, k_B\, T/e^2\, N_A\, 2\, C\right)^{1/2} \approx 0.7$ nm, of each PCNT. Since the PCNT internal diameter is $d_T \approx 2\,\lambda_D$, predominantly ions of the same charge are seen in the PCNT interiors, which is important for their selective separation. When we apply a small force of $f = 0.001$ kcal/mol/Å to the water molecules at the first 2 nm of the PCNT entrance ($P \approx 110$ atm), the charged ionic solution inside each tube flows with a speed of $v_i \approx 0.81$ nm/ns. In principle, this allows for the replacement of the ions in the system. The selectivity, speed, and efficiency of this process can be tuned by the type of PCNTs and the solution used.

6.3.3 Separation of organic mixtures using PCNTs

Next, we examine if neutral PCNTs could be used in separation of molecules passing through their walls. Pristine CNTs with relatively small diameters ($d_t \approx 2$ nm) can separate ethanol from ethanol-water solution with very high efficiency and selectivity [167, 168]. However, the requirement of narrow CNTs is quite strong. Therefore, it would be very interesting if PCNTs with tunable pore sizes could separate such molecular mixtures. Different coupling between the molecules and potentially functionalized PCNTs might help in the separation process. We are particularly interested in separating organic compounds with similar boiling points, $\Delta T_b \approx 0$, which is hard to do by fractional distillation or alike methods.

Here, we test if plain (no functionalization) PCNTs could separate a mixture of benzene and ethanol, with $\Delta T_b \approx 2^\circ$ C ($T_{benzene} = 80.1^\circ$ C, $T_{ethanol} = 78.4^\circ$ C). We evaluate the separation efficiency depending on the PCNT diameter, temperature, and mixture composition. First, we simulate the molecular separation by (20,20), (28,28), and (40,40) PCNTs with hexagonal

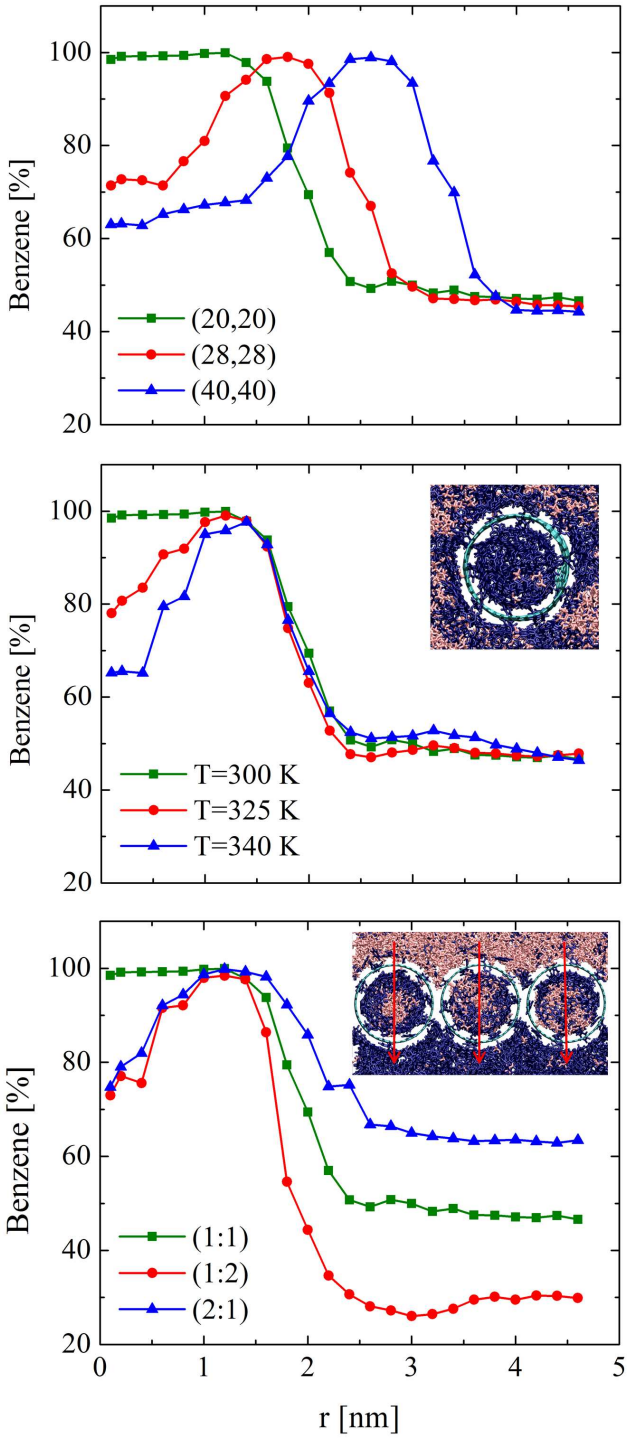

Figure 21. (top) Separation of the (1:1) benzene-ethanol mixture at $T = 300$ K with the (20,20), (28,28), and (40,40) PCNTs having $d_p \approx 1$ nm nanopores. (middle) The same in the (20,20) PCNT at different temperatures. (inset) The distribution of benzene (dark) and ethanol inside (20,20) PCNT after $t = 20$ ns of simulations. (bottom) Separation of the (1:1), (1:2), (2:1) benzene-ethanol mixtures in the (20,20) PCNT at $T = 300$ K. (inset) Separation of benzene from the benzene-ethanol (1:1) binary mixture at $T = 300$ K using a (20,20) PCNT membrane. Vertical arrows show direction of flow.

nanopores having a diameter of $d_p \approx 1$ nm, hexagonally arranged with ≈ 0.7 nm separations. The PCNTs are immersed in the (1:1) benzene-ethanol binary mixture in a $16 \times 11 \times 10$ nm ^{3} box with periodic boundary conditions applied. We simulate the systems in the NPT ensemble at $P = 1$ atm and $T = 300$ K.

Figure 21 (top) shows the equilibrated percentual radial distribution of benzene in these PCNTs. We calculate the distributions in cylindrical shells oriented along the PCNT axis and radially separated by 0.2 nm. One can clearly see that the molecular separation is possible in narrow PCNTs. The concentration of benzene inside the (20,20) PCNT is ≈ 98 %, while it is only ≈ 62 % inside the (40,40) PCNT. Therefore, PCNTs with smaller radii could separate molecules more efficiently, since all the molecules inside the tube either couple directly to the walls or they couple to the first layer of benzene adsorbed at the walls.

In the inset of Figure 21 (middle), we show the distribution obtained in the smallest (20,20) PCNT after $t = 20$ ns of simulations. We can clearly see that the PCNT interior is predominantly filled by benzene (dark) and so is its external surface. It is because benzene has a stronger vdW coupling to PCNT than ethanol; we have calculated by VMD the average vdW binding energy density for CNT-benzene (0.75 kcal/mol/atom) and CNT-ethanol (0.60 kcal/mol/atom) [169]. By changing the chemistry of the nanopores and PCNT interior, one might be able to control its separation ability.

In Figure 21 (middle), we study the effect of temperature on the separation efficiency in the (20,20) PCNT. We can see that as the temperature is increased from $T = 300$ K to $T = 325$ K and $T = 340$ K, the separation efficiency (average benzene concentration) drops from ≈ 98 %

to ≈ 90 % and ≈ 80 %, respectively. This is caused by the fact that thermal fluctuations tend to break the stronger benzene-nanotube vdW bonding, making the PCNT entrance for both types of molecules equally likely.

Finally, we investigate how the molecular separation efficiency depends on the composition of the binary mixture. We simulate the separation of the (1:1), (1:2) and (2:1) benzene-ethanol mixtures in the (20,20) PCNT. In Figure 21 (bottom), we observe that the separation is very efficient under the (1:1) conditions. However, as we increase the concentration of either component to (1:2) or (2:1), the separation efficiency decreases. This was expected for the (1:2) benzene-ethanol composition, but it is a rather unexpected result for the (2:1) composition. During closer inspection of our simulations, we observe clusters of ethanol forming under the (1:2) and (2:1) benzene-ethanol compositions, thus the solution does not appear to be uniformly homogeneous. This could be due to limited miscibility of benzene and ethanol or it could be that the PCNT may be introducing new phases within its interior. The conditions under which this occurs are unclear and further detailed studies may be necessary to explain this new interesting phenomena.

In the inset of Figure 21 (bottom), we also illustrate how PCNTs could be practically used in the separation of organic mixtures. We simulate the molecular passage through a membrane formed of adjacent parallel (fixed) (20,20) PCNTs with hexagonally arranged (0.7 nm apart) pores ($d_p \approx 0.5$ nm). The (1:1) benzene-ethanol mixture is placed on top of the PCNT membrane. A layer of dummy atoms placed 5 nm below the membrane prevents mixing of the solutions above and below the membrane (periodic system and NVT ensemble). The

solution above the PCNT membrane is pressurized by applying on all the solution atoms (5 nm above the membrane) a small force of $f = 5$ cal/mol/Å oriented normal to the membrane. As a result, the solution flows down, but predominantly benzene molecules are passing through the membrane, thus separating the binary mixture. After $t = 10$ ns, the molar ratio of benzene and ethanol below the PCNT membrane is 96 : 4. The separation efficiency may be improved by the use of multilayer membranes.

6.4 Conclusion

In this chapter, we have demonstrated that PCNTs could be used in selective molecular absorption, transport, and separation. We have shown that saturated water vapor can be absorbed on and pumped out by PCNTs, which might be used in active desiccation. Different types of ions can also be separated from ionic solutions and pumped away through charged PCNTs, which might be used in batteries and supercapacitors. PCNTs might also serve as molecular sieves, where molecules can be efficiently separated based on their coupling to PCNTs. Therefore, porous nanotubes made from atomic and molecular components can form an important class of materials with a broad range of applications.

CHAPTER 7

NANOMEDICINE I: DENDRON MEDIATED SELF-ASSEMBLY OF PEGYLATED BLOCK COPOLYMERS

7.1 Introduction

In this chapter, we characterize PEGylated dendron-based copolymers and their assemblies, which have the potential to become a new class of drug delivery platforms. The synthesis and experimental characterization of the studied systems was performed by the members of Prof. Seungpyo Hong's research group. The computational modeling was performed by myself and (currently Dr.) Lela Vuković. While both of us participated in all the aspects of research (preparing the systems, carrying out the simulations, analyzing data, writing the manuscript), Lela contributed more in parametrizing dendron-based polymers.

Self-assembled molecular nanoconstructs with controllable physical, chemical, and biological properties represent one of the most versatile platforms for drug delivery [170, 171]. Above their critical micelle concentrations (CMCs), linear and branched amphiphilic block copolymers can assemble into thermodynamically stable supramolecular structures of different sizes, morphologies, and properties [172, 173]. Among those copolymers, dendron-coils (DC) have attracted a great deal of scientific interest due to their unique structure and properties. A DC is comprised of a dendron, a branch of a dendrimer, and flexible hydrophilic and/or hydrophobic linear polymers, which allows us to engineer its amphiphilicity in a form suitable

for self-assembly and molecular delivery [174]. The mono-disperse, highly branched molecular architecture of the dendron imparts a precise control over the peripheral functional groups and multivalency, as in dendrimers [175–178]. DCs have been reported to self-assemble into micelles at CMCs as low as 10^{-8} M, which are expected to be significantly lower than CMCs of linear-block copolymers with similar hydrophilic-lipophilic balances (HLBs, defined as HLB $= 20 \times M_h/M$, where M_h is the molecular mass of the hydrophilic part of the molecule, and M is the molecular mass of the whole molecule) [179–182]. The high HLB is important for a nanocarrier to achieve a large surface coverage by a hydrophilic layer, e.g., poly(ethylene glycol) (PEG), to maximize its in *vivo* circulation time while minimizing its non-specific interactions with biological components [183]. Although DC-based micelles seem to be ideally suited for nanocarriers, systematic and quantitative studies into the role of dendrons are still lacking. Here, we perform a systematic quantitative study of the dendron role during the self-assembly of supramolecular structures, by comparing the micelle morphology and CMCs when formed from DCs and linear polymers with the same HLBs.

7.2 Synthesis of PEGylated Dendron-Coils

The synthesis and experimental analyses of PEGylated DCs were performed by Prof. Seungpyo Hong's research group. The synthesized PEGylated DCs (PDCs) consist of three functional components: (1) poly(-caprolactone) (PCL), used as a hydrophobic, biodegradable core-forming block; (2) biodegradable 2,2-bis(hydroxyl-methyl)propionic acid generation 3 (G3) dendron with an acetylene core, chosen to mediate the core and shell-forming blocks through selective click chemistry and to achieve a localized high density of peripheral functional groups; and (3) bio-

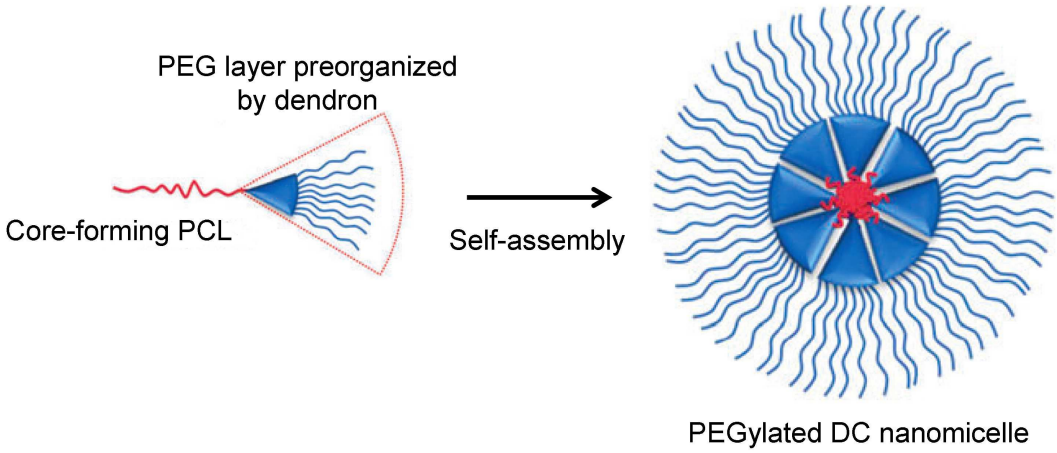

Figure 22. Schematic diagram of preparation of a nanomicelle from PEGylated DCs, synthesized through click chemistry between PCL and G3 dendron, followed by mPEG conjugation. The synthesis and experimental analyses were performed in Prof. Hong's laboratory.

compatible methoxy-terminated PEG (mPEG) forming the hydrophilic corona. The details of copolymer synthesis are described in [184].

Table I lists all the synthesized copolymers and their properties, including HLBs, HL ratios and CMCs. Two different molecular weights of PCL and mPEG (3.5 and 14 kDa for PCL; 2 and 5 kDa for mPEG) have been chosen to vary the HLB values of the resulting PDCs in a wide range. Similarly, the linear-block copolymer counterparts were prepared. All 8 amphiphilic copolymers (4 dendron-based and 4 linear, as listed in Table I) were successfully synthesized with low polydispersity indices, as confirmed using FT-IR, H-NMR, and GPC at each reaction step.

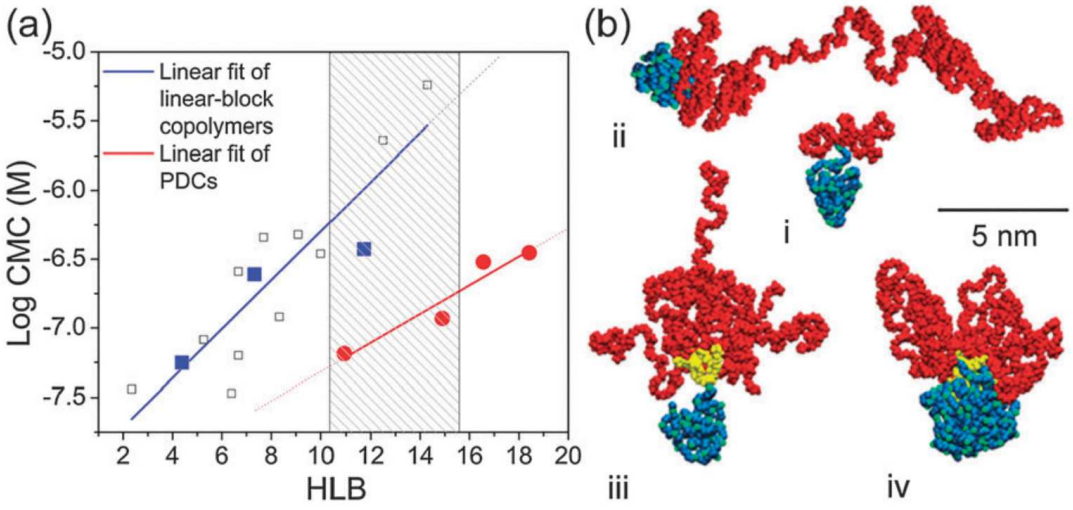

Figure 23. (a) Linear relationship between CMC and HLB for PDCs and linear-block copolymers. Additional data points for the linear-block copolymers (empty symbols) were acquired from the literature that used the same polymer blocks. Note that, at the same HLB $(10-15)$, the PDC self-assemblies maintain CMCs that are $1-2$ orders of magnitude lower than the linear counterparts, as highlighted in the shaded region. The data were obtained in Prof. Hong's laboratory. (b) MD simulations of (i) PCL3.5K-mPEG2K, (ii) PCL3.5K-mPEG16K, (iii) PCL3.5K-G3-mPEG2K, and (iv) PCL14K-G3-mPEG2K molecules after 5 ns in water (PCL: blue, G3-dendron: yellow, PEG: red). Water is not shown for clarity.

TABLE I

CRITICAL MICELLE CONCENTRATIONS (CMCS) OF THE AMPHIPHILIC COPOLYMERS WITH VARIOUS HYDROPHILIC-LIPOPHILIC BALANCES (HLBS)
[a] $HLB = 20M_H/(M_H + M_L)$, where M_H and M_L are molecular masses of the hydrophilic and lipophilic blocks, respectively. [b] Hydrophilic-lipophilic ratio.

Name	**HLB**[a]	**HL-ratio**[b]	**CMC, 10^{-7} M**
PCL3.5K-mPEG2K	7.27	36:64	2.40
PCL3.5K-mPEG5K	11.76	59:41	3.75
PCL14K-mPEG2K	2.50	13:87	–
PCL14K-mPEG5K	5.26	26:74	0.82
PCL3.5K-G3-mPEG2K	16.56	77:23	3.02
PCL3.5K-G3-mPEG5K	18.42	91:9	3.52
PCL14K-G3-mPEG2K	10.93	52:48	0.65
PCL14K-G3-mPEG5K	14.90	74:26	1.17

To directly assess the thermodynamic stability of the molecular assemblies, the CMC of each amphiphilic copolymer was measured [185]. A low CMC is particularly important for a nanocarrier in the bloodstream, due to an immediate, large dilution factor upon injection. Table 1 summarizes the measured CMCs, HLBs, and hydrophiliclipophilic (HL) ratios of the 8 copolymers. The CMCs of the linear-block copolymers are in good agreement with the previous reports [182, 186] and are comparable in magnitude to those of the PDCs, which have 24 fold higher HLBs.

Figure 23a shows a nearly linear correlation between CMC and HLB, observed for both linear and dendron-based copolymers. CMCs for linear-block copolymers composed of the same polymer blocks are included [187] to illustrate the large differences ($1 - 2$ orders of magnitude)

between CMC values observed for PDC micelles and linear-block copolymer micelles at similar HLBs. These data provide solid evidence that the pre-organized molecular architecture of the multiple PEGs and a single PCL mediated by a dendron facilitates the formation of remarkably stable PDC self-assemblies with large hydrophilic proportions. This is well illustrated on the PDC PCL3.5K-G3-mPEG5K (CMC of 3.5×10^{-7} M and HLB of 18.4) that is almost twice as hydrophilic as its linear counterpart PCL3.5K-mPEG5K (CMC of 3.8×10^{-7} M and HLB of 11.8). By measuring both dendron and linear copolymers at large HLBs (1618), the CMCs of the linear-block copolymers (10^{-5} M) [181, 182] are estimated to be up to two orders of magnitude larger than those of the PDCs (10^{-7} M).

7.3 Atomistic Modeling of PEGylated DCs and Their Assemblies

7.3.1 Computational Methods

We performed atomistic MD simulations of individual linear, PCL3.5K-mPEG2K and PCL3.5K-mPEG16K, and branched, PCL3.5K-G3-mPEG2K and PCL14K-G3-mPEG2K copolymers in water. Separately, we modeled micellar assemblies of hydrated PCL3.5K-mPEG2K, PCL3.5K-G3-mPEG2K, and PCL14K-G3-mPEGK copolymers with different aggregation numbers, N_{agg}. We used the NAMD package [30] and the CHARMM force field (CHARMM27, C35r revision for ethers, and general force field) [29, 32]. In all the simulations, a Langevin damping constant of $\gamma_{Lang} = 0.01$ ps^{-1} was used to achieve faster relaxation. Non-bonded interactions were calculated using the cut-off distance of $d = 12$ Å. Long-range electrostatic interactions were calculated by the PME method [31] and the MD integration time step was set to 2 fs.

The individual copolymer molecules were solvated and equilibrated for $\approx 5-7$ ns in TIP3P water, using the NPT ensemble, with periodic boundary conditions applied ($P = 1$ bar and $T = 300$ K). The obtained results are shown in Figure 23b. We also studied the conformations of individual copolymers fully equilibrated in water, using the same conditions. In the equilibration of PCL3.5K-mPEG2K, PCL3.5K-mPEG16K, PCL3.5K-G3-mPEG2K and PCL14K-G3-mPEG2K, a force of $F = 0.01$ kcal/mol/Å was applied to several atoms of the PEG chains, directing toward the hydrophobic PCL core. After ≈ 0.2 ns, the PEG chains were collapsed on the hydrophobic cores. Then, we stopped the force and equilibrated the monomers for another 10 ns.

7.3.2 Configurational Entropies of Linear and Branched Copolymers

We estimate the approximate entropic cost in the self-assembly of linear monomers, where it is assumed that PEG chains can be described as ideal chains [188]. An ideal chain of length L is comprised of n segments of statistical length l, so that $L = ln$. When placed in a good solvent (such as water), the ideal chain swells to maximize the number of polymer-fluid contacts. Configurations of the ideal chain can be characterized by a probability distribution function that depends on the chain end-to-end (e-t-e) distance. An ideal chain has a well-defined average e-t-e distance $\langle r \rangle = ln^{1/2}$, which is associated with minimum (configuration) free energy of the polymer.

When the ideal (PEG) chain becomes confined during the self-assembly process, its average e-t-e distance will increase and the free energy cost associated with this extension is purely entropic. Entropy of a freely jointed chain with a given e-t-e distance is proportional

to the logarithm of the number of chain configurations for that e-t-e distance. This, in turn, is proportional to the probability of the PEG having this e-t-e distance. The entropy difference between PEG chains in a given conformation with different e-t-e extensions is given by $\Delta S = S - S_1 = k_B b^2 (r_1^2 - r^2)$, where S and S_1 are configurational entropies associated with the e-t-e extensions r and r_1, k_B is the Boltzmann constant and $b^2 = 3/(2nl^2)$.

For PCL3.5K-mPEG16K, the PEG block has $n = 363$ repeating units (-CH_2CH_2O-), each of length $l \approx 0.368$ nm. In water, the average e-t-e distance of this polymer is $\langle r \rangle = ln^{1/2} \approx 7$ nm. If we assume that due to steric confinement the e-t-e distance of the chains in the micelle is extended by 50% from the above value of $\langle r \rangle$, the entropic cost for this extension is ≈ 1.11 kcal/mol $\approx 1.9\ k_BT$. Since every chain forming a micelle needs to pay this configurational entropy cost, the micelle formation is not favorable for polymers with long hydrophilic blocks, but in short chains attached to dendrons this entropic cost is absent. We can use the fact that the Gibbs free energy associated with the monomer self-assembly is given by $\Delta G = \Delta H - T\Delta S$, where ΔH is the related enthalpy change. We can immediately see that, for the same ΔH (hydrophobic binding in the core), long linear amphiphilic molecules tend to be less stable when self-assembled ($\Delta S > 0$) than branched dendron-based amphiphilic molecules ($\Delta S \approx 0$).

7.3.3 Modeling PDC Micelles

In the study of micellar assemblies, the monomers were initially spherically distributed by our codes and hydrated in cells containing $30,000 - 530,000$ atoms, with periodic boundary conditions applied. After short minimizations, the systems were heated to $T = 400$ K for fast reorganization, while the volume was kept constant. At the same time, the central force of

$F(\vec{r}) = k\vec{r}$ with $k = 1.0$ kcal/mol/Å was applied to several atoms along the PCL chains of all the copolymers, in order to accelerate aggregation of the micellar core. After 1 ns, the systems were cooled to $T = 300$ K, and equilibrated at $P = 1$ bar for $4 - 5$ ns. The obtained micelles are shown and discussed below.

7.3.4 Computational Results

The above MD simulations and analysis of configurational entropy clarify how dendron molecular architectures influence the micelle self-assembly. Figure 23b illustrates the structures of individual PCL3.5K-mPEG2K, PCL3.5K-mPEG16K, PCL3.5K-G3-mPEG2K, and PCL14K-G3-mPEG2K copolymers obtained after 5 ns of equilibration in water at $T = 300$ K. All the hydrated copolymers have a compact PCL block and relatively extended conformations of the PEG blocks. PCL3.5K-G3-mPEG2K shows a relatively stable conical shape, compared to PCL3.5K-mPEG16K with the identical HLB, since the dendron always keeps the PEG blocks close to the folded PCL block. The pre-organization of multiple PEG blocks attached to the surface of each PDC is favorable in the micelle self-assembly, giving a very small entropic cost in the self-assembly.

Moreover, PDCs with largely conical structures also have large enthalpic contributions to the coupling Gibbs free energy. In general, geometric constraints placed on amphiphilic molecules decrease their coupling Gibbs free energies, as necessary in their self-assembly [172, 189–191].

7.4 Characterization of PDC Nanomicelles

The size and morphology of the PDC and linear-block copolymer micelles were studied using transmission electron microscopy (TEM) and dynamic light scattering (DLS). Figure 24a shows

that all PDC and linear-block copolymer micelles were largely spherical in shape with narrow size distributions. The average diameters of all the self-assembled structures in the TEM and DLS measurements were smaller than 50 nm, except PCL14K-mPEG5K micelles that were $\approx$ 100 nm in diameter with a broader size distribution. The slight discrepancy in diameters between the TEM images and DLS measurements occurs because TEM visualizes the hydrophobic core of dried micelles with a minor contribution from the collapsed PEG shell [192]. Moreover, the polydisperse nature of polymers contributes to the variations in the measured diameters. Nonetheless, it is clear that PDC micelles form self-assembled structures with predominantly spherical shape and narrow size distribution, as compared to the linear polymer-based micelles, further supporting the superiority of PDCs in self-assembly. MD simulations show that the micelles formed from linear-block copolymers and PDCs have different surface coverage of the hydrophilic PEG layers. Figure 24b shows that the hydrophobic core is visible in the linear PCL3.5K-mPEG2K micelle, whereas it is fully covered by the PEG layer in the PCL3.5K-G3-mPEG2K PDC micelle. Interestingly, the core of the PCL14K-G3-mPEG2K PDC micelle is not completely covered by PEG, due to the long PCL chains, indicating that molecular weights of each polymer component in a PDC are also important to manipulate the surface coverage.

For the simulated micelles, we used the reported "magic" aggregation number (N_{agg}) of 14 to construct the PCL3.5K-G3- mPEG2K PDC micelle containing 112 PEG chains (Figure 24b-ii) [189], and 128 was used to construct the linear-block copolymer micelle to match the number of PEG chains (Figure 24b-i). Ten PCL14K-G3-mPEG2K molecules (80 PEGs) were used to match the size of the PCL3.5K-G3-mPEG2K PDC micelle (Figure 24b-iii). Using geometrical

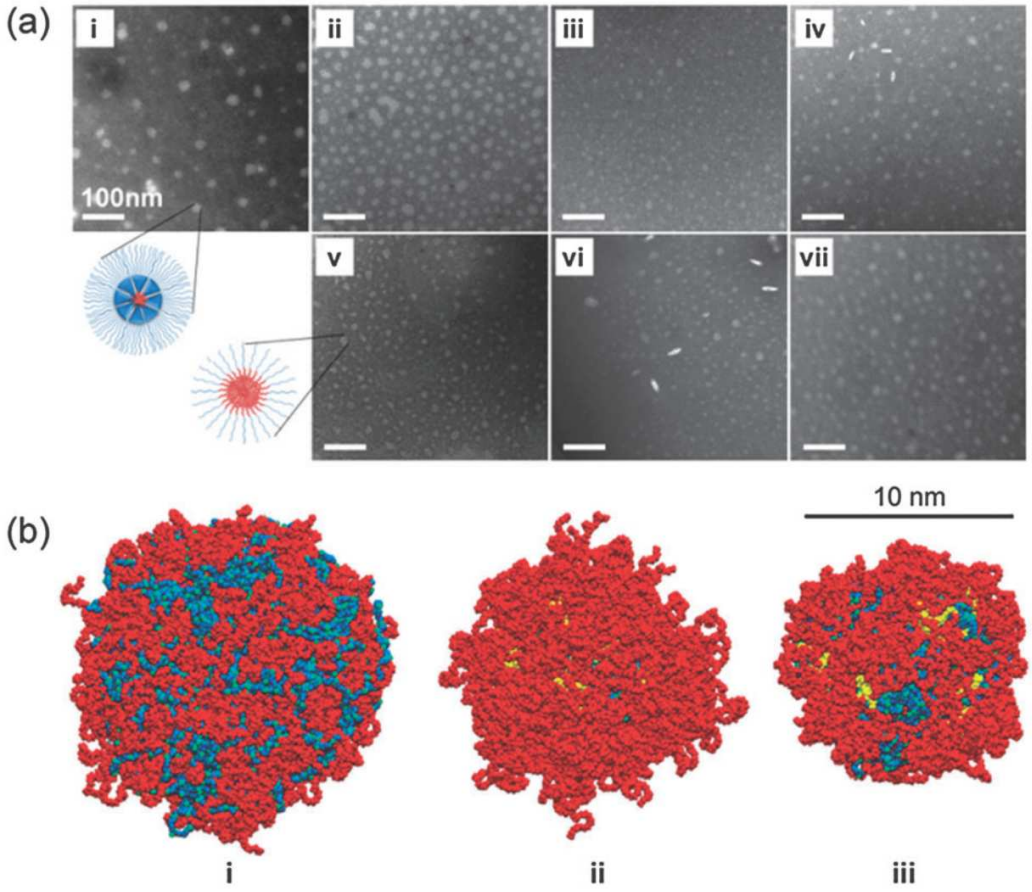

Figure 24. (a) TEM images of micelles self-assembled from PDCs obtained in Prof. Hong's laboratory: (i) PCL3.5K-G3-mPEG2K, (ii) PCL3.5K-G3-mPEG5K, (iii) PCL14K-G3-mPEG2K, (iv) PCL14K-G3-mPEG5K; and from the linear copolymers : (v) PCL3.5K-mPEG2K, (vi) PCL3.5K-mPEG5K, and (vii) PCL14K-mPEG5K. Scale bar = 100 nm. (b) MD simulations of micellar structures formed from (i) 128 PCL3.5K-mPEG2K, (ii) 14 PCL3.5K-G3-mPEG2K, and (iii) 10 PCL14K-G3-mPEG2K (PCL: blue, G3-dendron: yellow, PEG: red). Water is not shown.

relationships developed by Nagarajan [193], it is obvious that PDCs have a smaller N_{agg} than linear-block copolymers with the same length of linear polymer components, which is consistent with our MD results. Further, the high flexibility and number of PEG on the exterior of each PDC can promote the dense packing of the polymer chains, which can result in a CMC decrease. All the results presented here show that PDC-based micelles are more thermodynamically stable than those formed from linear block copolymers at the same HLBs.

7.5 Conclusion

In this chapter, we presented experimental and theoretical investigations of modular PDCs and their self-assembly into nanocarriers, performed in Prof. Hong's laboratory (experiments) and in Prof. Král's laboratory (theory). PDC-based micelles were compared with micelles formed from linear-block copolymer counterparts. The experimental observations made in Prof. Hong's laboratory and our supporting simulations and theoretical analysis clearly illustrate that the preorganized conical dendron architecture facilitates molecular assemblies with ultra low CMCs at high HLBs. In addition, DC-based micelles exhibit a significantly greater thermodynamic stability and surface coverage of hydrophilic layers than the linear polymer-based micelles. The highly stable supramolecular assemblies with homogeneous sizes and morphologies, highly hydrophilic PEG surfaces, and biocompatibility all prove that PDCs have great potential to provide a novel, versatile drug delivery platform.

CHAPTER 8

NANOMEDICINE II: POSITIVELY CHARGED DENDRON MICELLES DISPLAY NEGLIGIBLE CELLULAR INTERACTIONS

8.1 Introduction

In this chapter, we characterize PEGylated dendron-based copolymers (PDCs) with different end-group functionalities (-NH_2, -COOH, and -Ac) and their assemblies, which have the potential to become a new class of drug delivery platforms. The synthesis and experimental characterization of the studied systems were performed by the members of Prof. Seungpyo Hong's research group, while theoretical characterization was done by myself. The following contents are reproduced with permission from ACS Macro Lett., 2(1):77-81, 2013. Copyright (2012) American Chemical Society (see appendix).

Designing a nanocarrier that elicits controlled biological properties is critical to develop highly effective multifunctional drug delivery platforms. It has been demonstrated that the cellular interactions of such nanocarriers can be modulated through control over size, morphology, hydrophobicity, and surface charge [194–198]. Among the numerous investigated nanomaterials, dendrimers are unique macromolecules that have been successfully developed as a drug delivery platform. Their well-defined molecular architecture coupled with advantageous properties such as high branching degree, flexibility, controllable surface chemistry, and multivalency have all

been implemented, in one way or another, to enhance the efficacy of modern drug delivery platforms [175, 199–201].

Modulation of the surface charge of dendrimers has been used as major design criteria to control their cellular interactions and toxicity [**?**, 202–208]. In general, positively charged amine-terminated (-NH_2) dendrimers display a high level of nonspecific cellular interactions and toxicity because of electrostatic interactions with negatively charged cell membranes, whereas negative and neutral-charged dendrimers (carboxylated (-COOH) or acetylated (-Ac) surfaces) do not [203, 206, 207]. A number of other polycationic polymers, such as poly(L-lysine) (PLL), polyethylenimine (PEI), and diethylaminoethyl (DEAE)-dextran, have also shown nonspecific, spontaneous cellular interactions, which leads to high toxicity.

Recently, Prof. Hong's lab have developed methoxy-terminated (OMe) PEGylated dendron-based copolymers (PDC-OMe), which are triblock copolymers comprised of a polyester dendron (Generation 3 (G3), eight surface groups) and two types of linear polymers (polycaprolactone (PCL) and poly(ethylene glycol) (PEG)) [184]. At similar hydrophilic-lipophilic balances (HLBs), PDCs self-assembled into dendron micelles with high thermodynamic stability as measured by critical micelle concentrations (CMCs) that were 12 orders of magnitude lower than those of linearblock copolymer (LBC) counterparts. Additionally, molecular dynamics (MD) simulations revealed that the surface of the dendron-OMe micelle was almost completely covered by a dense PEG outer layer as opposed to the LBC micelles, which is expected to be beneficial by imparting stealth properties to the micelles in vivo [183, 209].

To understand the cellular interactions of dendron micelles at the molecular level, they engineered the chemical structure of each PDC to be suitable for self-assembly and to display various end-group functionalities on their surface. To that aim, they hypothesized that the surface functionality of the formed dendron micelles would largely determine these interactions, as in dendrimers and other nanocarriers. It was expected that amine-terminated dendron micelles would tend to interact spontaneously with cell membranes, while negative and neutral charged micelles would exhibit low levels of cellular interactions. To test this hypothesis, four structurally similar PDCs that varied only by surface functional group (-NH_2, -COOH, -Ac, and -OMe) were synthesized and self-assembled into dendron micelles. The cellular interaction of each micelle was evaluated using confocal microscopy and flow cytometry. Surprisingly, they observed that all four dendron micelles displayed similar cellular uptake and cell-associated fluorescence. This finding disproved our hypothesis and prompted a thorough investigation of the potential reasons for these observations, such as size, morphology, surface charge density, and end-group orientation of the dendron micelles.

8.2 Synthesis of PEGylated Dendron Copolymers

The synthesis and experimental analyses of all PEGylated DCs were performed by Prof. Hong's research group. The synthesis of PDC-NH_2, PDC-COOH, and PDC-Ac with low polydispersity indices (PDI < 1.2) was completed using a modified pre-existing protocol (Table II) [184]. The molecular weights of the hydrophobic PCL tail and the hydrophilic PEG chains were 3.5 and 2 kDa, respectively. Each surface-modified PDC was synthesized through a series of steps starting from BOC-protected PDC (PDC-BOC). Deprotection of PDC-BOC

TABLE II

MOLECULAR WEIGHT AND POLYDISPERSITY INDICES (PDIS) OF SYNTHESIZED PDCS

[a]Number-averaged molecular weight, M_n, estimated by ^{1}H NMR. Measured by GPC using the following. [b]Conventional calibration against polystyrene standards. [c]Eluted as multiple broad peaks due to column interaction [210].

samples	**theoretical** M_w	M_n^a	$M_{n,GPC}^b$	**PDI**
PDC-BOC	20,482	21,330	15,684	1.19
PDC-NH_2	19,690	18,077	–	NA
PDC-COOH	20,042	17,831	13,960	1.17
PDC-Ac	20,026	18,453	14,687	1.18
PDC-OMe	21,990	22,568	15,690	1.02

resulted in amine-terminated PDC (PDC-NH_2), and subsequent carboxylation using succinic anhydride or acetylation using acetic anhydride resulted in PDC-COOH and PDC-Ac, respectively. The dendron micelles with various surface groups were prepared by the self-assembly of the individual PDCs using the dialysis method and immediately used for further experiments.

8.3 Molecular Dynamics (MD) Simulations of PDCs and Micelles

8.3.1 Computational Methods

The computational modeling was performed by myself. Atomistic MD simulations of individual PDC-$(NH_2)_n$, PDC-$(COOH)_n$, and PDC-$(Ac)_n$ ($n = 4, 6, 8$ PEG copolymers per PDC) and dendron micelle assemblies ($n = 8$) were performed in water with aggregation numbers, N_{agg}, of 30. We used the NAMD package and the CHARMM force field (CHARMM27, C35r

revision for ethers, and general force field) [29, 30]. In all the simulations, a Langevin damping constant of $\gamma_{Lang} = 0.01\ ps^{-1}$ was used to achieve a faster relaxation. Nonbonded interactions were calculated using the cut-off distance of $d = 12$ Å. Long-range electrostatic interactions were calculated by the PME method and the MD integration time step was set to 2 fs. The individual PDCs were solvated and equilibrated for $\approx 10 - 12$ ns in TIP3P water, using the NPT ensemble (VMD) [43], with periodic boundary conditions applied ($P = 1$ bar and $T = 300$ K).

8.3.2 Modeling PDC Micelles

To model the dendron micelles used in this study, the monomers were initially spherically distributed by our codes and hydrated in cells containing 900,000-1,000,000 atoms, with periodic boundary conditions applied. After short minimizations, the systems were heated to $T = 400$ K for fast reorganization, while the volume was kept constant. At the same time, the central force of $F(\vec{r}) = k\vec{r}$ with $k = 1.0$ kcal/mol/Å was applied to several atoms along the PCL chains of all the copolymers, in order to accelerate aggregation of the micellar core. After 2 ns, the systems were cooled to $T = 300$ K, and equilibrated at $P = 1$ bar for $\approx 10 - 12$ ns, using NPT ensemble.

In order to observe in detail the hydrogen bond formation in the peripheral region of different micelles, we performed three separate simulations, each of them containing a single PEG chain which was terminated by one of the functional groups (-NH_3^+, -COO^-, or -Ac). Initially, the terminated PEG chain was hydrated in a cell containing 25,000-30,000 atoms and counter ions were added to neutralize the system. The MD simulation conditions were the same as described

above for the equilibration of the dendron micelles. We fixed a couple of atoms of the PEG chain (the other end of the PEG chain). After a short minimization, the systems were equilibrated for 12-15 ns. In the case of PEG-NH_3^+, we observed that the amine-hydrogen atoms form hydrogen bonds (cut-off distance 2.75 Å) with the oxygen atoms of the PEG chain. On the other hand, we have not observed such hydrogen bond formation for the other two systems (PEG-Ac and PEG-COO^-). In the case of PEG-NH_2 micelles, we expect intra and inter-hydrogen bonds formation.

8.4 Characterization of PDC Micelles

Figure 25A,B shows the particle size distribution, zeta potential, and CMC for dendron micelles of the four different types. The micelles predominantly exhibited diameters of $20 - 60$ nm, obtained by dynamic light scattering (DLS). Their particle sizes were stable for up to 21 days at room temperature in water and had the zeta potentials between 20 and 23 mV. The negative zeta potential value of the dendron-OMe micelles is likely attributed to the presence of partially negatively charged oxygen atoms near the termini of the PEG chain and is in agreement with a previous report employing methoxy-terminated polymer micelles [211]. The zeta potential of the dendron-Ac micelles was close to neutral because the proton in the amide end group does not appreciably dissociate at pH 5.6 (ddH_2O) due to its high pK_a value (typically > 15), maintaining a neutral zeta potential.

The thermodynamic stability of the PDCs was evaluated by measuring the CMC through monitoring their micelle formation with pyrene used as a fluorescent probe in water and in PBS [185]. As expected, the surface-modified PDCs displayed very low CMCs on the order of 10^{-7} M

at high hydrophilic-lipophilic balances (HLB) of ≈ 16.5. HLB is defined as $20 \times M_H/(M_H+M_L)$, where MH is the mass of the hydrophilic portion and ML is the mass of the lipophilic portion of an amphiphilic molecule [184, 212]. The CMCs of the PDCs measured in water and PBS appeared to be very similar under the conditions tested.

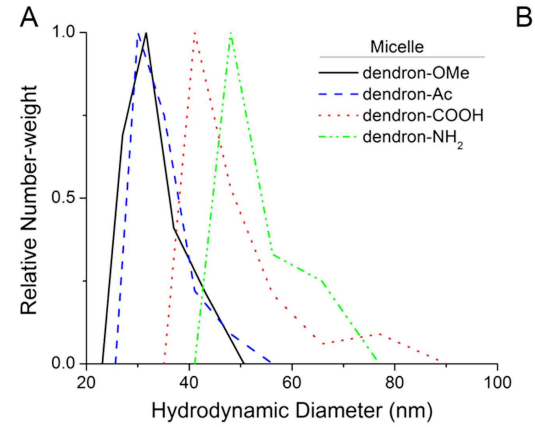

B

Micelle	ZP (mV)	CMC (10^{-7} M) Water	PBS
Dendron-NH_2	22.88 ± 2.84	9.58	9.31
Dendron-COOH	-19.06 ± 0.68	9.97	7.05
Dendron-Ac	2.39 ± 3.04	9.93	10.2
Dendron-OMe	-13.12 ± 5.96	11.1	8.72

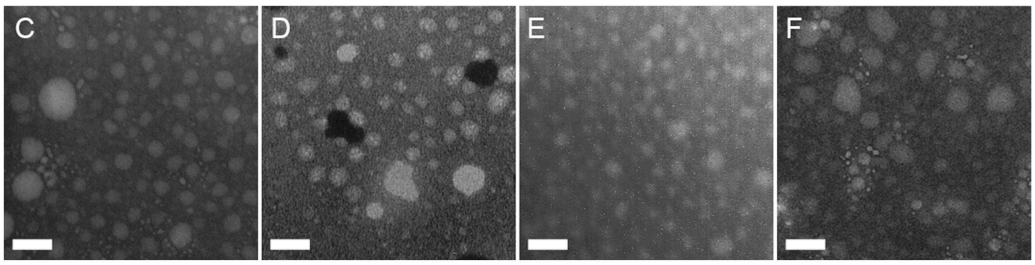

Figure 25. Characterization of surface-modified dendron micelles. (A) Hydrodynamic diameter measurements of dendron micelles using dynamic light scattering. (B) Zeta potential (ZP) values measured in ddH_2O (pH 5.6) and critical micelle concentration (CMC) of dendron micelles measured in ddH_2O and PBS (pH 7.4). Transmission electron micrographs of dendron micelles comprised of (C) PDC-NH_2, (D) PDC-COOH, (E) PDC-Ac, and (F) PDC-OMe. Scale bar: 50 nm.

Next, cellular interactions of the dendron micelles were studied. KB cells were treated with the dendron micelles at a polymer concentration of 4 μM (> 4-fold over CMC) to ensure that the structure of each micelle remained intact. Rhodamine-labeled, amine-terminated G4 polyamidoamine (PAMAM) dendrimer was prepared as described in previous studies [208, 213] and was used as a positive control in the cell studies at a concentration of 1μM. Unexpectedly, the dendron-NH_2 micelles did not exhibit a higher cellular uptake or cell-associated fluorescence than other surface-modified micelles. Instead, all surface-modified dendron micelles showed similar cellular uptake and low cell-associated fluorescence. The results from the dendron-NH_2 micelle are in contrast to our positive control achieved with PAMAM-NH_2 dendrimers, where we found that after 60 min of incubation a significant amount of the dendrimers was interacting with the cells. Our observations related to the dendron-NH_2 micelles are also in contrast with the results of previous reports, where the cellular interactions of G5 and G7 PAMAM dendrimers with NH_2, COOH, and Ac end-group modifications were tested [203,206]. PAMAM-NH_2 dendrimers strongly interacted with KB cells, while PAMAM-COOH and PAMAM-Ac dendrimers did not exhibit any significant cellular interactions after the same 60 min incubation time.

To understand this unexpected behavior of the dendron micelles, the influence of a number of parameters, such as size, morphology, PEG density, and orientation of the end-groups, which may play roles in determining the cellular interactions of the dendron micelles, have investigated. Note that nanocarrier-cell interactions are complex and potentially affected by a number of factors [198]. Transmission electron microscopy (TEM) was used to evaluate the effect of

size and morphology of the dendron micelles. Figure 25C-F shows electron micrographs of the dendron micelles after negative staining with 2% phosphotungstic acid. The size of the dendron micelles observed using TEM correlated with the results obtained using DLS. The micelles also had a spherical morphology, confirming our previous results (Figure 25) [184].

One possible reason for the absence of observable cellular interactions for the four types of dendron micelles could be their unusually dense PEG layer due to the dendritic architecture, as demonstrated in our previous study [184]. PEG is well-known to enhance the evasion of nanoparticles from detection by the reticuloendothelial system (RES) in vivo [214]. However, the presence of PEG does not always prevent micelles from nonspecifically interacting with cells [215, 216]. For amphiphilic polymers that comprise micelles with relatively low HLBs (typically lower than 3), a significant degree of nonspecific interactions with cell surfaces has been observed as opposed to those from higher HLB polymers (higher than 8 in general) [217].

In our dendron micelles, a PDC molecule theoretically accommodates eight PEG arms, resulting in an extraordinarily high PEG density on the PDC surface. Atomistic MD simulations revealed that the PEG density is significantly increased when the number of PEG chains per PDC is increased. This high PEG density, along with the almost complete surface coverage of the PEG outer layer [184], could likely result in the maximized nonfouling effect of PEG, which would, in turn, minimize nonspecific interactions of the dendron micelles in vitro regardless of the surface charge.

Another reason for the weak cellular interactions of the dendron micelles could be their significantly higher ratio of molecular weight to surface functional groups. Each PDC has an

approximate molecular weight of 18,000 Da and eight end-groups, resulting in a high molecular-weight-to-surface-functional-group ratio ($\approx$ 2250). G4 PAMAM dendrimers with an ethylene-diamine core on the other hand have a theoretical molecular weight of 14,215 Da and 64 end-groups, resulting in a 10-fold lower ratio ($\approx$ 222). One can thus expect that the end-group effect of the dendron micelles should be smaller than in dendrimers.

The effect of end-group orientation, which may contribute to the unobservable cellular interactions of the dendron-NH_2 micelles, have also investigated. The hydrogens of the amino-functional groups on the micelle surface could interact through hydrogen bonding with the oxygen atoms of the PEG backbone, in analogy to the coupling observed from other ions [218]. This would result in a decreased number of available positive charges to interact with the plasma membrane. This charge sequestration may be one potential mechanism by which the dendron-NH_2 micelles exhibit limited cellular interactions.

To confirm the intramolecular hydrogen bond formation and compare the overall micelle parameters, atomistic MD simulations (see computational part) were performed. Since our aim was to investigate the orientation of each of the employed end-groups, it was not necessary to match the size of the experimentally produced micelles. Dendron micelles were simulated using 30 PDCs arranged into spherical micelles. The simulated dendron micelle data are presented in Table III. The PCL core size of each micelle was similar ($\approx$ 8 nm), and the average thickness of the surface-modified PEG layers ranged between 10 and 11 nm. To observe the details of intramolecular hydrogen bond formation, three different simulations were carried out, each of them containing a single PEG chain that was terminated by one of the functional groups, -

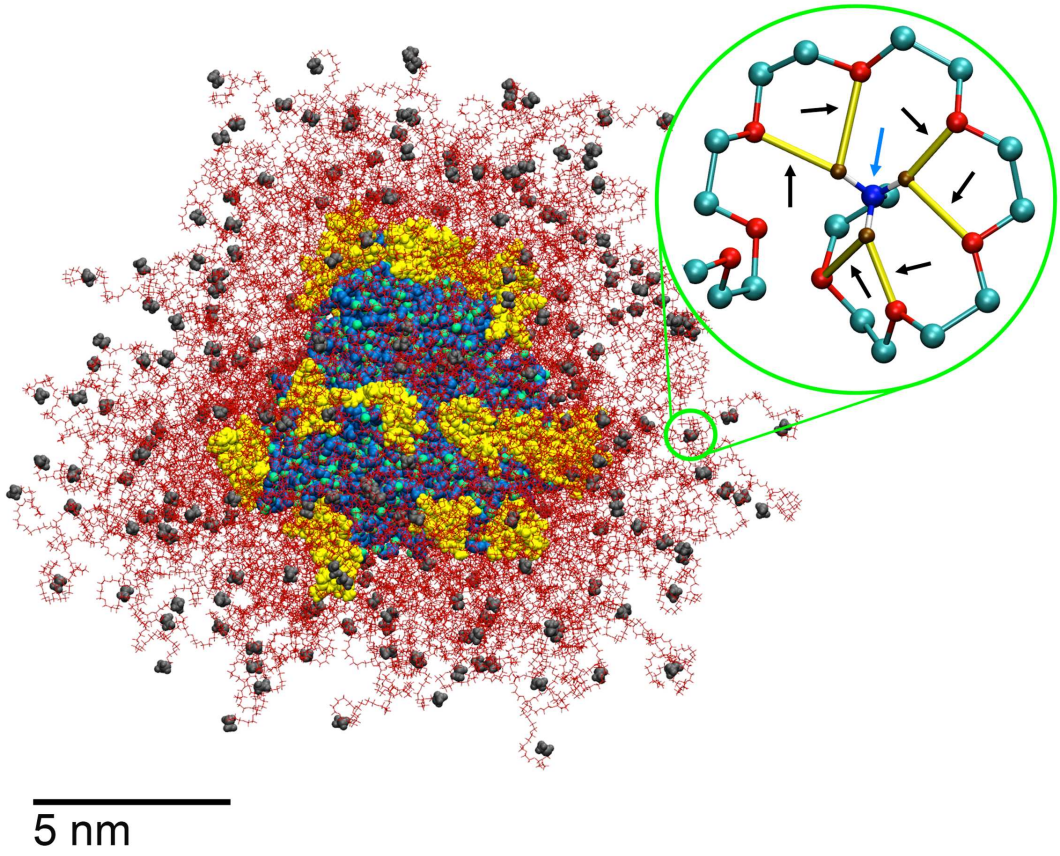

Figure 26. Atomistic molecular dynamics simulations of the dendron -NH_3^+ micelle in water. Black arrows indicate hydrogen bonding (yellow bonds) between hydrogens (gold balls) present on the terminal amine group (blue ball; identified by a blue arrow) with the oxygen atoms (red balls) present on the PEG chain. The hydrogen bond cutoff distance is 2.75 Å. We expect to observe intra- as well as intermolecular hydrogen bond formation within the micelle. Water is not shown for clarity.

TABLE III

DEPENDENCE OF THE TOTAL MICELLE DIAMETER (D_{TOTAL}), CORE DIAMETER (D_{CORE}) AND PEG CORONA DIAMETER (D_{PEG}) BASED ON AGGREGATION NUMBER (N_{AGG}) AND MONOMER TYPE. THESE VALUES ARE OBTAINED BY ANGULAR AVERAGING ($10 - 12$ NS) OF THE RADIAL EXTENSIONS OF THE PEG CHAINS WITH RESPECT TO THE MICELLE CENTER OF MASS.

Micelles	N_{agg} **nm**	d_{total} **nm**	d_{core} **nm**	d_{PEG} **(nm)**
dendron-COOH	30	19.21	7.99	11.22
dendron-NH_2	30	18.12	8.01	10.11
dendron-Ac	30	17.69	7074	9.95

NH_3^+, -Ac, or -COO^-. Hydrogen bonding between amine-hydrogens and oxygen atoms of the PEG chains was evaluated using a cutoff distance of 2.75 Å. From these simulations, we found that the PEG chain wraps around the terminal amine group through hydrogen bonding, as seen in Figure 26. No hydrogen bonding was observed between PEG and the other end-groups used in this study. Although we focused on one PEG chain in this simulation due to the long equilibrium time required, in principle, the hydrogen bond formation should be present throughout the whole micelle, both intra- and intermolecularly. This phenomenon is likely responsible for the decreased presentation of positive charges at the surface of the dendron-NH_2 micelles, contributing to the reduced cellular interactions.

8.5 Conclusion

In this chapter, we have presented experimental and theoretical investigations of surface-modified PDCs, with -NH_2, -COOH, -Ac, and -OMe surface groups and their self-assembly into

nanocarrier, performed in Prof. Hong's (experiments) and in Prof. Král's laboratory (theory). The lack of cellular interaction for the dendron -NH_2 micelles could be attributed to the dense PEG layers, the high molecular-weight-to- surface-group ratio (≈ 2250), and the orientation of end-groups (charge sequestration via hydrogen bond formation). Our results show that surface modification of the dendronized copolymers does not significantly alter the size or morphology of the formed micelles. These results provide a guideline for designing highly effective and targeted drug delivery micelles by overcoming, at times, the nonspecific interactions associated with PEGylated nanocarriers.

CHAPTER 9

DYNAMICS OF ION BINDING TO GRAPHENE NANOSTRUCTURES

9.1 Introduction

In this chapter, we model the dynamics of ion binding to graphene nanostructures by hybrid quantum/classical (QM/MM) simulations. We first perform scanned single-point DFT calculations of monovalent ions (Na^+, Li^+, Cl^-, F^-) at fixed distances above planar graphene-like H-passivated molecules of different shapes and sizes to obtain potential energy and charge transfer surfaces. We correlate these static results with our room-temperature QM/MM simulations of the ion-molecule systems, performed in both vacuum and water. Our simulations show that anions either are physisorbed onto the nanostructures or covalently bind at their selected regions, depending on the initial conditions, while cations only physisorb onto them. This research was conducted by myself and Mr. Dominic A. Esan. While both of us participated in all the aspects of research (designing the systems, carrying out the simulations, analyzing data), Dominic contributed more in preparing the manuscript. The following contents are reproduced with permission from J. Phys. Chem. C, 117(20):10750-10754, 2013. Copyright (2013) American Chemical Society (see appendix).

Since its recent isolation [67] graphene was the subject of many experimental [219, 220] and theoretical studies [221]. In particular, chemically functionalized graphene [222–225] has unique properties and potential applications [19, 226, 227]. Large attention was devoted to

graphene oxidation [228, 229], sulfonation [230], hydrogenation [231–234], fluorination [235–241], and chlorination [242–245]. Although, F^- binds covalently to graphene, Cl^- can either bind covalently or physisorb on it [242, 243]. Functionalized graphene nanostructures, such as nanoribbons [246] and porous graphene [146], have also been studied for their potential applications in electronics [151, 247, 248], molecular filtration [142], and nanofluidics [148, 149, 249].

However, it may be difficult to precisely functionalize graphene nanostructures since they are highly polarizable and they can have locally very different chemistries. Detailed information about their chemistry could be obtained in refined experiments. Recently, atomic force microscopy was used to map subtle differences in bond length and charge density connected with non-equivalent C-C bonds in polycyclic aromatic hydrocarbons [5]. Alternatively, advanced simulations can help guiding experiments aiming at precise functionalization of graphene nanostructures.

With this in mind, we model the dynamics of ion-nanostructure binding. We first use TeraChem [55] to perform scanned single-point DFT calculations of monovalent ions (Na^+, Li^+, Cl^-, F^-) at fixed distances above planar carbon-based H-passivated molecules of different shapes and sizes. At each point, we calculate the ion-nanostructure interaction energy and charge transfer (Mulliken charges considered). In principle, the scans can be performed at finite temperatures and averaged over a thermal ensemble to predict the binding dynamics of the components. We compare these results with separate quantum molecular dynamics simulations of the ion-molecule binding dynamics.

9.2 Computational Methods

The single-point energy calculations and molecular dynamical simulations were done for cations (Na^+, Li^+) at the B3LYP/3-21g* level, with dispersion corrections (DFT-D3) [250, 251], while for anions (F^-, Cl^-) they were done at the RHF/3-21g level, due to stability reasons. The use of B3LYP and the relatively small systems studied helps to minimize the self-interaction error in DFT [252]. We used the Conjugate Gradient (CG) method [253], the convergence criterion on the total energy of 10^{-6}, the X-matrix tolerance of 10^{-4}, the wavefunction convergence threshold of 3.0×10^{-5}, and the dispersion corrections [250, 251]. Our test calculations of the systems with other DFT methods (ωPBE, ωB97, ωB97x, and camB3LYP) gave similar results.

In the MD simulations (T = 100 and 300 K), we used the Langevin dynamics with the damping coefficient of $\gamma_{Lang} = 1$ ps^{-1}, and the time step of 1 fs (no periodic boundary conditions). Given the large power of TeraChem, we can scan the structures at relatively large pixel density of 0.5 Å (0.25 Å for the edge passage), giving in each scan a picture with ≈ 700 pixels.

9.3 Results and Discussion

9.3.1 Coronene ($C_{24}H_{12}$)

In Figure 27, we present the potential energy (top) and ion charge (middle) scans obtained for coronene. The scans were performed at the height of $h = 2$ Å for F^- (left) and $h = 2.5$ Å for Na^+ (right) above the optimized coronene (Figure 27c and f), using the RHF/3-21g and B3LYP/3-21g* levels of theory, respectively.

Figure 27a reveals that the potential energy surface for F^- has a pronounced C_6 symmetry. The coupling energy is large between the H atoms of neighboring C rings at the zigzag edges

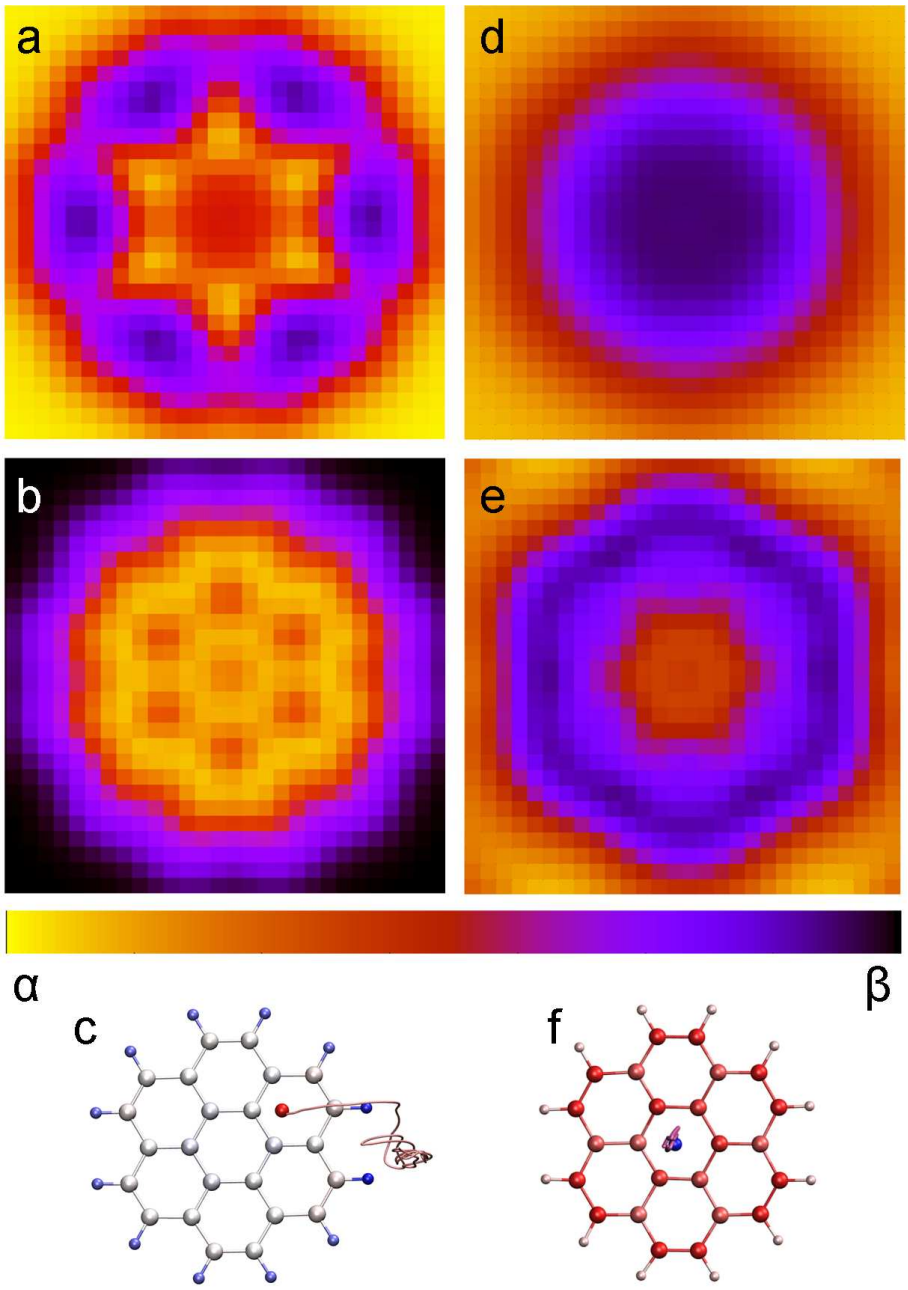

Figure 27. Scanning of F^- (left) and Na^+ (right) ions coupled to coronene, evaluated at $h = 2$ Å (for F^-) and 2.5 Å (for Na^+) above its surface. The potential energy surface for (a) F^- ($\alpha = -1009.60$ au and $\beta = -1009.64$ au) and (d) Na^+ ($\alpha = -1077.97$ au and $\beta = -1078.06$ au). The charge transfer surface for (b) F^- ($\alpha = -0.65$ and $\beta = -1$) and (e) Na^+ ($\alpha = 1$ and $\beta = 0.8$). The dynamics of (c) F^- released at $h = 4$ Å ($T = 100$ K) and (f) Na^+ released at $h = 3.5$ Å above the coronene flake ($T = 300$ K). The flakes are shown for the last simulation frame, where atoms are colored by charge. The pixel density is 0.5 Å. (a-f) have the same scale.

of coronene and it is small in its central region, giving a maximum energy difference is ≈ 1.6 eV (see scale). This can be explained by a large average positive charge on the H atoms of $q_H = -0.25e$ ($q_C = 0.14e$). The charge transfer distribution in Figure 27b shows that the transfer is large (≈ 0.35 e) above all the carbon atoms. From the binding energy profile, we expect that the area around the edge H atoms is the most likely target for F^- binding.

We compare these predictions with the simulated trajectories of F^- released at different heights above the coronene. When F^- is released at $h = 4$ Å, at the temperature of $T = 100$ K, it moves to the coronene periphery within 2.5 ps, as seem in Figure 27c. Over there it Coulombically couples (physisorption) to the polarized coronene and stays between two adjacent H atoms of the neighboring C rings, within 2.6 Å from each of them. When these simulations are repeated at $T = 300$ K, the ion moves along a slightly longer path and again couples between two the two H atoms. However, when F^- is released at $h < 3.5$ Å above the coronene center ($T = 300$ K), it binds covalently to one of the closest C atoms with a bond length of ($l \approx 1.35$ Å) . When the room-temperature simulations are performed at $h = 4$ Å in (nonpolarized) water (treated classically, TIP3), F^- is stabilized within 4 Å from the edge H atoms (B3LYP/6-31g).

We also performed the scans for cations. Figure 27d shows that Na^+ coupling is weak and of a radial symmetry in the negatively charged coronene center ($q_C = 0.12$ e, $q_H = -0.22$ e), indicating a tendency to physisorption. The charge transfer (Figure 27e) is larger in the peripheral region and of the C_6 symmetry. When Na^+ is released at $h = 3.5$ Å ($T = 300$ K), it diffuses around its central region at the average height of $h \approx 2.5$ Å, shown on the (1 ps)

trajectory in Figure 27f. In water at $T = 300$ K, Na^+ diffuses at $h = 3.5$ Å above the coronene center (B3LYP/6-31g).

9.3.2 Triangular Graphene Flakes

We also want to understand the binding dynamics of ions to other graphene nanostructures. Therefore, we model the ion binding to triangular H-passivated graphene flakes with zigzag and armchair edges of different sizes, as shown in Figure 28c and f, respectively (RHF/3-21g level). Figure 28a shows the potential energy of F^- evaluated at $h = 2$ Å above the zigzag-edge flake. It has a preference (4.9 eV) for the edge carbons. Figure 28b indicates that large charge transfers (≈ 0.5 e) occur along the edges. These expectations are confirmed in Figure 28c, showing that when F^- is released at $h = 4.8$ Å ($T = 300$ K), it covalently binds within ≈ 1 ps to one of the C atom at the (side) edge (sp^2 to sp^3 transition). However, when F^- is released at $h < 2$ Å above the flake, it binds to the nearest C atom. In experiments, [237–239] graphene fluorination was done with energetic ions (breaking of diatomic gas bonds by microwave or plasma) that prevent observation of different chemical functionalization at different graphene regions (bulk, edges).

Next, we present the results of F^- scanning at $h = 2$ Å above the armchair-edge triangular flake. Figure 28d indicates that the regions around the edge carbons (between the H atoms) have larger interaction energy (≈ 1.9 eV) but no preference to any particular region is observed. Figure 28e also reveals a large charge transfer ($\approx 35\%$) occurs above most of the C atoms. Therefore, when F^- is released at $h = 3.6$ Å ($T = 300$ K) above the flake, it binds covalently to C atoms away from the edge (see Figure 28f). This preference in F^- binding to internal carbons might be caused by the edge deformation upon binding [254].

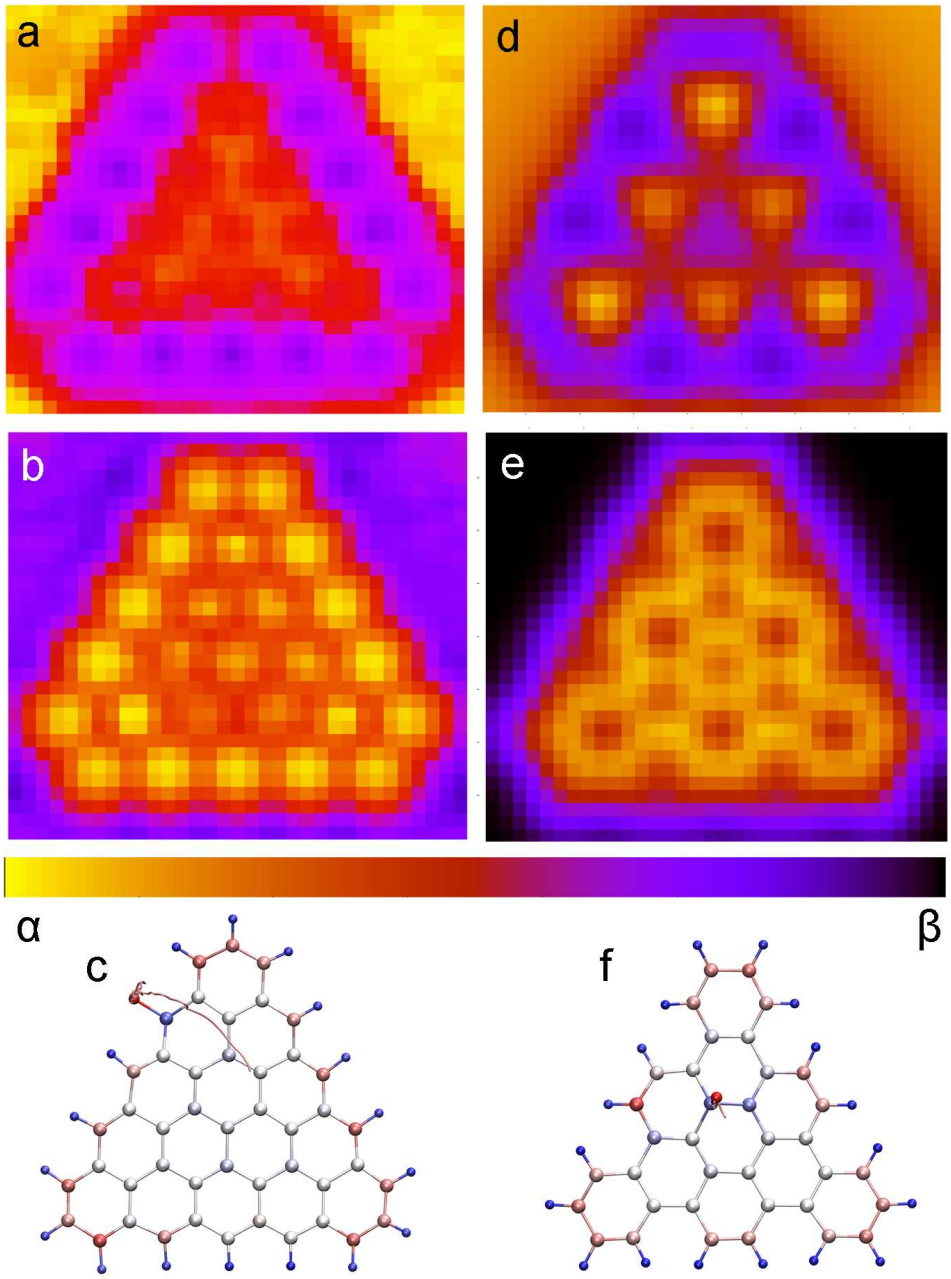

Figure 28. Sanning of F^- ion coupled to zigzag-edge (left) and armchair-edge (right) triangular graphene flakes, evaluated at $h = 2$ Å above their surfaces. The potential energy surface for (a) zigzag ($\alpha = -1841.36$ au and $\beta = -1841.54$ au) and (d) armchair ($\alpha = -1464.97$ au and $\beta = -1465.04$ au) flakes. The charge transfer surface for (b) zigzag ($\alpha = -0.45$ and $\beta = -0.95$) and (e) armchair ($\alpha = -0.65$ and $\beta = -1$) flakes. The structure and dynamics of (c) zigzag flake after 1 ps simulations with F^- released at $h = 4.8$ Å and (f) armchair flake in 0.4 ps simulations where F^- released at $h = 3.6$ Å. The covalent coupling formed is seen in both cases.

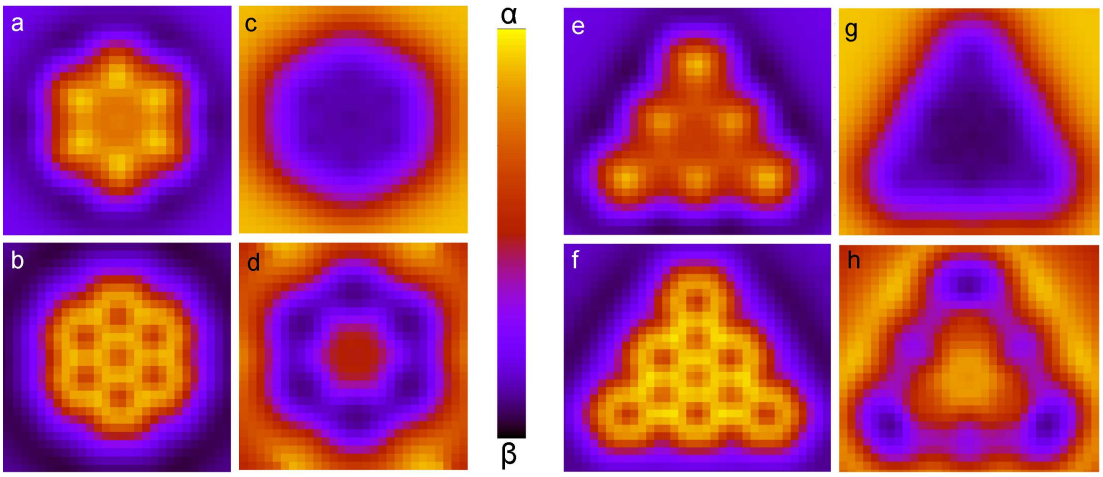

Figure 29. Scanning of Cl^- (left) and Li^+ (right) above coronene (left set), and armchair-edge triangular H-passivated graphene flake (right set) at $h = 2$ Å (Cl^-) and 2.5 Å (Li^+) above the surface of each molecule. Potential energy surface for (a) Cl^- ($\alpha = -1374.94$ au and $\beta = -1375.1$ au) and (c) Li^+ ($\alpha = -924.13$ au and $\beta = -924.22$ au). Charge distribution surface for (b) Cl^- ($\alpha = -0.3$ and $\beta = -1.0$) and (d) Li^+ ($\alpha = 1.0$ and $\beta = 0.78$). Potential energy surface for (e) Cl^- ($\alpha = -1833.364$ au and $\beta = -1833.54$ au) and (g) Li^+ ($\alpha = -1382.57$ au and $\beta = -1382.66$ au). Charge distribution surface for (f) Cl^- ($\alpha = -0.3$ and $\beta = -1.0$) and (d) Li^+ ($\alpha = 0.92$ and $\beta = 0.76$).

9.3.3 Simulation of Other Ions

We also studied the coupling of other ions to graphene flakes. The simulations show that Cl^- covalently binds to larger zigzag and armchair triangular flakes, due to their increased polarization. Graphene chlorination has also been done in experiments. [242, 244, 245] We found that the system in Figure 28c is the smallest flake where covalent Cl^- binding can be observed. This indicates that polarization plays a significant role in chlorination of small graphene structures. On the other hand, Li^+ and Na^+ bind to triangular flakes by physisorption, as in coronene (Figure 27d-f).

In Figure 29a-d (left set), we show the results of scanning Cl^- (left) and Li^+ (right) ions at the height of $h = 2$ (Cl^-) and 2.5 Å (Li^+) above the surface of coronene. In Figure 29e-h (right set), the same is done above the surface of the armchair triangular flake in Figure 29f. As shown in Figure 29a and e, the interaction energy of Cl^- is weak at the center of both the coronene and the triangular flake, but it is stronger along the edges. The charge transfer surfaces for Cl^- above these flakes also follow the same pattern, with the highest transfer of $\approx 70\%$ seen along the ring edges for both molecules (see Figure 28b and f). In contrast, Figure 29c and g show that Li^+ interacts more strongly with the central regions of both flakes, with a maximum energy difference between the edge and the center of ≈ 2.45 eV. In Figure 29d and h, we can see a charge transfer ($\approx 23\%$) of a striking structure along the ring edges of both molecules. Here, the single-point calculations were performed at the B3LYP/3-21g* level with dispersion corrections (DFT-D3).

9.3.4 Porous Graphene Flakes

It is of large interest to study the dynamics of ions and molecules around nanopores formed in graphene, due to their numerous applications in nanofluidics, molecular separation, molecular detection, and energy storage [142, 146, 148, 149, 249]. Here, we describe the coupling of ions to a rectangular H-passivated flake with a nanopore, shown in Figure 30c. Scanning of F^- at $h = 2$ Å and Na^+ at $h = 2.5$ Å above the optimized flake is done with the single-point energies calculated at the RHF/3-21g level.

Figure 30a presents the potential energy surface of F^- above the porous flake. Its minimum energy is at the zigzag-edge C atoms, about ≈ 4.9 eV deeper than in the pore area. The largest charge transfer also takes place over there (see Figure 30b). Although, this does not provide a direct evidence about the ion-flake covalent binding, we observe this binding of F^- to the zigzag edge of the regular flake (Figure 30f), when it is released at $h \approx 6$ Å and its trajectory is simulated for 1.5 ps at $T = 300$ K (B3LYP/6-31g level). When F^- is released at $h < 3$ Å above the regular flake, it covalently binds to any C atom. Its single-point energy scan with F^- at $h = 2$ Å gives similar results like in Figure 30a,b.

In Figure 30d, we also show the interaction energy of Na^+ to the porous flake. It has two large energy minima (≈ 3.3 eV) on the sides of the pore. Na^+ should physisorb to the porous flake as in the other structures. The charge transfer is relatively homogeneous across the whole structure, except of the large transfer at the pore region.

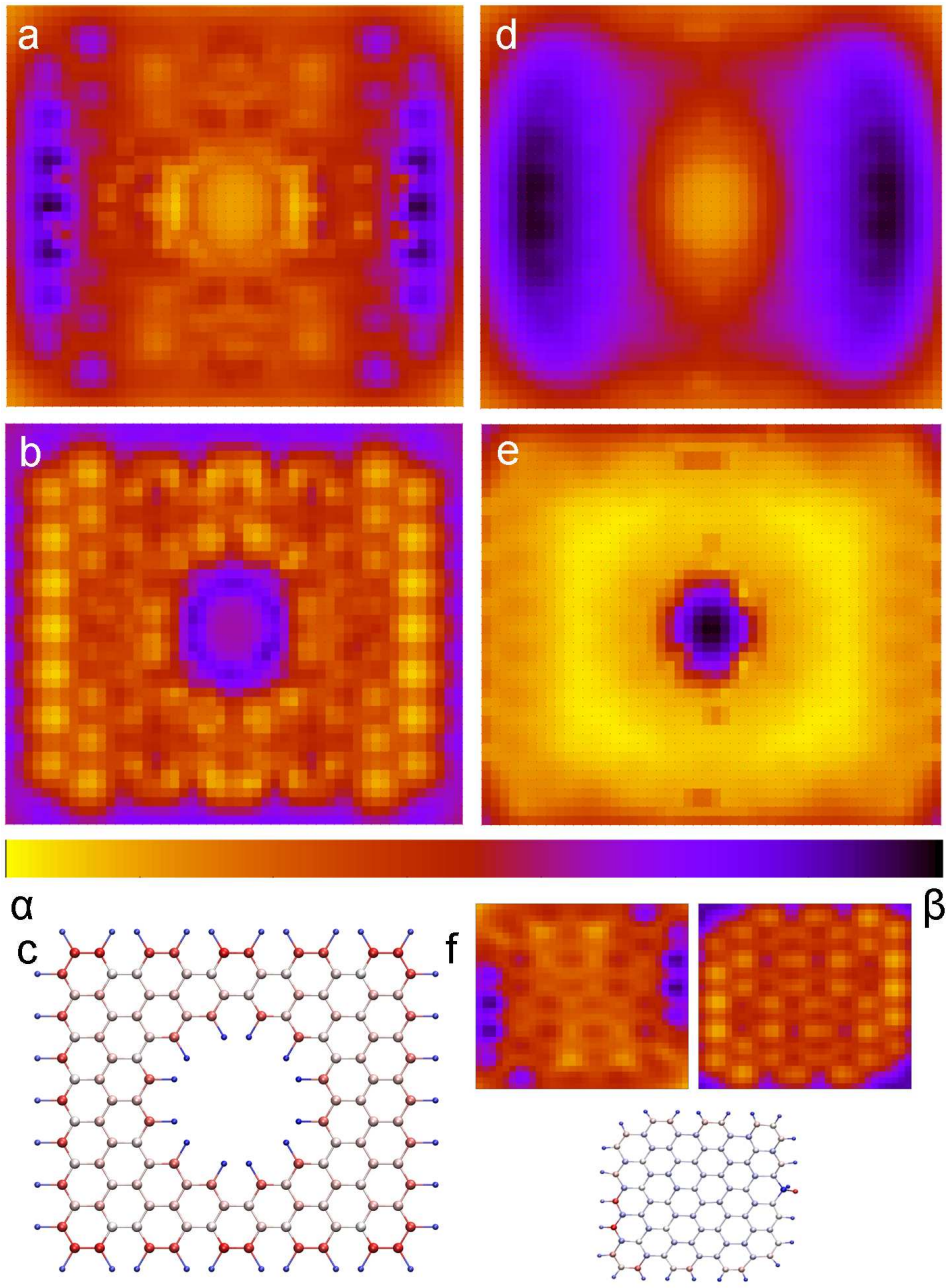

Figure 30. Scans of F^- (left) at $h = 2$ Å and Na^+ (right) at $h = 2.5$ Å above a rectangular H-passivated flake with a nanopore of the diameter ≈ 8.25 Å. Potential energy surface for (a) F^- ($\alpha = -4872.68$ au and $\beta = -4872.86$ au) and (d) Na^+ ($\alpha = -4934.58$ au and $\beta = -4934.70$ au). The charge transfer surface for (b) F^- ($\alpha = -0.45$ and $\beta = -1$) and (e) Na^+ ($\alpha = 1$ and $\beta = 0.2$). (c) The porous rectangular flake with atoms colored by charge. (f) Scanned calculations for a regular rectangular flake with F^-; (top left) potential energy surface ($\alpha = -3200.94$ au and $\beta = -3201.05$ au); (top right) charge transfer surface ($\alpha = -0.45$ and $\beta = -0.95$); (bottom) the rectangular flake with covalently bonded F^- at the edge, obtained after 1.5 ps quantum MD simulation at $T = 300$ K (F^- released at $h \approx 6$ Å above the center of the flake).

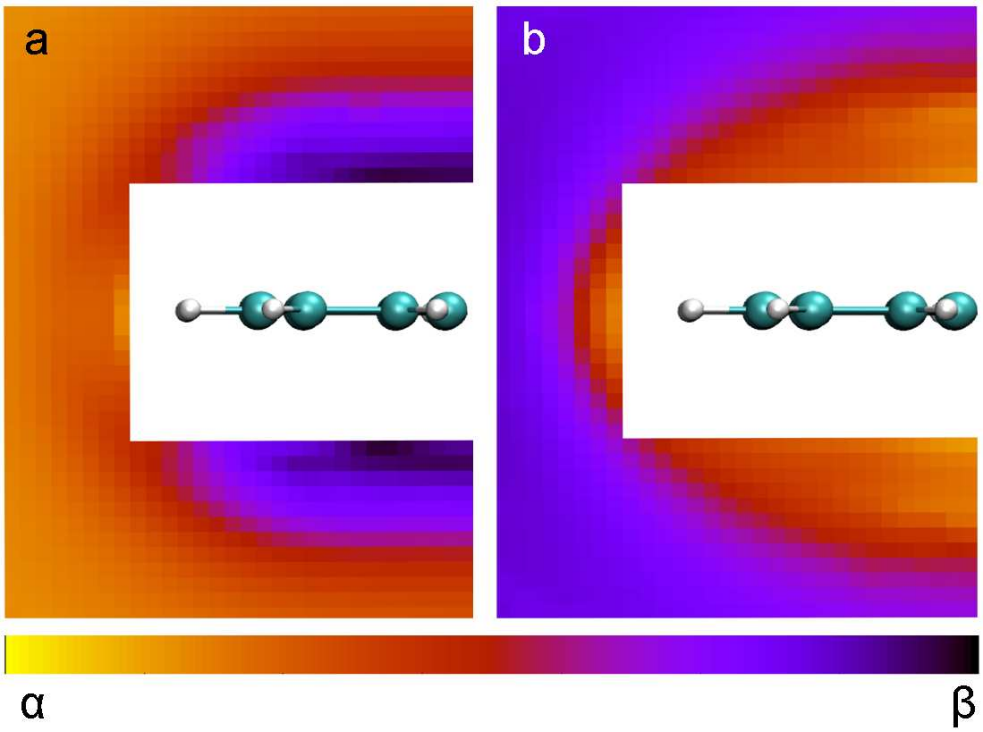

Figure 31. Scanning of Na^+ around the base of the zigzag-edge triangular H-passivated flake shown in Figure 28c (two basal layers of C rings are visualized from the structure). (a) The potential energy surface ($\alpha = -1915.39$ au and $\beta = -1915.47$ au) and (b) the charge transfer surface ($\alpha = 1.1$ and $\beta = 0.4$) are calculated in a U-shaped pixel arrangement around the flake (here, the pixel density is 0.25 Å).

9.3.5 Passage over the Nanostructure edge

Above, we study ion coupling to a H-passivated nanopore with a diameter of 8.25 Å. Since nanopores used in practical systems can be relatively large ($1-10$ nm), here we briefly examine the passage of ions over the central part of the zigzag edge in the triangular H-passivated flake shown in Figure 28c. We scan Na^+ around the flake at the position of the central H atom, within $1.6 < h < 5$ Å above the flake, at $d > 0.7$ Å in front of it. The single-point energy calculations are done at the RHF/3-21g level.

Figure 31a shows that the coupling energy between Na^+ and the flake. The energy is large at $h \approx 3$ Å above (below) the flake, but rather small in front of it. We calculate the energy barrier for Na^+ to move from the top to the bottom of the flake (around the U-shape window in Figure 31), between a point located at $h = 2$ Å above the flake (≈ 7.5 Å from the left edge of Figure 31) and a point located $d \approx 1.45$ Å in front of the H atoms within the plane of the flake. Since the barrier is $E_b \approx 1.24$ eV, the ion practically can not overcome this barrier at $T = 300$ K. Figure 31b also reveals that ≈ 0.3 e is passed to Na^+ close to the flake, as in coronene (Figure 27e), while at larger distances the charge transfer is fractional (limited validity).

9.4 Conclusion

In this chapter, we have studied the binding dynamics of monovalent ions to graphene-like H-passivated flakes. Our scanned ab initio calculations have revealed complex patterns in the potential energy and charge transfer surfaces of ions coupled to hexagonal, triangular, and porous graphene-based flakes. The scanned data correlate well with our time-dependent room temperature quantum molecular dynamics simulations of the ion attachment to the graphene

flakes. These studies open new avenues into large-scale exploration of nanoscale systems by first-principle methods.

CHAPTER 10

SELF-ASSEMBLY OF LARGE CARBON-RICH STRUCTURES IN INTERSTELLAR MEDIUM

10.1 Introduction

In this chapter, we use reactive MD simulations to describe the nucleation of long chains, large clusters, and complex cage structures in carbon and hydrogen rich interstellar gas phases. We study how temperature, particle density, presence of hydrogen, and carbon inflow affect the nucleation of molecular moieties with different characteristics. We derive analytic formulae for the formation times of the observed structures. We also determine the probability distributions of the sizes of carbon clusters at different temperatures. This research was conducted by myself.

Carbon-based chemistry of the interstellar medium (ISM) is now an established discipline. Presence of large variety of organic molecules such as nitriles, aldehydes, alcohols, acids, ethers, ketones, amines, amides and sugar, as well as many long-chain hydrocarbon compounds in the dense interstellar medium have been confirmed by infrared, radio, millimeter, and submillimeter spectroscopic measurement [255–260]. Detection of ring species, including aromatic rings, raises the possibility that biologically significant ring molecules may exist in the ISM. Between 10%-30% of the interstellar carbon budget is thought to reside in polycyclic aromatic hydrocarbons (PAHs) [261].

The presence and chemistry of complex molecules, and their spectral properties, are therefore useful probes of the environments in which they reside and provide a fairly faithful history of molecular clouds. IR emission lines (in the range of 3-14 μm) have been assigned to C-C and C-H vibration bands of a broad class of polycyclic aromatic hydrocarbons (PAHs) [259,261–266]. The simplest PAH, naphthalene ($C_{10}H_8$) has been found in carbonaceous chondrites [267], suggesting extraterrestrial origin. Although no specific PAH molecule has yet been unambiguously identified in space, the infrared emission bands have been observed towards nearly all astronomical objects, from highly ionized HII regions to ultraluminous infrared galaxies. Moreover, the simplest PAH, naphthalene ($C_{10}H_8$) has been already found in carbonaceous chondrites [267], suggesting its extraterrestrial origin.

The emission features at 7.0, 8.5, 17.4 and 18.9 μm, present in the spectra of Tc1, NGC 7023 and NGC 2023 planetary and reflection nebulae, have been conclusively associated with the vibrational lines of regular carbon cages (C_{60} and C_{70}) [268, 269]. Moreover, a large class of unsolved mysteries in astronomy, such as diffuse interstellar bands (DIB) [270], extended red emission (ERE) [271], and the 2,175 Å "bump" [272] trace their origins to large carbon and/or carbonaceous molecules. Single and multi-layer graphene have strong plasmon excitation bumps in the vicinity of the 2,175 Å feature [273]. However, more work in needed to establish their potential connection in astrophysical conditions. These challenges can not be solved without a strong theoretical input. Development of a comprehensive and detailed theoretical models for the origin and evolution of complex organic molecules such as PAHs, fullerenes, and

other ordered carbon structures may be crucially important for understanding of the role that prebiotic molecules played on early Earth.

To our knowledge, there are no available dynamical simulations of formation of molecules with aromatic rings at astrophysically-relevant conditions. However, it is not even clear under which conditions carbon structures are formed in ISM. Orderly growth of carbon structures (pentagon and hexagon rings, ring-stacks, ring fusion) from precursor C_2 molecules necessitates conditions close to chemical equilibrium. Under such conditions no significant curvatures form leading to cage-like structures. Fast inflow of carbon material is needed to form curved carbon clusters and fullerenes. In the laboratory, fullerenes are created with a remarkable efficiency (≈ 40 % in a condensing carbon arc) under conditions which are far from chemical equilibrium.

Most models for formation of larger aromatic carbon chains, rings, and cages in ISM work close to chemical equilibrium. For example, naphthalene ($C_{10}H_8$) can be formed via a barrierless reaction of phenyl radical (C_6H_5) and vinylacetylene (C_4H_4) [274], and C_{60} through a conversion of PAHs into graphene [275]. The latter top-down hypothesis relies on successive de-hydrogenation of PAHs, and formation of defects (pentagons) in graphene sheets for the synthesis of C_{60} in interstellar space. There are a number of issues here: the circumstellar environment of Tc1 planetary nebula is distinctly hydrogen poor; graphene is only synthesized in the laboratory and is not believed to naturally exist, and the processes for formation of laboratory carbon cages is far from equilibrium.

Interstellar gases are often present at very low densities for extended periods of time (equilibrium). Therefore, it is useful to understand the thermodynamics of these systems. At very

low density, carbon atoms behave like a monoatomic ideal gas with almost no clusters present in it. These atoms have a very large configurational space and entropy, which overcomes the binding enthalpy and destroys all the clusters ($G = H - TS$); atoms bound in clusters contribute by a much smaller entropy. As we increase the carbon density, small clusters are formed, since the entropic gain of atoms released from such clusters is smaller. Therefore, we can observe gradual formation of larger and larger clusters (dimers, trimers, etc.). Eventually, solid (liquid) and gas (of different clusters) phases coexist.

It would be hard to simulate ultra-low density systems. These systems may potentially be studied analytically by equilibrium thermodynamics methods. In this work, we study cluster formation in higher density carbon-based systems as they approach equilibrium. We use reactive molecular dynamics (MD) simulations to model the nucleation of carbon clusters, starting from randomly distributed elementary carbon and hydrogen atoms in a periodic box. We study how chains, rings, and cages of different sizes and moieties form in regimes relevant to astrophysics (cold temperatures and low densities), which are several orders of magnitude more diluted than those considered under laboratory conditions [276, 277]. Since the simulations of cluster nucleations under such conditions take a long time, we use an approximate description of the chemical bonds. Moreover, we propose simple analytical fit formulae for the structure formation times.

10.2 Computational Method

To simulate nucleation of carbon clusters in extraterrestrial space face, we need to solve several major issues. Since the systems are large, we cannot reasonably investigate them by first

principle molecular dynamics methods, but we can use semiclassical reactive MD simulations. These necessitate the knowledge of reactive force fields characterized by appropriate potential functions describing the change of hybridization of atoms over the time.

Here, we have applied the adaptive intermolecular reactive empirical bond-order (AIREBO) potential function proposed by Stuart [40], based on the Brenner bond-order potential [39]. This potential can be used for chemical reactions and intermolecular interactions in condensed-phase hydrocarbon systems such as liquids, graphite, and polymers. The potential function is given by

$$\begin{aligned} E_{Total} &= E_{REBO} + E_{LJ} + E_{tors}\,, \\ E_{REBO} &= V_{ij}^{R}(r_{ij}) + b_{ij} V_{ij}^{A}(r_{ij})\,, \end{aligned} \tag{10.1}$$

where V_{ij}^{R} and V_{ij}^{A} are repulsive and attractive pairwise potentials between atoms i and j, separated by r_{ij}, and b_{ij} is the bond-order term in a Tersoff-type potential [40]. The dispersion and intermolecular interaction (E_{LJ}) are modeled with a Lennard-Jones (LJ) 12-6 potential, with universal switching function and connectivity switch [40]. The torsional potential (E_{tors}) is proportional to bond weights that contribute to the dihedral angle [40].

Another problem of the reactive MD simulations is the timescale of the processes (mostly because the particle density is low). For example, the estimated time for fullerene formation through a laser irradiation or arc-discharge methods is 1 ms to several seconds. Therefore, simulating the whole process is computationally unrealistic. By increasing the density of carbon

atoms, we can compress the time. However, this compression enhances both the growth and dissociation of the formed clusters due to their collisions.

We model the self-assembly of clusters from C and/or H atom gases using atomistic reactive MD simulations with the AIREBO potential [40], as implemented in the LAMMPS package [278], The systems are modeled in the NVT ensemble at targeted temperature and time step is 0.5 fs. The Langevin damping method [42] is used to thermalize the systems and the damping co-efficient is 0.01 ps^{-1}. Periodic boundary conditions are applied. Visualization and analysis of the trajectories are done by VMD [43].

Simulations become progressively more computational expensive with increasing temperatures, as finer time steps are required- the scaling is linear with temperature. For instance, it took 24 hours to simulate $10,000$ C atoms at T=$3,000$ K for ≈ 1 ns simulation time on a 120-core machine with 2.6 GHz AMD Opteron processors. For the same reason higher temperature systems are simulated upto 50 ns.

10.3 Results and Discussion

In the actual simulations, 512 carbons atoms in the gas phase are placed in a cubic box with periodic boundary conditions. We change the density of carbon atoms (4.1×10^{-6} – 5.8×10^{-10} $Å^{-3}$) by varying the box size while keeping the number of atoms fixed. We investigate the cluster formation at different temperatures (3,000–300 K). We also simulate two systems at different temperatures where the ratio between carbon atoms and hydrogen atoms are 1 : 1 and 1 : 2, respectively (in a $500 \times 500 \times 500$ $Å^3$ box). Each MD simulation consists of two steps. First, the system energy is minimized for a short time (5 ps), the systems are heated to the

target temperature and equilibrated for up to 3 μs. Snapshots of carbon moieties formed at different times were taken for analysis and reproduction below.

10.3.1 Formation of chain and cage structures: dependence with gas temperature

Experimental evidence suggests that high temperatures are required to transform a flat structure to a curved moiety [279]. MD simulations were performed at $T = 3,000, 2,000, 1,000, 500,$ and 300 K. In a composite Figure 32, we give the time snapshots of carbon structure formation for a box size of $500 \times 500 \times 500$ Å^3, giving a carbon particle density of 4.1×10^{-6} Å^{-3}. At higher temperatures, as expected, diffusion and collision rates are faster and curvature forms at much earlier times. At top panel, planar clusters (a) form within t=10 ns, followed by fullerene type and large planar forms of five and six member rings after $t = 25$ ns (b), while fully formed fullerene structures ($C_{70} - C_{84}$) appear after $t = 50$ ns (c). Even at early times, defects (pentagons) are present in the moieties heralding the process of curvature formation. After $t = 90$ ns, nearly all structures are cages.

At $T = 2,000$ K, the temperature is still high enough to overcome transition barriers. Snapshots are given at $t = 25, 50,$ and 75 ns (d-f). The existence of five-member rings at $t = 25$ ns (d) is a prelude to cage-like structure formation. At $t = 50$ ns (e), curvature is dramatic and a fullerene-like structure begins to form. At $t = 75$ ns, cylindrical nano-structures due to merger of fullerene-type clusters form. At $T = 1,000$ K, even though defects are forming at short times, $t = 50$ ns (g), the tendency is to form chain-like structures, while cage-like structure begin to appear after $t = 100$ ns (h). At $t = 200$ ns (i), curvature is clearly evident, while regularity of the type present at higher temperatures, is lacking. At lower temperatures,

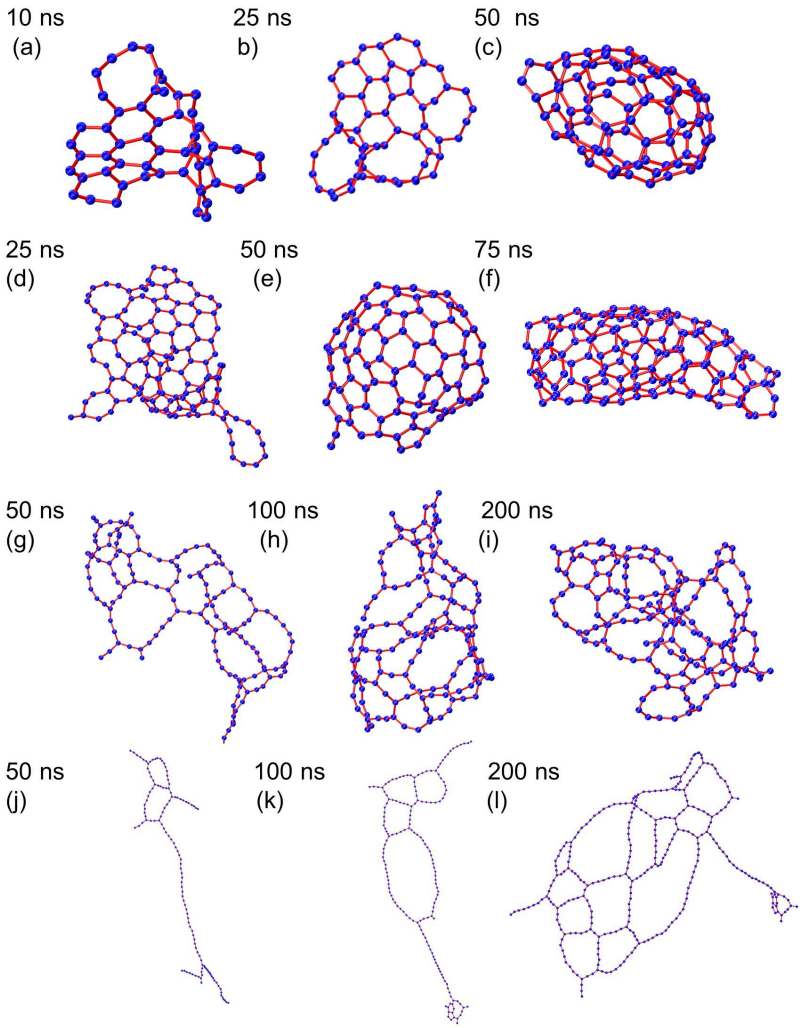

Figure 32. Self-assembly of carbon atoms at different temperatures (a–c at $T = 3,000$ K; d–e at $T = 2,000$ K; g–i at $T = 1,000$ K; j–l at $T = 500$K; most dominant structures are shown). 512 carbon atoms are placed in a cubic box ($500 \times 500 \times 500$ Å^3; atom density, $\rho = 4.1 \times 10^{-6}$ Å^{-3}). a) Formation of planar clusters (six member rings are well observed) within 10 ns. b) Fullerene type and big planar cluster with six and five member rings are observed after 25 ns. c) Almost all carbon atoms form fullerene type clusters ($C_{70} - C_{84}$) within 50 ns. d) Planar structures are formed within 25 ns. e) Formation of cage like structures with five and six member rings are observed after 50 ns. f) Cylindrical clusters, due to the merger of small fullerene type clusters, are found within 75 ns. g) Long chains emerge from short chains and eventually large member rings structures are observed (snapshot taken at 50 ns). h) Several large member rings form cage like structures (snapshot taken at 100 ns). i) Formation of five and six member rings are observed after 200 ns. j)Long chains molecules are observed within 50 ns. k) Large member rings emerge from long chains after 100 ns. l) Planar clusters, with big rings, are found after 200 ns.

$T = 500$ or 300 K, cage like formation takes very long times, if at all. Snapshots at $t = 50, 100,$ and 200 ns (j-l) in the lower panel illustrate that chain formation is readily accomplished with instances of several irregularly formed rings. At $t = 200$ ns (l), there's evidence for curvature formation, but rings with odd-number of atoms are quite irregular in shape.

While formation of structure at much lower temperatures and densities is hampered by the slowness in the diffusion and collision rates, it is still possible to glean valuable information under these conditions by investigating the pattern at higher temperatures and densities. We calculated the time taken to form small linear or branched chain, with a carbon atom number, ($n_C \approx 30$), at different temperatures. As shown in Figure 33, at 300 K, small chains form after $\approx$ 40 ns, whereas at 3,000 K, it took $\approx$ 3.5 ns to form. The formation time at 500 K, 1,000 K, 2,000 K, are 28.5 ns, 10.5 ns, 5.2, respectively. The analytic dependence is t(ns)= 23,153 $\mathrm{T}^{-1.10}$(K).

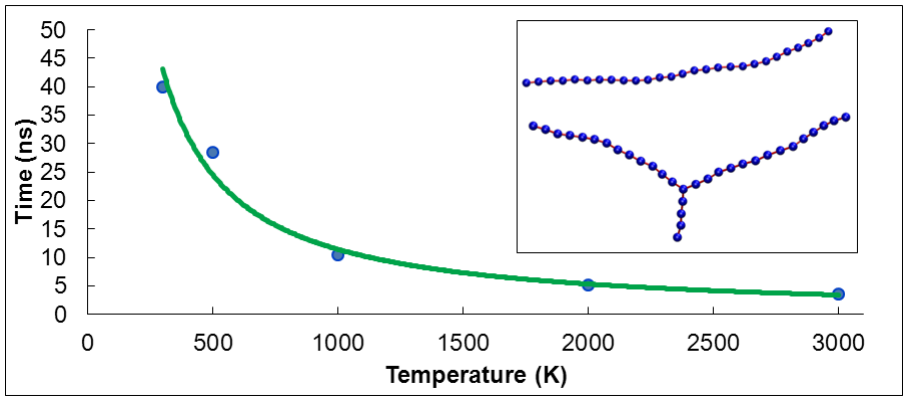

Figure 33. Self-assembly of carbon atoms to small linear or branched chains at different temperature. The analytic dependence is t(ns)= 23,153 $\mathrm{T}^{-1.10}$(K).

Next, we measured the time of formation of small graphene flakes at different temperatures. We observed graphene flakes after ≈ 9.7 ns at $3,000$ K, whereas at $1,750$ K, we noticed formation of graphene flakes after 18.4 ns. We did not observed graphene flakes forming at $T < 1,500$ K. This is likely due to existence barrier below $T < 1,750$ K. It is then possible to obtain a fit to the formation time vs. temperature. The analytical form is $t(ns) = 339,404\ \mathrm{T}^{-1.31}(\mathrm{K})$. This fit predicts that a graphene flake, assuming that the classical over the barrier can be penetrated, would form after $t(ns) \sim 193$ at $T = 300$ K.

10.3.2 Formation of chain and cage structures: dependence with gas density

Next, we study the effect of particle (carbon atom) density on the structure of carbon cages/clusters. Here, we simulated the clustering process with different carbon atom densities (4.1×10^{-6} Å^{-3} – 5.8×10^{-10} Å^{-3}) at $T = 3,000$ K. As shown in Figure 32a (carbon atom density, $\rho = 4.1 \times 10^{-6}$ Å^{-3}), planar cluster formation were observed within 10 ns and all carbon atoms formed fullerene type clusters after 50 ns (Figure 32c). However, when we decrease the the concentration of carbon atoms ($\rho = 5.1 \times 10^{-7}$ Å^{-3}), short chain molecules emerge only after 100 ns. After 450 ns, long chain molecules with cage like clusters were observed. Fullerene type clusters were observed after $1\mu s$. Interestingly, no graphene flakes formation were observed at $T = 3,000$ K. Graphene flakes formation were observed after 97 ns and 125 ns at $2,500$ K and $2,000$ K, respectively. No graphene flakes were observed at 300 K and 500 K after $\approx 3\mu s$. When the concentration is 5.8×10^{-10} Å^{-3}, we have only found very short carbon chain molecules (n < 10) after 450 ns; no planar and fullerene type clusters were observed.

10.3.3 Hydrogenation process

In order to investigate the influence of hydrogen atom addition on the structure of carbon cages/clusters, we simulate two systems where the ratio between carbon atoms and hydrogen atoms are $1:1$ and $1:2$, respectively. We also investigated the effect of concentration on the self-assembled structures by varying the atomic concentration. For each study, after a short minimization, we simulated the cluster formation at different temperatures ($3,000$ K, $2,000$ K, $1,000$ K, 500 K and 300 K). Here, we noticed the formation of alkene and other unsaturated carbon-hydrogen chain molecules along with small carbon clusters and hydrogen molecules. We observed that hydrogen atoms terminate the growth of big carbon clusters. At low temperature $T = 500$ K, small chains (terminated with hydrogen atoms) were predominantly found (Figure 34a). Planar clusters (Figure 34b), terminated by hydrogen atoms, were observed at $T = 1,000$ K. Fullerene type clusters were observed at high temperature $T = 2,000$ K (few hydrogen atoms were absorbed on the surface), as shown in Figure 34c. At low temperatures, both the C-H and C-C bonds formation are favorable, but at high temperatures C-H bonds formation is less favorable compared to C-C bonds due to high thermal fluctuation. Therefore, small hydrogen terminated carbon chains were observed at low temperatures and graphene to fullerene type clusters were formed at high temperatures.

10.3.4 Carbon inflow: non-equilibrium nucleation

While in a chemical steady-state condition, significant curvature of graphitic sheets, leading to spontaneous folding to form a cage structure, may not occur at certain low temperatures, inflow of carbon material could facilitate approach to additional equilibria to curved carbon

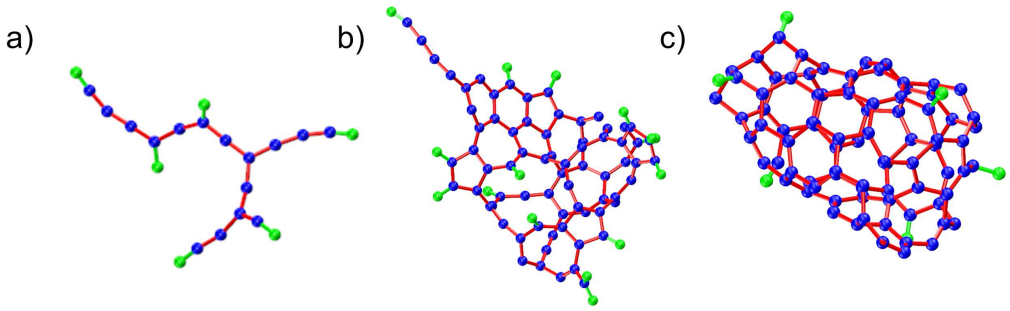

Figure 34. Formation of Carbon-hydrogen clusters (most dominant structures were shown, snapshots taken at 200 ns). 256 carbon atoms and 256 hydrogen atoms were placed in cubic box ($500 \times 500 \times 500$ Å^3). a) Short unsaturated chain and branched molecules, terminated with hydrogen atoms, were formed at $T = 500$ K. b) Planar clusters, terminated with hydrogen atoms, were observed at $T = 1,000$ K. c) At $T = 2,000$ K, fullerene like clusters, with some hydrogen atoms attached to surface, were found.

clusters and finally to fullerene formation. This situation is more resembling of astrophysical environments. Here, we investigate the nucleation process under such conditions. To this end, we simulate with 100 gaseous carbon atom in a 150 Å^3 box (atom density, $\rho = 2.96 \times 10^{-5}$ Å^{-3}) at 1,750 K (all other conditions are the same as describe above). After equilibrating for 10 ns, we save the coordinates of all atoms at the last frame and add another 20 carbon atoms into the box, keeping it box size fixed (total carbon atoms = 120; atom density, $\rho = 3.55 \times 10^{-5}$ Å^{-3}). After minimization, we simulate for another 10 ns equilibration at 1,750 K and save the coordinates of all atoms of the last frame and repeat the process one more time (total carbon atoms = 140; atom density, $\rho = 4.15 \times 10^{-5}$ Å^{-3}).

As shown in Figure 35a, we observe that planar cluster forms, with few six and five member rings, after 10 ns. Within 20 ns, formation of bend structure is observed with more six and

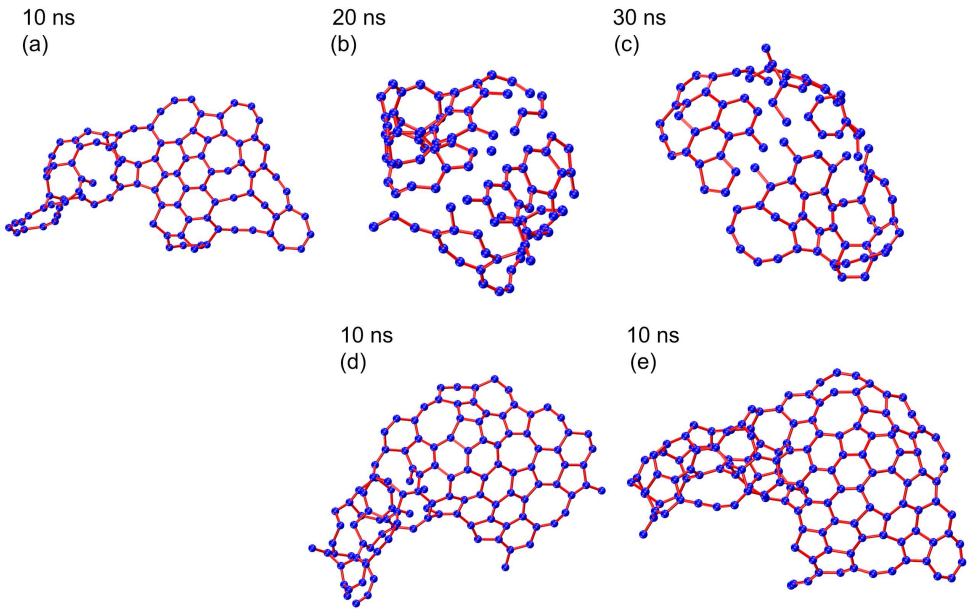

Figure 35. Carbon inflow at $T = 1,750$ K. 100 carbon atoms are placed in a cubic box ($150 \times 150 \times 150$ Å^3). a) Formation of planar cluster with few six and five member rings is observed; snapshot taken at 10 ns. b) Bend cluster, with of six and five member rings, is observed after 20 ns. c) More bend structure, with all five and six member rings, is formed after 30 ns (note that some C-C bonds are missing for b and c; this is due to the fact, some part of these structures are in other periodic boxes and VMD (visualization software) can not draw bonds in such situations). d)Formation of planar cluster after 10 ns, where 20 carbon atoms are added after 10 ns simulation of 100 carbon atoms(a). e)Formation of even bigger planar cluster after 10 ns, where another 20 carbon atoms are added after 10 ns simulation of 120 carbon atoms(d).

five member rings (Figure 35b) and after 30 ns, curved structures are observed where allmost all carbon atoms form six or five member rings (Figure 35c). When we add 20 carbon atoms to structure in Figure 35a and simulate for another 10 ns, we observed more planar structure compared to Figure 35b, as shown in Figure 35d. The added carbon atoms form bonds with edge carbon atoms of Figure 35a and tend to create six member rings. When we add another 20 carbon atoms to Figure 35d, we observe more planar structure (Figure 35e) compared to Figure 35c, as the added carbon atoms again form bonds with edge carbon atoms of Figure 35d and create more six member rings.

10.3.5 Probability Distribution of Cluster sizes

The carbon structures which form in simulations can have varying distributions according to atom size, moiety, ring size (pentagon, hexagon) and bond length, depending on the density and temperature of the gas. There can be large variations in different clusters which form. We have determined the probability distributions on structure size (C atom number) at different temperatures and densities. To this end, we simulated two systems with $4,100$ and $10,000$ carbon atoms (carbon density, $\rho = 4.0 \times 10^{-}6$ Å^{-3} same for both systems) in gas phase at T = $3,000$ K, $2,000$ K, $1,000$ K, and 500 K. At $T = 500$ K, the size distribution is obtained after 200 ns. Similarly, for $T = 1,000$, $T = 2,000$, and $T = 3,000$ K, the size distributions are obtained after 100ns, 50 ns, and 40ns, respectively. For a particular system, the total number of formed clusters are divided into bins with each bin containing 25 carbon atoms. Clusters, having less than 5 carbons atoms are ignored. Simulations are performed for two large systems containing $4,100$ and $10,000$ atoms. The different statistical distributions are modeled with

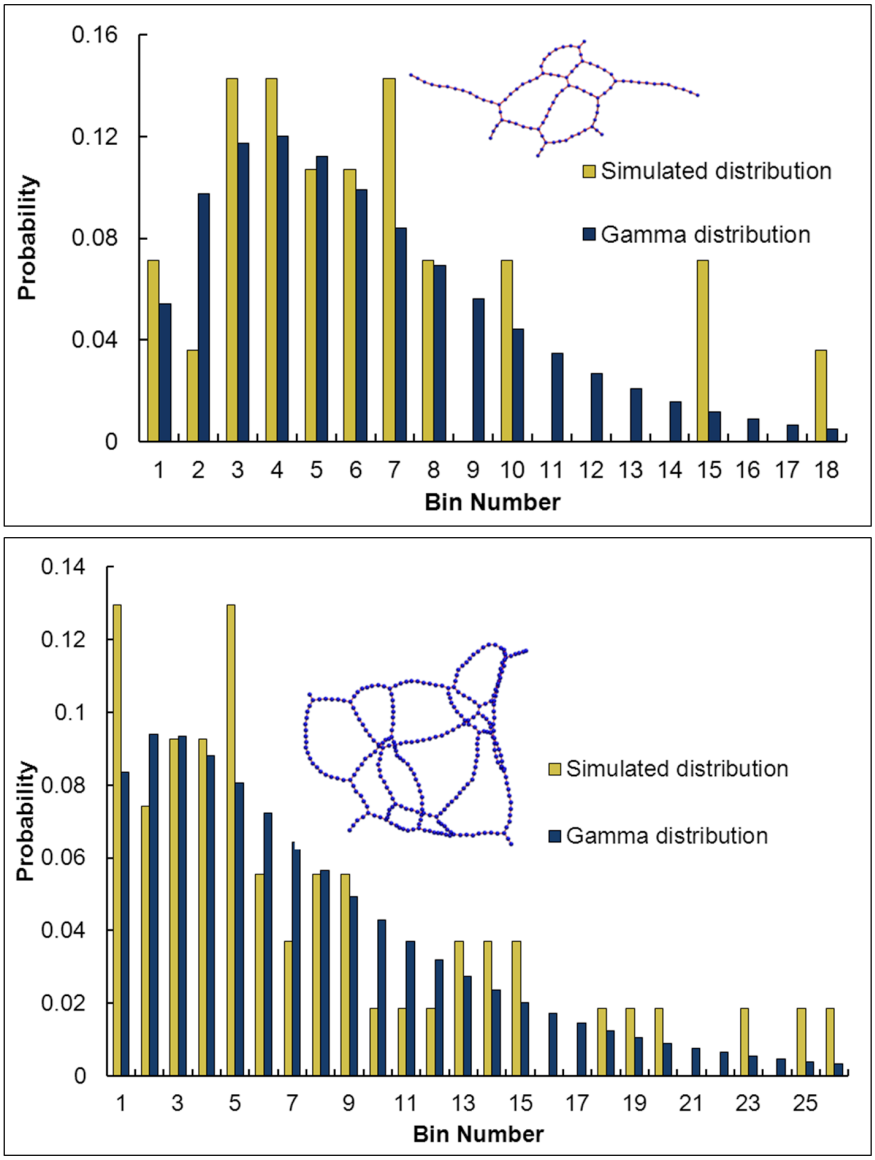

Figure 36. Probability distribuition of carbon clusters (based on atom numbers in each cluster). (top) Simulated and gamma (blue; $\alpha = 2.3902$ and $\theta = 2.6447$) probability distributions of formed cluster sizes with $4,100$ carbon atoms (atom density, $\rho = 4.0 \times 10^{-}6$ Å^{-3}) at 500 K. (bottom) Simulated and gamma (blue; $\alpha = 1.4441$ and $\theta = 5.3347$) probability distributions of cluster sizes with $10,000$ carbon atoms (atom density, $\rho = 4.0 \times 10^{-}6$ Å^{-3}). The bin size is 25 carbon atoms. The snapshots are taken at 200 ns.

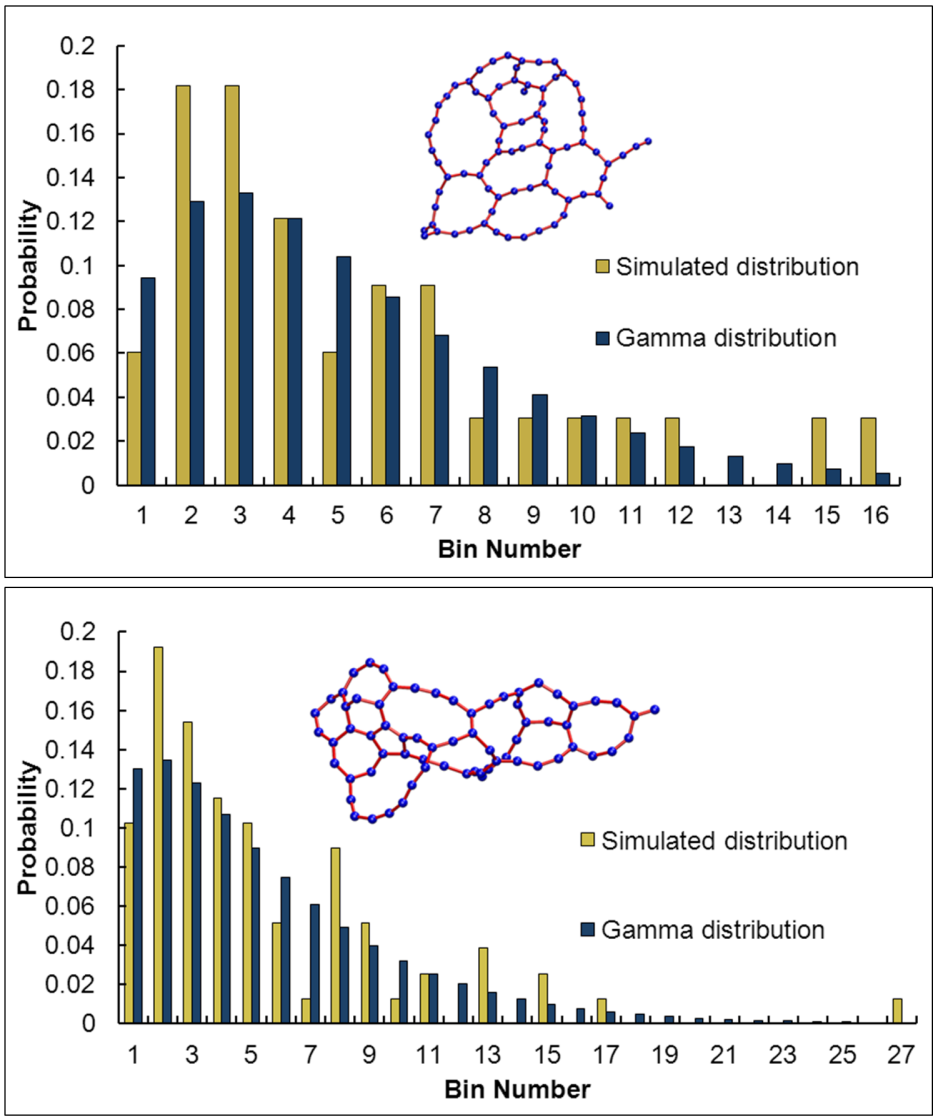

Figure 37. Probability distribuition of carbon clusters (based on atom numbers in each cluster). (top) Simulated and gamma (blue; $\alpha = 2.0007$ and $\theta = 2.6959$) probability distributions of formed cluster sizes with $4,100$ carbon atoms (atom density, $\rho = 4.0 \times 10^{-}6$ Å^{-3}) at $1,000$ K. (bottom) Simulated and gamma (blue; $\alpha = 1.4342$ and $\theta = 3.7367$) probability distributions of cluster sizes, with $10,000$ carbon atoms (atom density, $\rho = 4.0 \times 10^{-}6$ Å^{-3}) at $1,000$ K. The bin size is 25 carbon atoms. Snapshot taken at 100 ns.

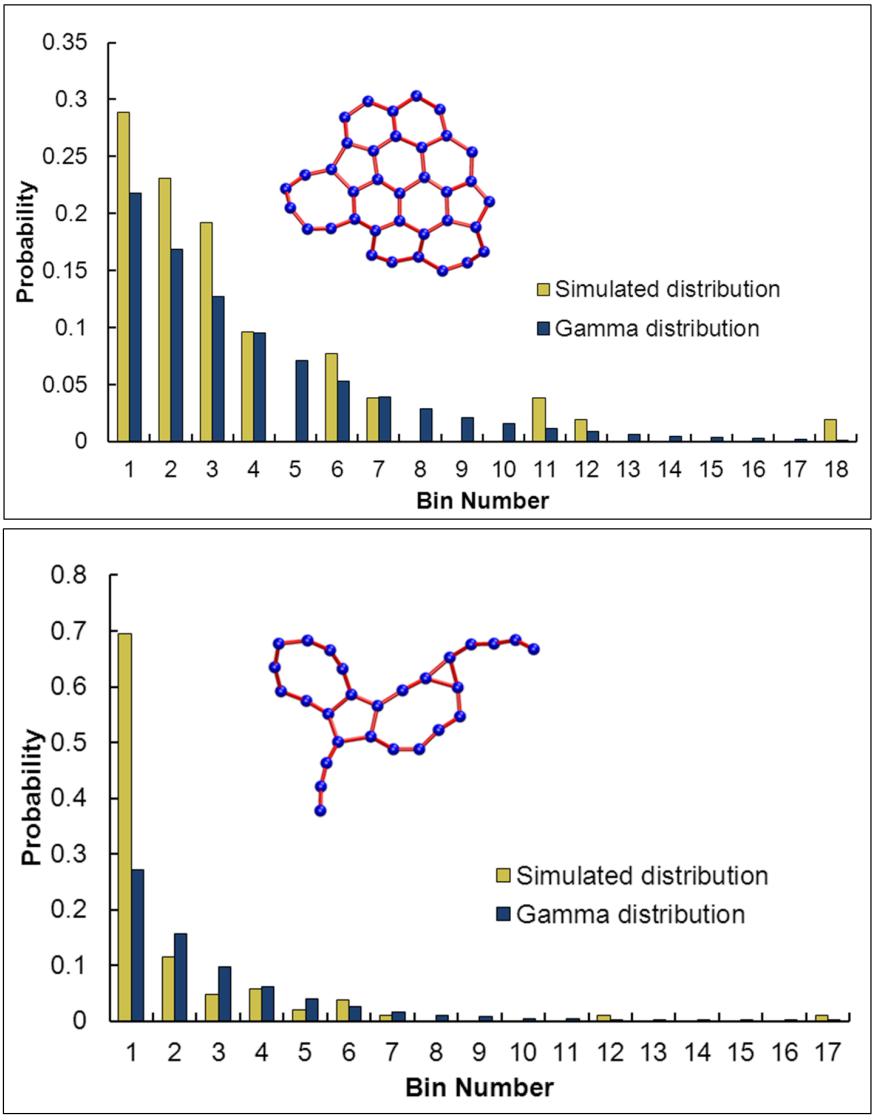

Figure 38. Probability distribuition of carbon clusters (based on atom numbers in each cluster). (top) Simulated and gamma (blue; $\alpha = 1.0832$ and $\theta = 3.177804$) probability distributions of obtained cluster sizes, when $4,100$ carbon atoms (atom density, $\rho = 4.0 \times 10^{-}6$ Å^{-3}) are simulated at $2,000$ K (snapshot taken at 50 ns). (bottom) Simulated and gamma (blue; $\alpha = 0.7571$ and $\theta = 2.5915$) probability distributions of obtained cluster sizes, when $4,100$ carbon atoms (atom density, $\rho = 4.0 \times 10^{-}6$ Å^{-3}) are simulated at $3,000$ K (snapshot taken at 40 ns). The bin size is 25 carbon atoms.

Gamma distribution functions and the parameters for each distribution are given in the figure captions.

As shown in Figure 36 (top) with 4,100 atoms at 500 K and sampled at 200 ns, we found that carbon clusters containing $\approx$ 100 atoms more likely form. For 10,000 atoms at 500 K, sampled at 200 ns, Figure 36 (bottom), we found nearly the same probability distributions of carbon clusters. For longer equilibration times, several small clusters can merge to big clusters. Next, we determined the probability distribution for 4,100 C atoms, Figure 37 (top), and 10,000 C atoms, Figure 37 (bottom), at 1,000 K, sampled at 100 ns. In this case, we observed that the most probable carbon clusters consist of $\approx$ 75. We also observed that at 1,000 K, the ring sizes are smaller in the clusters compare to the clusters at 500 K, as previously discussed. At 2,000 K, several small graphene flakes and few large curved clusters, with five- and six-member rings (bowl shape) are observed along with chains molecules. The high formation probability of the small clusters ($\approx$ 35) is also confirmed by the probability distribution analysis in Figure 38 (top) with 4,100 C atoms at 2,000 K, sampled at 50 ns of simulations. When we increase the temperature to 3,000 K (4,100 C atoms and simulation time of 40 ns), we find several small structures along with fullerene type clusters. The formation of several clusters can be explained by the high thermal energy in the system. Representative structures formed after the sampling times are shown as inset in each figure.

10.4 Conclusion

In this chapter, we demonstrate synthesis of large carbon structures in gas phase by using reactive MD simulations. The formation mechanism of the large clusters and graphene type

structures were investigated by a series of simulations. The influence of the temperature and particle density on the shape of structures were studied. It is found that at high temperature (2,000-3,000 K) fullerene type clusters are obtained, whereas at relatively low temperature graphene type sheets along with long chain molecules/structures are synthesized. The effect of hydrogen atom addition on the structure of carbon clusters is also studied. At high temperature, fullerene type clusters are found whereas short and branched chains molecules, terminated with hydrogen atoms, are observed at low temperature. At higher density of hydrogen atoms, we find that small unsaturated carbon chains are formed. When the concentration of hydrogen are relative low graphene type sheet (terminated by hydrogen atoms) and small cluster are observed. We simulate the self-assembly of carbon structures, in non-equilibrium conditions of periodic carbon inflow, resembling the astrophysical conditions. The analytical expressions can be used to predict the timescale of the formation of nanostructures in interstellar medium. Finally, we determine the probability distributions of cluster sizes at different temperatures and initial C atom number and compare them with the gamma-distribution.

CHAPTER 11

CONCLUDING REMARKS

The research described in this thesis contributes to the understanding of self-assembly of various building blocks (atoms, molecules, graphenes) and nanomedicines, with various applications in drug delivery and chemical separations. We have implemented several theoretical and computational methods at different length scales to describe the modeled systems. We have used all-atom, reactive and coarse-grained MD, and *ab-initio* approaches to investigate the self-assembly of nanomaterials in various media, stability and structural properties of the self-assembled systems. The computational models of the studied systems are sufficiently realistic to chemical and physical properties of their experimental analogues and can potentially be used to investigate new phenomena. In fact, some of our simulations has been experimentally realized later [280] and many of my computational studies were performed to explain experimental results of our collaborations.

We have demonstrated by classical MD simulations that water nanodroplets can activate and guide folding of graphene nanostructures. The self-assembly phenomena can be realized by different types of motions, such as bending, sliding, rolling or zipping that lead to stable or metastable structures, such as sandwiches, capsules, knots and rings. These complex nanostructures can be potentially used as building blocks of functional nanodevices, with unique mechanical, electrical or optical properties

We have shown by classical MD that carbon nanotubes can control and guide the self-assembly of planar graphene nanostructures on their surfaces and in their interiors in vacuum and in solvents. The self-assembly can proceed by sliding, folding, and rolling motions, leading to stable or metastable bulky nanostructures, such as knots, rings, and helices. The GNRs can also hybridize with other nanostructures. The novel hybrid materials can have unique mechanical, electrical and optical properties, and numerous potential applications.

By using CGMD, we have demonstrated that kinetically stable micelles filled with molecules in water could be prepared on CNT surfaces. The sizes and filling of the formed micelles could be controlled by the preparation conditions. We have shown that the lifetimes of the formed micelles depend on their size, the monomers used, the molecules carried, and the solution. The outlined methodology can be potentially used in molecular storage, protection, manipulation, and delivery.

We have used classical MD simulations to show that PCNTs could be used in selective molecular absorption, transport, and separation. We have shown that saturated water vapor can be condensed inside PCNTs and pumped out by it, which might be used in active desiccation. It cans also be used to separate different types of ions from ionic solutions and pumped away through charged PCNTs, which might be used in batteries and supercapacitors. PCNTs can also be used as molecular sieves, where molecules can be efficiently separated based on their coupling to PCNTs. Therefore, PCNTs can be used as an important class of materials with a broad range of applications.

Self-assembly of PEGylated linear and dendron-based branched copolymers into micellar aggregates are studied by atomistic MD simulations. We have characterized the structures and dynamics of the self-assembled micelles. We have shown that DC-based micelles exhibit a significantly greater surface coverage of hydrophilic layers than the linear polymer-based micelles. The highly stable supramolecular assemblies with highly hydrophilic PEG surfaces, and biocompatibility could provide a novel, versatile drug delivery platform.

We have investigated the binding characteristics of monovalent ions to graphene-like H-passivated flakes in vacuum and in water by quantum chemical calculations. We have shown that anions either are physisorbed onto the nanostructures or covalently bind at their selected regions, depending on the initial conditions, whereas cations only physisorb onto them.

Finally, we have demonstrated the self-assembly of carbon or/hydrogen atoms in gas phase, leading to long chains, graphene and complex cage structures, by using reactive MD simulations. The influence of the temperature and particle density on the shape of structures were studied. At high temperature ($2,000$-$3,000$ K) fullerene type clusters were obtained, whereas at relatively low temperature graphene type sheets along with long chain molecules/structures were formed. The derived analytical expressions can be used to predict the time scale of the formation of nanostructures in interstellar medium. Probability distributions of cluster sizes at different temperatures were determined.

In all the above studies, we have shown how we can control the structure and dynamics of nanoscale systems. The studied systems can be used to perform variety of tasks, such as drug delivery and separation of liquid mixtures. In the future, self-assembled nanostructures could

be used as building blocks to build macro-systems. These studied self-assembled complex and hybrid nanostructures could enrich the spectrum of new materials at the nanoscale.

CITED LITERATURE

1. Binnig, G., Rohrer, H., Gerber, C., and Weibel, E.: Surface studies by scanning tunneling microscopy. Phys. Rev. Lett., 49:57–61, 1982.

2. Binnig, G., Quate, C. F., and Gerber, C.: Atomic force microscope. Phys. Rev. Lett., 56:930–933, 1986.

3. Ashkin, A., Dziedzic, J. M., Bjorkholm, J. E., and Chu, S.: Observation of a single-beam gradient force optical trap for dielectric particles. Opt. Lett., 11(5):288–290, 1986.

4. Eigler, D. M., Weiss, P. S., Schweizer, E. K., and Lang, N. D.: Imaging Xe with a low-temperature scanning tunneling microscope. Phys. Rev. Lett., 66:1189–1192, 1991.

5. Gross, L., Mohn, F., Moll, N., Schuler, B., Criado, A., Guitin, E., Pea, D., Gourdon, A., and Meyer, G.: Bond-order discrimination by atomic force microscopy. Science, 337(6100):1326–1329, 2012.

6. Rief, M., Oesterhelt, F., Heymann, B., and Gaub, H. E.: Single molecule force spectroscopy on polysaccharides by atomic force microscopy. Science, 275(5304):1295–1297, 1997.

7. Cui, X. D., Primak, A., Zarate, X., Tomfohr, J., Sankey, O. F., Moore, A. L., Moore, T. A., Gust, D., Harris, G., and Lindsay, S. M.: Reproducible measurement of single-molecule conductivity. Science, 294(5542):571–574, 2001.

8. Schuler, B., Lipman, E. A., and Eaton, W. A.: Probing the free-energy surface for protein folding with single-molecule fluorescence spectroscopy. Nature, 419(6908):743–747, 2002.

9. Murray, C. B., Norris, D. J., and Bawendi, M. G.: Synthesis and characterization of nearly monodisperse CdE (E = sulfur, selenium, tellurium) semiconductor nanocrystallites. J. Am. Chem. Soc., 115(19):8706–8715, 1993.

10. Alivisatos, A. P.: Semiconductor clusters, nanocrystals, and quantum dots. Science, 271(5251):933–937, 1996.

11. Hu, J., Odom, T. W., and Lieber, C. M.: Chemistry and physics in one dimension: Synthesis and properties of nanowires and nanotubes. Acc. Chem. Res., 32(5):435–445, 1999.

12. Hafeman, D., Parce, J., and McConnell, H.: Light-addressable potentiometric sensor for biochemical systems. Science, 240(4856):1182–1185, 1988.

13. Bruchez, M., Moronne, M., Gin, P., Weiss, S., and Alivisatos, A. P.: Semiconductor nanocrystals as fluorescent biological labels. Science, 281(5385):2013–2016, 1998.

14. Dubertret, B., Skourides, P., Norris, D. J., Noireaux, V., Brivanlou, A. H., and Libchaber, A.: In vivo imaging of quantum dots encapsulated in phospholipid micelles. Science, 298(5599):1759–1762, 2002.

15. Barbé, C. J., Arendse, F., Comte, P., Jirousek, M., Lenzmann, F., Shklover, V., and Grätzel, M.: Nanocrystalline titanium oxide electrodes for photovoltaic applications. J. Am. Ceram. Soc., 80(12):3157–3171, 1997.

16. Kroto, H. W., Heath, J. R., O'Brien, S. C., Curl, R. F., and Smalley, R. E.: C_{60}: Buckminsterfullerene. Nature, 318(6042):162–163, 1985.

17. Iijima, S.: Helical microtubules of graphitic carbon. Nature, 354(6348):56–58, 1991.

18. Novoselov, K. S., Geim, A. K., Morozov, S. V., Jiang, D., Katsnelson, M. I., Grigorieva, I. V., Dubonos, S. V., and Firsov, A. A.: Two-dimensional gas of massless dirac fermions in graphene. Nature, 438(7065):197–200, 2005.

19. Geim, A. K. and Novoselov, K. S.: The rise of graphene. Nat. Mater., 6(3):183–191, 2007.

20. Zhao, G., Perilla, J. R., Yufenyuy, E. L., Meng, X., Chen, B., Ning, J., Ahn, J., Gronenborn, A. M., Schulten, K., Aiken, C., and Zhang, P.: Mature HIV-1 capsid structure by cryo-electron microscopy and all-atom molecular dynamics. Nature, 497(7451):643–646, 2013.

21. Kohn, W. and Sham, L. J.: Self-consistent equations including exchange and correlation effects. Phys. Rev., 140:A1133–A1138, 1965.

22. Born, M. and Oppenheimer, R.: Quantum theory of molecule. Ann. d. Physik, 84(12):457–484, 1927.

23. Szabo, A. and Ostlund, N. S.: Modern Quantum Chemistry. New York, Dover Publication, 1989.

24. Hohenberg, P. and Kohn, W.: Inhomogeneous electron gas. Phys. Rev., 136:B864–B871, 1964.

25. Lee, C., Yang, W., and Parr, R. G.: Development of the colle-salvetti correlation-energy formula into a functional of the electron density. Phys. Rev. B, 37:785–789, 1988.

26. St.-Amant, A., Cornell, W. D., Kollman, P. A., and Halgren, T. A.: Calculation of molecular geometries, relative conformational energies, dipole moments, and molecular electrostatic potential fitted charges of small organic molecules of biochemical interest by density functional theory. Journal of Computational Chemistry, 16(12):1483–1506, 1995.

27. Becke, A. D.: Density-functional exchange-energy approximation with correct asymptotic behavior. Phys. Rev. A, 38:3098–3100, 1988.

28. Vosko, S. H., Wilk, L., and Nusair, M.: Accurate spin-dependent electron liquid correlation energies for local spin density calculations: a critical analysis. Can. J. Phys., 58(8):1200–1211, 1980.

29. MacKerell, A. D., Bashford, D., Bellott, Dunbrack, R. L., Evanseck, J. D., Field, M. J., Fischer, S., Gao, J., Guo, H., Ha, S., Joseph-McCarthy, D., Kuchnir, L., Kuczera, K., Lau, F. T. K., Mattos, C., Michnick, S., Ngo, T., Nguyen, D. T., Prodhom, B., Reiher, W. E., Roux, B., Schlenkrich, M., Smith, J. C., Stote, R., Straub, J., Watanabe, M., Wirkiewicz-Kuczera, J., Yin, D., and Karplus, M.: All-atom empirical potential for molecular modeling and dynamics studies of proteins. J. Phys. Chem. B, 102(18):3586–3616, 1998.

30. Phillips, J. C., Braun, R., Wang, W., Gumbart, J., Tajkhorshid, E., Villa, E., Chipot, C., Skeel, R. D., Kalé, L., and Schulten, K.: Scalable molecular dynamics with NAMD. J. Comput. Chem., 26(16):1781–1802, 2005.

31. Darden, T., York, D., and Pedersen, L.: Particle mesh ewald: An N.log(N) method for ewald sums in large systems. J. Chem. Phys., 98(12):10089–10092, 1993.

32. Lee, H., Venable, R. M., Jr., A. D. M., and Pastor, R. W.: Molecular dynamics studies of polyethylene oxide and polyethylene glycol: Hydrodynamic radius and shape anisotropy. Biophys. J., 95(4):1590–1599, 2008.

33. Duan, Y., Wu, C., Chowdhury, S., Lee, M. C., Xiong, G., Zhang, W., Yang, R., Cieplak, P., Luo, R., Lee, T., Caldwell, J., Wang, J., and Kollman, P.: A point-charge force field for molecular mechanics simulations of proteins based on condensed-phase quantum mechanical calculations. J. Comput. Chem., 24(16):1999–2012, 2003.

34. Jorgensen, W. L. and Tirado-Rives, J.: The OPLS [optimized potentials for liquid simulations] potential functions for proteins, energy minimizations for crystals of cyclic peptides and crambin. J. Am. Chem. Soc., 110(6):1657–1666, 1988.

35. Jorgensen, W. L., Maxwell, D. S., and Tirado-Rives, J.: Development and testing of the opls all-atom force field on conformational energetics and properties of organic liquids. J. Am. Chem. Soc., 118(45):11225–11236, 1996.

36. Oostenbrink, C., Villa, A., Mark, A. E., and Van Gunsteren, W. F.: A biomolecular force field based on the free enthalpy of hydration and solvation: The gromos force-field parameter sets 53A5 and 53A6. J. Comput. Chem., 25(13):1656–1676, 2004.

37. Tersoff, J.: New empirical approach for the structure and energy of covalent systems. Phys. Rev. B, 37:6991–7000, 1988.

38. Tersoff, J.: Modeling solid-state chemistry: Interatomic potentials for multicomponent systems. Phys. Rev. B, 39:5566–5568, 1989.

39. Brenner, D. W.: Empirical potential for hydrocarbons for use in simulating the chemical vapor deposition of diamond films. Phys. Rev. B, 42:9458–9471, 1990.

40. Stuart, S. J., Tutein, A. B., and Harrison, J. A.: A reactive potential for hydrocarbons with intermolecular interactions. J. Chem. Phys., 112(14):6472–6486, 2000.

41. Frenkel, D. and Smit, B.: Molecular simulation from algorithms to applications. CA, Academic Press: San Diego, 2002.

42. Servantie, J. and Gaspard, P.: Methods of calculation of a friction coefficient: Application to nanotubes. Phys. Rev. Lett., 91:185503, 2003.

43. Humphrey, W., Dalke, A., and Schulten, K.: VMD: Visual molecular dynamics. J. Mol. Graph., 14(1):33–38, 1996.

44. Noguchi, H. and Takasu, M.: Self-assembly of amphiphiles into vesicles: A brownian dynamics simulation. Phys. Rev. E, 64:041913, 2001.

45. Farago, O.: "Water-free" computer model for fluid bilayer membranes. J. Chem. Phys., 119(1):596–605, 2003.

46. Sevink, G. J. A. and Zvelindovsky, A. V.: Self-assembly of complex vesicles. Macromolecules, 38(17):7502–7513, 2005.

47. Murtola, T., Falck, E., Patra, M., Karttunen, M., and Vattulainen, I.: Coarse-grained model for phospholipid/cholesterol bilayer. J. Chem. Phys., 121(18):9156–9165, 2004.

48. Brannigan, G. and Brown, F. L. H.: Solvent-free simulations of fluid membrane bilayers. J. Chem. Phys., 120(2):1059–1071, 2004.

49. Shelley, J. C., Shelley, M. Y., Reeder, R. C., Bandyopadhyay, S., and Klein, M. L.: A coarse grain model for phospholipid simulations. J. Phys. Chem. B, 105(19):4464–4470, 2001.

50. Marrink, S. J., de Vries, A. H., and Mark, A. E.: Coarse grained model for semiquantitative lipid simulations. J. Phys. Chem. B, 108(2):750–760, 2004.

51. Marrink, S. J., Risselada, H. J., Yefimov, S., Tieleman, D. P., and de Vries, A. H.: The martini force field: coarse grained model for biomolecular simulations. J. Phys. Chem. B, 111(27):7812–7824, 2007.

52. Warshel, A. and Karplus, M.: Calculation of ground and excited state potential surfaces of conjugated molecules. i. formulation and parametrization. J. Am. Chem. Soc., 94(16):5612–5625, 1972.

53. Warshel, A. and Levitt, M.: Theoretical studies of enzymic reactions: Dielectric, electrostatic and steric stabilization of the carbonium ion in the reaction of lysozyme. J. Mol. Biol., 103(2):227 – 249, 1976.

54. Shao, Y., Molnar, L. F., Jung, Y., Kussmann, J., Ochsenfeld, C., Brown, S. T., Gilbert, A. T., Slipchenko, L. V., Levchenko, S. V., O'Neill, D. P., DiStasio Jr, R. A., Lochan, R. C., Wang, T., Beran, G. J., Besley, N. A., Herbert, J. M., Yeh Lin, C., Van Voorhis, T., Hung Chien, S., Sodt, A., Steele, R. P., Rassolov, V. A., Maslen, P. E., Korambath, P. P., Adamson, R. D., Austin, B., Baker, J., Byrd, E. F. C., Dachsel, H., Doerksen, R. J., Dreuw, A., Dunietz, B. D., Dutoi, A. D., Furlani, T. R., Gwaltney, S. R., Heyden, A., Hirata, S., Hsu, C.-P., Kedziora, G., Khalliulin, R. Z., Klunzinger, P., Lee, A. M., Lee, M. S., Liang, W., Lotan, I., Nair,

N., Peters, B., Proynov, E. I., Pieniazek, P. A., Min Rhee, Y., Ritchie, J., Rosta, E., David Sherrill, C., Simmonett, A. C., Subotnik, J. E., Lee Woodcock III, H., Zhang, W., Bell, A. T., Chakraborty, A. K., Chipman, D. M., Keil, F. J., Warshel, A., Hehre, W. J., Schaefer III, H. F., Kong, J., Krylov, A. I., Gill, P. M. W., and Head-Gordon, M.: Advances in methods and algorithms in a modern quantum chemistry program package. Phys. Chem. Chem. Phys., 8:3172–3191, 2006.

55. Ufimtsev, I. S. and Martinez, T. J.: Quantum chemistry on graphical processing units. 1. strategies for two-electron integral evaluation. J. Chem. Theory Comput., 4(2):222–231, 2008.

56. Shimomura, M. and Sawadaishi, T.: Bottom-up strategy of materials fabrication: A new trend in nanotechnology of soft materials. Curr. Opin. Colloid. Interface Sci., 6(1):11–16, 2001.

57. Whitesides, G.: Nanoscience, nanotechnology, and chemistry. Small, 1(2):172–179, 2005.

58. Addadi, L. and Weiner, S.: Biomineralization: Crystals, asymmetry and life. Nature, 411(6839):753–755, 2001.

59. Nam, K. T., Kim, D.-W., Yoo, P. J., Chiang, C.-Y., Meethong, N., Hammond, P. T., Chiang, Y.-M., and Belcher, A. M.: Virus-enabled synthesis and assembly of nanowires for lithium ion battery electrodes. Science, 312(5775):885–888, 2006.

60. Talapin, D. V., Shevchenko, E. V., Murray, C. B., Titov, A. V., and Král, P.: Dipole-dipole interactions in nanoparticle superlattices. Nano Lett., 7(5):1213–1219, 2007.

61. Shevchenko, E. V., Talapin, D. V., Kotov, N. A., O'Brien, S., and Murray, C. B.: Structural diversity in binary nanoparticle superlattices. Nature, 439(7072):55–59, 2006.

62. Bigioni, T. P., Lin, X.-M., Nguyen, T. T., Corwin, E. I., Witten, T. A., and Jaeger, H. M.: Kinetically driven self assembly of highly ordered nanoparticle monolayers. Nature Mater., 5(4):265–270, 2006.

63. Kalsin, A. M., Fialkowski, M., Paszewski, M., Smoukov, S. K., Bishop, K. J. M., and Grzybowski, B. A.: Electrostatic self-assembly of binary nanoparticle crystals with a diamond-like lattice. Science, 312(5772):420–424, 2006.

64. DeVries, G. A., Brunnbauer, M., Hu, Y., Jackson, A. M., Long, B., Neltner, B. T., Uzun, O., Wunsch, B. H., and Stellacci, F.: Divalent metal nanoparticles. Science, 315(5810):358–361, 2007.

65. Li, L.-S. and Alivisatos, A.: Semiconductor nanorod liquid crystals and their assembly on a substrate. Adv. Mater., 15(5):408–411, 2003.

66. Titov, A. V. and Král, P.: Modeling the self-assembly of colloidal nanorod superlattices. Nano Lett., 8(11):3605–3612, 2008.

67. Novoselov, K. S., Geim, A. K., Morozov, S. V., Jiang, D., Zhang, Y., Dubonos, S. V., Grigorieva, I. V., and Firsov, A. A.: Electric field effect in atomically thin carbon films. Science, 306(5696):666–669, 2004.

68. Berner, S., Corso, M., Widmer, R., Groening, O., Laskowski, R., Blaha, P., Schwarz, K., Goriachko, A., Over, H., Gsell, S., Schreck, M., Sachdev, H., Greber, T., and Osterwalder, J.: Boron nitride nanomesh: Functionality from a corrugated monolayer. Angew. Chem., Int. Ed., 46(27):5115–5119, 2007.

69. Laskowski, R., Blaha, P., Gallauner, T., and Schwarz, K.: Single-layer model of the hexagonal boron nitride nanomesh on the rh(111) surface. Phys. Rev. Lett., 98:106802, 2007.

70. Li, X., Wang, X., Zhang, L., Lee, S., and Dai, H.: Chemically derived, ultrasmooth graphene nanoribbon semiconductors. Science, 319(5867):1229–1232, 2008.

71. Jiao, L., Zhang, L., Wang, X., Diankov, G., and Dai, H.: Narrow graphene nanoribbons from carbon nanotubes. Nature, 458(7240):877–880, 2009.

72. Kosynkin, D. V., Higginbotham, A. L., Sinitskii, A., Lomeda, J. R., Dimiev, A., Price, B. K., and Tour, J. M.: Longitudinal unzipping of carbon nanotubes to form graphene nanoribbons. Nature, 458(7240):872–876, 2009.

73. Tapaszto, L., Dobrik, G., Lambin, P., and Biro, L. P.: Tailoring the atomic structure of graphene nanoribbons by scanning tunnelling microscope lithography. Nat. Nano., 3(7):397–401, 2008.

74. Stampfer, C., Güttinger, J., Hellmüller, S., Molitor, F., Ensslin, K., and Ihn, T.: Energy gaps in etched graphene nanoribbons. Phys. Rev. Lett., 102:056403, 2009.

75. Ci, L., Xu, Z., Wang, L., Gao, W., Ding, F., Kelly, K., Yakobson, B., and Ajayan, P.: Controlled nanocutting of graphene. Nano Res., 1(2):116–122, 2008.

76. Campos, L. C., Manfrinato, V. R., Sanchez-Yamagishi, J. D., Kong, J., and Jarillo-Herrero, P.: Anisotropic etching and nanoribbon formation in single-layer graphene. Nano Lett., 9(7):2600–2604, 2009.

77. Zhu, Z., Su, D., Weinberg, G., and Schlögl, R.: Supermolecular self-assembly of graphene sheets: formation of tube-in-tube nanostructures. Nano Lett., 4(11):2255–2259, 2004.

78. Jin, W., Fukushima, T., Niki, M., Kosaka, A., Ishii, N., and Aida, T.: Self-assembled graphitic nanotubes with one-handed helical arrays of a chiral amphiphilic molecular graphene. Proc. Natl. Acad. Sci. USA, 102(31):10801–10806, 2005.

79. Chen, Q., Chen, T., Pan, G.-B., Yan, H.-J., Song, W.-G., Wan, L.-J., Li, Z.-T., Wang, Z.-H., Shang, B., Yuan, L.-F., and Yang, J.-L.: Structural selection of graphene supramolecular assembly oriented by molecular conformation and alkyl chain. Proc. Natl. Acad. Sci. USA, 105(44):16849–16854, 2008.

80. Lee, C., Wei, X., Kysar, J. W., and Hone, J.: Measurement of the elastic properties and intrinsic strength of monolayer graphene. Science, 321(5887):385–388, 2008.

81. Bunch, J. S., Verbridge, S. S., Alden, J. S., van der Zande, A. M., Parpia, J. M., Craighead, H. G., and McEuen, P. L.: Impermeable atomic membranes from graphene sheets. Nano Lett., 8(8):2458–2462, 2008.

82. Gómez-Navarro, C., Burghard, M., and Kern, K.: Elastic properties of chemically derived single graphene sheets. Nano Lett., 8(7):2045–2049, 2008.

83. Viculis, L. M., Mack, J. J., and Kaner, R. B.: A chemical route to carbon nanoscrolls. Science, 299(5611):1361, 2003.

84. Braga, S. F., Coluci, V. R., Legoas, S. B., Giro, R., Galvo, D. S., and Baughman, R. H.: Structure and dynamics of carbon nanoscrolls. Nano Lett., 4(5):881–884, 2004.

85. Yu, D. and Liu, F.: Synthesis of carbon nanotubes by rolling up patterned graphene nanoribbons using selective atomic adsorption. Nano Lett., 7(10):3046–3050, 2007.

86. Sidorov, A., Mudd, D., Sumanasekera, G., Ouseph, P. J., Jayanthi, C. S., and Wu, S.-Y.: Electrostatic deposition of graphene in a gaseous environment: a deterministic route for synthesizing rolled graphenes? Nanotechnology, 20(5):055611, 2009.

87. Wang, B. and Král, P.: Dragging of polarizable nanodroplets by distantly solvated ions. Phys. Rev. Lett., 101:046103, 2008.

88. Martel, R., Shea, H. R., and Avouris, P.: Ring formation in single-wall carbon nanotubes. J. Phys. Chem. B., 103(36):7551–7556, 1999.

89. Huang, J., Juszkiewicz, M., de Jeu, W. H., Cerda, E., Emrick, T., Menon, N., and Russell, T. P.: Capillary wrinkling of floating thin polymer films. Science, 317(5838):650–653, 2007.

90. Py, C., Reverdy, P., Doppler, L., Bico, J., Roman, B., and Baroud, C. N.: Capillary origami: Spontaneous wrapping of a droplet with an elastic sheet. Phys. Rev. Lett., 98:156103, 2007.

91. Ellis, R. J. and van der Vies, S. M.: Molecular chaperones. Annu. Rev. Biochem., 60(1):321–347, 1991.

92. In the md simulations, we apply the langevin dynamics with 0.01 ps^{-1} damping coefficient, to minimize the unphysical loss of momentum [87], and the time step is 1 fs. the systems are simulated as nvt ensembles inside periodic cells of the following sizes: Figure 2 ($55 \times 35 \times 35$ nm^3), Figure 3 (up) ($30 \times 35 \times 35$ nm^3), Figure 3 (bottom) ($30 \times 35 \times 35$ nm^3), Figure 4 ($15 \times 85 \times 25$ nm^3), Figure 5 ($20 \times 120 \times 20$ nm^3), Figure 7 ($20 \times 75 \times 20$ nm^3) and Figure 8 ($60 \times 85 \times 60$ nm^3). the bn sheet, shown in Figure 8, have charges of e and -e on the boron and nitrogen atoms, respectively [87]. the graphene-water (or graphene-graphene) binding energies are calculated as the difference of the total vdw energy of the system, when the system components are at the normal binding distance, and when they are separated by 5 nm. averaging of the energies is done over 100 consecutive frames of the simulation trajectory, with a 1 ps time interval.

93. Tersoff, J.: Energies of fullerenes. Phys. Rev. B, 46:15546–15549, 1992.

94. Kudin, K. N., Scuseria, G. E., and Yakobson, B. I.: C_2F, BN, and C nanoshell elasticity from *ab initio* computations. Phys. Rev. B, 64:235406, 2001.

95. Arroyo, M. and Belytschko, T.: Finite crystal elasticity of carbon nanotubes based on the exponential cauchy-born rule. Phys. Rev. B, 69:115415, 2004.

96. Lu, Q., Arroyo, M., and Huang, R.: Elastic bending modulus of monolayer graphene. J. Phy. D: Appl. Phys., 42(10):102002, 2009.

97. Juniper, B. E., Robins, R. J., and Joel, D. M.: The carnivorous plants. CA, Academic Press: San Diego, 1989.

98. Lee, K.-B., Park, S.-J., Mirkin, C. A., Smith, J. C., and Mrksich, M.: Protein nanoarrays generated by dip-pen nanolithography. Science, 295(5560):1702–1705, 2002.

99. Duwez, A.-S., Cuenot, S., Jerome, C., Gabriel, S., Jerome, R., Rapino, S., and Zerbetto, F.: Mechanochemistry: targeted delivery of single molecules. Nat. Nano., 1(2):122–125, 2006.

100. Walther, J. H., Werder, T., Jaffe, R. L., Gonnet, P., Bergdorf, M., Zimmerli, U., and Koumoutsakos, P.: Water-carbon interactions III: The influence of surface and fluid impurities. Phys. Chem. Chem. Phys., 6:1988–1995, 2004.

101. Baughman, R. H., Cui, C., Zakhidov, A. A., Iqbal, Z., Barisci, J. N., Spinks, G. M., Wallace, G. G., Mazzoldi, A., De Rossi, D., Rinzler, A. G., Jaschinski, O., Roth, S., and Kertesz, M.: Carbon nanotube actuators. Science, 284(5418):1340–1344, 1999.

102. Jiao, L., Wang, X., Diankov, G., Wang, H., and Dai, H.: Facile synthesis of high-quality graphene nanoribbons. Nat. Nano., 5(5):321–325, 2010.

103. Patra, N., Wang, B., and Král, P.: Nanodroplet activated and guided folding of graphene nanostructures. Nano Lett., 9(11):3766–3771, 2009.

104. Buldum, A. and Lu, J. P.: Atomic scale sliding and rolling of carbon nanotubes. Phys. Rev. Lett., 83:5050–5053, 1999.

105. Ortolani, L., Houdellier, F., Monthioux, M., and Morandi, V.: Chirality dependent surface adhesion of single-walled carbon nanotubes on graphene surfaces. Carbon, 48(11):3050–3056, 2010.

106. Wang, B., Král, P., and Thanopulos, I.: Docking of chiral molecules on twisted and helical nanotubes: nanomechanical control of catalysis. Nano Lett., 6(9):1918–1921, 2006.

107. Atalaya, J., Isacsson, A., and Kinaret, J. M.: Continuum elastic modeling of graphene resonators. Nano Lett., 8(12):4196–4200, 2008.

108. (1) we evaluate σ_{sym} by placing a small (≈ 9.1 nm^2) relaxed hexagonal piece of graphene on a large fixed square graphene. after relaxation, they adjust their positions to (graphite-like) AB-form interlayer stacking (half of the atoms sitting above each other). we assign the angle of $\varphi = 0$ to this locked orientation. then, we rotate the hexagonal graphene flake around its center and calculate by *VMD* the total energy ($T = 20$ K). the E_{C-G} total energy has a C_6 symmetry: it increases sharply at the first $\delta\varphi \approx 3^\circ$ of rotation and keeps relatively constant until it sharply returns to its minimum energy at $\varphi = 60^\circ$, and so on. the *CNT-GNR* binding energy density, $\langle\sigma_{C-G}\rangle$, is calculated as the maximum (in value) vdw energy per unit area of the system ($\varphi = 30^\circ$). due to sharp localization of the energy minima, we consider nonzero σ_{sym} only at $\varphi = n\,60^\circ$ and define it as the energy difference per unit area between the energy maxima ($\varphi = 30^\circ$) and minima points ($\varphi = 0$). averaging of the energies are done over 100 consecutive frames of the simulation trajectory, with a 1 ps time interval. (2) the *GNR-GNR* sidewise *vdW* energy density, σ_{G-G}, is calculated as the difference of the (averaged) energies per unit length of two *GNRs* placed in a plane and separated by 0.35 and 5 nm (both fixed). their armchair structures are facing each other without any sidewise shifting. (3) in order to validate the *CHARMM27* force field parameters, we calculate the flexural rigidity, as in ref. [103], the young's modulus of graphene (*GNR*), as in ref. [133], and the average graphene-graphene *vdw* binding energy. we obtain the flexural rigidity of $d \approx 27.9$ kcal/mol and the young's modulus of $e \approx 0.9$ tpa, where the used bond and angular constants are 322.5 kcal mol^{-1}Å^{-2} and 53.35 kcal mol^{-1} rad^{-2}, respectively. the average graphene-graphene *vdW* energy is 56 kcal/mol/nm^2 (0.024 ev/Å^2).

109. Wang, B. and Král, P.: Optimal atomistic modifications of material surfaces: Design of selective nesting sites for biomolecules. Small, 3(4):580–584, 2007.

110. Zhang, Z. and Li, T.: Carbon nanotube initiated formation of carbon nanoscrolls. Appl. Phys. Lett., 97(8):081909, 2010.

111. Li, K., Pandit, S., Guccione, S., and Bednarski, M.: Molecular imaging applications in nanomedicine. Biomed. Microdevices, 6(2):113–116, 2004.

112. Kwon, G. S. and Okano, T.: Polymeric micelles as new drug carriers. Adv. Drug Delivery Rev., 21(2):107 – 116, 1996.

113. Gu, F., Zhang, L., Teply, B. A., Mann, N., Wang, A., Radovic-Moreno, A. F., Langer, R., and Farokhzad, O. C.: Precise engineering of targeted nanoparticles by using self-assembled biointegrated block copolymers. Proc. Natl. Acad. Sci. USA, 105(7):2586–2591, 2008.

114. Ashok, B., Arleth, L., Hjelm, R. P., Rubinstein, I., and Önyüksel, H.: In vitro characterization of PEGylated phospholipid micelles for improved drug solubilization: Effects of PEG chain length and PC incorporation. J. Pharma. Sci., 93(10):2476–2487, 2004.

115. Bond, P. J., Cuthbertson, J. M., Deol, S. S., and Sansom, M. S. P.: MD simulations of spontaneous membrane protein/detergent micelle formation. J. Am. Chem. Soc., 126(49):15948–15949, 2004.

116. Otsuka, H., Nagasaki, Y., and Kataoka, K.: Pegylated nanoparticles for biological and pharmaceutical applications. Adv. Drug Delivery Rev., 55(3):403 – 419, 2003.

117. Torchilin, V. P.: Structure and design of polymeric surfactant-based drug delivery systems. J. Controlled Release, 73(23):137–172, 2001.

118. Cui, X., Mao, S., Liu, M., Yuan, H., and Du, Y.: Mechanism of surfactant micelle formation. Langmuir, 24(19):10771–10775, 2008.

119. Moore, V. C., Strano, M. S., Haroz, E. H., Hauge, R. H., Smalley, R. E., Schmidt, J., and Talmon, Y.: Individually suspended single-walled carbon nanotubes in various surfactants. Nano Lett., 3(10):1379–1382, 2003.

120. Wu, Y., Hudson, J. S., Lu, Q., Moore, J. M., Mount, A. S., Rao, A. M., Alexov, E., and Ke, P. C.: Coating single-walled carbon nanotubes with phospholipids. J. Phys. Chem. B, 110(6):2475–2478, 2006.

121. Qiao, R. and Ke, P. C.: Lipid-carbon nanotube self-assembly in aqueous solution. J. Am. Chem. Soc., 128(42):13656–13657, 2006.

122. Wallace, E. J. and Sansom, M. S. P.: Carbon nanotube self-assembly with lipids and detergent: a molecular dynamics study. Nanotechnology, 20(4):045101, 2009.

123. Arai, N., Yasuoka, K., and Zeng, X. C.: Self-assembly of surfactants and polymorphic transition in nanotubes. J. Am. Chem. Soc., 130(25):7916–7920, 2008.

124. Islam, M. F., Rojas, E., Bergey, D. M., Johnson, A. T., and Yodh, A. G.: High weight fraction surfactant solubilization of single-wall carbon nanotubes in water. Nano Lett., 3(2):269–273, 2003.

125. O'Connell, M. J., Boul, P., Ericson, L. M., Huffman, C., Wang, Y., Haroz, E., Kuper, C., Tour, J., Ausman, K. D., and Smalley, R. E.: Reversible water-solubilization of single-walled carbon nanotubes by polymer wrapping. Chem. Phys. Lett., 342(34):265–271, 2001.

126. Král, P. and Tománek, D.: Laser-driven atomic pump. Phys. Rev. Lett., 82:5373–5376, 1999.

127. Wang, B. and Král, P.: Coulombic dragging of molecules on surfaces induced by separately flowing liquids. J. Am. Chem. Soc., 128(50):15984–15985, 2006.

128. Moseler, M. and Landman, U.: Formation, stability, and breakup of nanojets. Science, 289(5482):1165–1169, 2000.

129. Lee, K.-B., Park, S.-J., Mirkin, C. A., Smith, J. C., and Mrksich, M.: Protein nanoarrays generated by dip-pen nanolithography. Science, 295(5560):1702–1705, 2002.

130. Carr, R., Weinstock, I. A., Sivaprasadarao, A., Müller, A., and Aksimentiev, A.: Synthetic ion channels via self-assembly: A route for embedding porous polyoxometalate nanocapsules in lipid bilayer membranes. Nano Lett., 8(11):3916–3921, 2008.

131. Neri, M., Baaden, M., Carnevale, V., Anselmi, C., Maritan, A., and Carloni, P.: Microseconds dynamics simulations of the outer-membrane protease T. Biophys. J., 94(1):71–78, 2008.

132. Wallace, E. J. and Sansom, M. S. P.: Carbon nanotube/detergent interactions via coarse-grained molecular dynamics. Nano Lett., 7(7):1923–1928, 2007.

133. Titov, A. V., Král, P., and Pearson, R.: Sandwiched graphenemembrane superstructures. ACS Nano, 4(1):229–234, 2010.

134. Feller, S. E., Zhang, Y., Pastor, R. W., and Brooks, B. R.: Constant pressure molecular dynamics simulation: The langevin piston method. J. Chem. Phys., 103(11):4613–4621, 1995.

135. Richard, C., Balavoine, F., Schultz, P., Ebbesen, T. W., and Mioskowski, C.: Supramolecular self-assembly of lipid derivatives on carbon nanotubes. Science, 300(5620):775–778, 2003.

136. Zhou, R., Huang, X., Margulis, C. J., and Berne, B. J.: Hydrophobic collapse in multidomain protein folding. Science, 305(5690):1605–1609, 2004.

137. Regan, B. C., Aloni, S., Ritchie, R. O., Dahmen, U., and Zettl, A.: Carbon nanotubes as nanoscale mass conveyors. Nature, 428(6986):924–927, 2004.

138. Král, P. and Shapiro, M.: Nanotube electron drag in flowing liquids. Phys. Rev. Lett., 86:131–134, 2001.

139. Ghosh, S., Sood, A. K., and Kumar, N.: Carbon nanotube flow sensors. Science, 299(5609):1042–1044, 2003.

140. Stan, G.: Condensation of a quasi-one dimensional gas within asingle wall carbon nanotube. J. Low. Temp. Phys., 157(3-4):374–381, 2009.

141. Arora, G. and Sandler, S. I.: Air separation by single wall carbon nanotubes: Thermodynamics and adsorptive selectivity. J. Chem. Phys., 123(4):044705, 2005.

142. Blankenburg, S., Bieri, M., Fasel, R., Müllen, K., Pignedoli, C. A., and Passerone, D.: Porous graphene as an atmospheric nanofilter. Small, 6(20):2266–2271, 2010.

143. Lee, J. and Aluru, N. R.: Separation of gases from gas–water mixtures using carbon nanotubes. Appl. Phys. Lett., 96(13):133108, 2010.

144. Corry, B.: Designing carbon nanotube membranes for efficient water desalination. J. Phys. Chem. B, 112(5):1427–1434, 2008.

145. Noy, A., Park, H. G., Fornasiero, F., Holt, J. K., Grigoropoulos, C. P., and Bakajin, O.: Nanofluidics in carbon nanotubes. Nano Today, 2(6):22–29, 2007.

146. Sint, K., Wang, B., and Král, P.: Selective ion passage through functionalized graphene nanopores. J. Am. Chem. Soc., 130(49):16448–16449, 2008.

147. Hauser, A. W. and Schwerdtfeger, P.: Nanoporous graphene membranes for efficient ^{3}He/^{4}He separation. J. Phys. Chem. Lett., 3(2):209–213, 2012.

148. Nair, R. R., Wu, H. A., Jayaram, P. N., Grigorieva, I. V., and Geim, A. K.: Unimpeded permeation of water through helium-leaktight graphene-based membranes. Science, 335(6067):442–444, 2012.

149. Garaj, S., Hubbard, W., Reina, A., Kong, J., Branton, D., and Golovchenko, J. A.: Graphene as a subnanometre trans-electrode membrane. Nature, 467(7312):190–193, 2010.

150. Nelson, T., Zhang, B., and Prezhdo, O. V.: Detection of nucleic acids with graphene nanopores: Ab initio characterization of a novel sequencing device. Nano Lett., 10(9):3237–3242, 2010.

151. Baskin, A. and Král, P.: Electronic structures of porous nanocarbons. Sci. Rep., 1:36, 2011.

152. Kim, M., Sohn, K., Kim, J., and Hyeon, T.: Synthesis of carbon tubes with mesoporous wall structure using designed silica tubes as templates. Chem. Commun., 7:652–653, 2003.

153. Rodriguez, A. T., Chen, M., Chen, Z., Brinker, C. J., and Fan, H.: Nanoporous carbon nanotubes synthesized through confined hydrogen-bonding self-assembly. J. Am. Chem. Soc., 128(29):9276–9277, 2006.

154. Kulathunga, D. D. T. K., Ang, K. K., and Reddy, J. N.: Molecular dynamics analysis on buckling of defective carbon nanotubes. J. Phys. C: Condens. Matter., 22(34):345301, 2010.

155. Hirai, Y., Nishimaki, S., Mori, H., Kimoto, Y., Akita, S., Nakayama, Y., and Tanaka, Y.: Molecular dynamics studies on mechanical properties of carbon nanotubes with pinhole defects. Jpn. J. Appl. Phys., (34):4120–4123, 2003.

156. Hata, H., Saeki, S., Kimura, T., Sugahara, Y., and Kuroda, K.: Adsorption of taxol into ordered mesoporous silicas with various pore diameters. Chem. Mater., 11(4):1110–1119, 1999.

157. Burfield, D. R., Lee, K.-H., and Smithers, R. H.: Desiccant efficiency in solvent drying. a reappraisal by application of a novel method for solvent water assay. J. Org. Chem., 42(18):3060–3065, 1977.

158. Davis, M. E. and Lobo, R. F.: Zeolite and molecular sieve synthesis. Chem. Mater., 4(4):756–768, 1992.

159. Kalra, A., Garde, S., and Hummer, G.: Osmotic water transport through carbon nanotube membranes. Proc. Natl. Acad. Sci. USA, 100(18):10175–10180, 2003.

160. Harkins, W. D. and Brown, F. E.: The determination of surface tension (free surface energy), and the weight of falling drops: The surface tension of water and benzene by the capillary height method. J. Am. Chem. Soc., 41(4):499–524, 1919.

161. Beu, T. A.: Molecular dynamics simulations of ion transport through carbon nanotubes. I. influence of geometry, ion specificity, and many-body interactions. J. Chem. Phys., 132(16):164513, 2010.

162. Fornasiero, F., Park, H. G., Holt, J. K., Stadermann, M., Grigoropoulos, C. P., Noy, A., and Bakajin, O.: Ion exclusion by sub-2-nm carbon nanotube pores. Proc. Natl. Acad. Sci. USA, 11:17250–17255, 2008.

163. Banerjee, S., Murad, S., and Puri, I. K.: Preferential ion and water intake using charged carbon nanotubes. Chem. Phys. Lett., 434(46):292 – 296, 2007.

164. Park, J. H., Sinnott, S. B., and Aluru, N. R.: Ion separation using a Y-junction carbon nanotube. Nanotechnology, 17(3):895, 2006.

165. Lee, S. W., Yabuuchi, N., Gallant, B. M., Chen, S., Kim, B.-S., Hammond, P. T., and Shao-Horn, Y.: High-power lithium batteries from functionalized carbon-nanotube electrodes. Nat. Nano., 5(7):531–537, 2010.

166. Pan, H., Li, J., and Feng, Y. P.: Carbon nanotubes for supercapacitors. Nanoscale Res. Lett., 5(7):654–668, 2010.

167. Zhao, W.-H., Shang, B., Du, S.-P., Yuan, L.-F., Yang, J., and Zeng, X. C.: Highly selective adsorption of methanol in carbon nanotubes immersed in methanol-water solution. J. Chem. Phys., 137(3):034501, 2012.

168. Mao, Z. and Sinnott, S. B.: Separation of organic molecular mixtures in carbon nanotubes and bundles: molecular dynamics simulations. J. Phys. Chem. B, 105(29):6916–6924, 2001.

169. The CNT-benzene (or CNT-ethanol) binding energies are calculated as the difference of the total vdW energy of the system, when the system components are at the normal binding distance, and when they are separated by 5 nm. averaging of the energies is done over 200 consecutive frames of the simulation trajectory, with a 1 ps time interval. the binding energy density (kcal/mol/atom) of CNT-benzene is obtained from dividing the average binding energy by the number of atoms of benzene molecules. similarly, CNT-ethanol binding energy density is calculated.

170. Wiradharma, N., Zhang, Y., Venkataraman, S., Hedrick, J. L., and Yang, Y. Y.: Self-assembled polymer nanostructures for delivery of anticancer therapeutics. Nano Today, 4(4):302–317, 2009.

171. Harada, A. and Kataoka, K.: Supramolecular assemblies of block copolymers in aqueous media as nanocontainers relevant to biological applications. Prog. Polym. Sci., 31(11):949–982, 2006.

172. Israelachvili, J. N., Mitchell, D. J., and Ninham, B. W.: Theory of self-assembly of hydrocarbon amphiphiles into micelles and bilayers. J. Chem. Soc., Faraday Trans. 2, 72:1525–1568, 1976.

173. Whitesides, G., Mathias, J., and Seto, C.: Molecular self-assembly and nanochemistry: a chemical strategy for the synthesis of nanostructures. Science, 254(5036):1312–1319, 1991.

174. Rosen, B. M., Wilson, C. J., Wilson, D. A., Peterca, M., Imam, M. R., and Percec, V.: Dendron-mediated self-assembly, disassembly, and self-organization of complex systems. Chem. Rev., 109(11):6275–6540, 2009.

175. Hong, S., Leroueil, P. R., Majoros, I. J., Orr, B. G., Baker., J. J. R., and Holl, M. M. B.: The binding avidity of a nanoparticle-based multivalent targeted drug delivery platform. Chem. Biol., 14(1):107–115, 2007.

176. McNerny, D. Q., Kukowska-Latallo, J. F., Mullen, D. G., Wallace, J. M., Desai, A. M., Shukla, R., Huang, B., Banaszak Holl, M. M., and Baker, J. R.: RGD dendron bodies; synthetic avidity agents with defined and potentially interchangeable effector sites that can substitute for antibodies. Bioconjugate Chem., 20(10):1853–1859, 2009.

177. Papp, I., Sieben, C., Ludwig, K., Roskamp, M., Bttcher, C., Schlecht, S., Herrmann, A., and Haag, R.: Inhibition of influenza virus infection by multivalent sialic-acid-

functionalized gold nanoparticles. Small, 6(24):2900–2906, 2010.

178. Kostiainen, M. A., Szilvay, G. R., Lehtinen, J., Smith, D. K., Linder, M. B., Urtti, A., and Ikkala, O.: Precisely defined proteinpolymer conjugates: Construction of synthetic dna binding domains on proteins by using multivalent dendrons. ACS Nano, 1(2):103–113, 2007.

179. Tian, L. and Hammond, P. T.: Comb-dendritic block copolymers as tree-shaped macromolecular amphiphiles for nanoparticle self-assembly. Chem. Mater., 18(17):3976–3984, 2006.

180. Poon, Z., Chen, S., Engler, A. C., Lee, H., Atas, E., vonMaltzahn, G., Bhatia, S. N., and Hammond, P. T.: Ligand-clustered patchy nanoparticles for modulated cellular uptake and in vivo tumor targeting. Angew. Chem., Int. Ed., 49(40):7266–7270, 2010.

181. Lu, C., Guo, S., Liu, L., Zhang, Y., Li, Z., and Gu, J.: Aggregation behavior of MPEG-PCL diblock copolymers in aqueous solutions and morphologies of the aggregates. J. Polym. Sci., Part B: Polym. Phys., 44(23):3406–3417, 2006.

182. Liu, J., Zeng, F., and Allen, C.: In vivo fate of unimers and micelles of a poly(ethylene glycol)-block-poly(caprolactone) copolymer in mice following intravenous administration. Eur. J. Pharm. Biopharm., 65(3):309–319, 2007.

183. Ding, B. S., Dziubla, T., Shuvaev, V. V., Muro, S., and Muzykantov, V.: Advanced drug delivery systems that target the vascular endothelium. Mol. Interventions, 6(1):98–112, 2006.

184. Bae, J. W., Pearson, R. M., Patra, N., Sunoqrot, S., Vuković, L., Král, P., and Hong, S.: Dendron-mediated self-assembly of highly pegylated block copolymers: a modular nanocarrier platform. Chem. Commun., 47:10302–10304, 2011.

185. Gaucher, G., Dufresne, M.-H., Sant, V. P., Kang, N., Maysinger, D., and Leroux, J.-C.: Block copolymer micelles: preparation, characterization and application in drug delivery. J. Controlled Release, 109(13):169–188, 2005.

186. Kim, S. Y., Shin, I. G., Lee, Y. M., Cho, C. S., and Sung, Y. K.: Methoxy poly(ethylene glycol) and ϵ-caprolactone amphiphilic block copolymeric micelle containing indomethacin.: II. micelle formation and drug release behaviours. J. Controlled Release, 51(1):13–22, 1998.

187. Zhou, G. and Smid, J.: Micellization of amphiphilic star polymers with poly(ethylene oxide) arms in aqueous solutions. Langmuir, 9(11):2907–2913, 1993.

188. Ward, I. M.: Mechanical properties of solid polymers. New York, John Wiley and Sons, 1971.

189. Chen, T., Zhang, Z., and Glotzer, S. C.: A precise packing sequence for self-assembled convex structures. Proc. Natl. Acad. Sci. USA, 104(3):717–722, 2007.

190. Kellermann, M., Bauer, W., Hirsch, A., Schade, B., Ludwig, K., and Böttcher, C.: The first account of a structurally persistent micelle. Angew. Chem., Int. Ed., 43(22):2959–2962, 2004.

191. Kratzat, K. and Finkelmann, H.: Influence of the molecular geometry of nonionic surfactants on surface and micellar properties in aqueous solutions. Langmuir, 12(7):1765–1770, 1996.

192. Zeng, F., Liu, J., and Allen, C.: Synthesis and characterization of biodegradable poly(ethylene glycol)-block-poly(5-benzyloxy-trimethylene carbonate) copolymers for drug delivery. Biomacromolecules, 5(5):1810–1817, 2004.

193. Nagarajan, R.: Molecular packing parameter and surfactant self-assembly: The neglected role of the surfactant tail. Langmuir, 18(1):31–38, 2002.

194. Kataoka, K., Harada, A., and Nagasaki, Y.: Block copolymer micelles for drug delivery: Design, characterization and biological significance. Adv. Drug Delivery Rev., 47(1):113–131, 2001.

195. Duncan, R.: The dawning era of polymer therapeutics. Nat. Rev. Drug. Discov., 2(5):347–360, 2003.

196. Peer, D., Karp, J. M., Hong, S., Farokhzad, O. C., Margalit, R., and Langer, R.: Nanocarriers as an emerging platform for cancer therapy. Nat. Nano., 2(12):751–760, 2007.

197. Jin, S.-E., Bae, J. W., and Hong, S.: Multiscale observation of biological interactions of nanocarriers: From nano to macro. Microsc. Res. Tech., 73(9):813–823, 2010.

198. Zhao, F., Zhao, Y., Liu, Y., Chang, X., Chen, C., and Zhao, Y.: Cellular uptake, intracellular trafficking, and cytotoxicity of nanomaterials. Small, 7(10):1322–1337, 2011.

199. Lee, C. C., MacKay, J. A., Frechet, J. M. J., and Szoka, F. C.: Designing dendrimers for biological applications. Nat. Biotechnol., 23(12):1517–1526, 2005.

200. Myung, J. H., Gajjar, K. A., Saric, J., Eddington, D. T., and Hong, S.: Dendrimer-mediated multivalent binding for the enhanced capture of tumor cells. Angew. Chem., Int. Ed., 50(49):11769–11772, 2011.

201. Pearson, R. M., Sunoqrot, S., Hsu, H. J., Bae, J. W., and Hong, S.: Dendritic nanoparticles: the next generation of nanocarriers? Ther. Delivery, 3(49):941–959, 2012.

202. Duncan, R. and Izzo, L.: Dendrimer biocompatibility and toxicity. Adv. Drug Delivery Rev., 57(15):2215–2237, 2005.

203. Hong, S., Rattan, R., Majoros, I. J., Mullen, D. G., Peters, J. L., Shi, X., Bielinska, A. U., Blanco, L., Orr, B. G., Baker, J. R., and Holl, M. M. B.: The role of ganglioside gm1 in cellular internalization mechanisms of poly(amidoamine) dendrimers. Bioconjugate Chem., 20(8):1503–1513, 2009.

204. Kitchens, K. M., Kolhatkar, R. B., Swaan, P. W., and Ghandehari, H.: Endocytosis inhibitors prevent poly(amidoamine) dendrimer internalization and permeability across caco-2 cells. Mol. Pharmaceutics, 5(2):364–369, 2008.

205. Albertazzi, L., Serresi, M., Albanese, A., and Beltram, F.: Dendrimer internalization and intracellular trafficking in living cells. Mol. Pharmaceutics, 7(3):680–688, 2010.

206. Hong, S., Bielinska, A. U., Mecke, A., Keszler, B., Beals, J. L., Shi, X., Balogh, L., Orr, B. G., Baker, J. R., and Banaszak Holl, M. M.: Interaction of poly(amidoamine) dendrimers with supported lipid bilayers and cells: hole formation and the relation to transport. Bioconjugate Chem., 15(4):774–782, 2004.

207. Leroueil, P. R., Hong, S., Mecke, A., Baker, J. R., Orr, B. G., and Banaszak Holl, M. M.: Nanoparticle interaction with biological membranes: Does nanotechnology present a janus face? Acc. Chem. Res., 40(5):335–342, 2007.

208. Yang, Y., Sunoqrot, S., Stowell, C., Ji, J., Lee, C.-W., Kim, J. W., Khan, S. A., and Hong, S.: Effect of size, surface charge, and hydrophobicity of poly(amidoamine) dendrimers on their skin penetration. Biomacromolecules, 13(7):2154–2162, 2012.

209. Owens, D. E. and Peppas, N. A.: Opsonization, biodistribution, and pharmacokinetics of polymeric nanoparticles. Int. J. Pharm., 307(1):93–102, 2006.

210. Yan, J., Ye, Z., Luo, H., Chen, M., Zhou, Y., Tan, W., Xiao, Y., Zhang, Y., and Lang, M.: Synthesis, characterization, fluorescence labeling and cellular internalization of novel amine-functionalized poly(ethylene glycol)-block-poly([varepsilon]-caprolactone) amphiphilic block copolymers. Polym. Chem., 2:1331–1340, 2011.

211. Zhang, Y., Zhang, Q., Zha, L., Yang, W., Wang, C., Jiang, X., and Fu, S.: Preparation, characterization and application of pyrene-loaded methoxy poly(ethylene glycol)poly(lactic acid) copolymer nanoparticles. Colloid Polym. Sci., 282(12):1323–1328, 2004.

212. Bechaer, P. and Schick, M. J.: Macroemulsions: Nonionic Surfactants Physical Chemistry. New York, Marcel Dekker, 1987.

213. Sunoqrot, S., Bae, J. W., Pearson, R. M., Shyu, K., Liu, Y., Kim, D.-H., and Hong, S.: Temporal control over cellular targeting through hybridization of folate-targeted dendrimers and peg-pla nanoparticles. Biomacromolecules, 13(4):1223–1230, 2012.

214. Veronese, F. M. and Pasut, G.: Pegylation, successful approach to drug delivery. Drug Discovery Today, 10(21):1451–1458, 2005.

215. Xiao, K., Li, Y., Luo, J., Lee, J. S., Xiao, W., Gonik, A. M., Agarwal, R. G., and Lam, K. S.: The effect of surface charge on in vivo biodistribution of peg-oligocholic acid based micellar nanoparticles. Biomaterials, 32(13):3435–3446, 2011.

216. Hu, Y., Xie, J., Tong, Y. W., and Wang, C.-H.: Effect of PEG conformation and particle size on the cellular uptake efficiency of nanoparticles with the HepG2 cells. J. Controlled Release, 118(1):7–17, 2007.

217. Fan, W., Wu, X., Ding, B., Gao, J., Cai, Z., Zhang, W., Yin, D., Wang, X., Zhu, Q., Liu, J., Ding, X., and Gao, S.: Degradable gene delivery systems based on pluronics-modified low-molecular-weight polyethylenimine: Preparation, characterization, intracellular trafficking, and cellular distribution. Int. J. Nanomed., 7(1):1127–1138, 2012.

218. Vuković, L., Khatib, F. A., Drake, S. P., Madriaga, A., Brandenburg, K. S., Král, P., and Onyüksel, H.: Structure and dynamics of highly peg-ylated sterically stabilized micelles in aqueous media. J. Am. Chem. Soc., 133(34):13481–13488, 2011.

219. Girit, C. O., Meyer, J. C., Erni, R., Rossell, M. D., Kisielowski, C., Yang, L., Park, C.-H., Crommie, M. F., Cohen, M. L., Louie, S. G., and Zettl, A.: Graphene at the edge: Stability and dynamics. Science, 323(5922):1705–1708, 2009.

220. Wu, J., Xie, L., Li, Y., Wang, H., Ouyang, Y., Guo, J., and Dai, H.: Controlled chlorine plasma reaction for noninvasive graphene doping. J. Am. Chem. Soc., 133(49):19668–19671, 2011.

221. Klintenberg, M., Lebègue, S., Katsnelson, M. I., and Eriksson, O.: Theoretical analysis of the chemical bonding and electronic structure of graphene interacting with group IA and group VIIA elements. Phys. Rev. B, 81:085433, 2010.

222. Boukhvalov, D. W. and Katsnelson, M. I.: Chemical functionalization of graphene. J. Phys.: Condens. Matter, 21(34):344205, 2009.

223. Hossain, M. Z., Johns, J. E., Bevan, K. H., Karmel, H. J., Liang, Y. T., Yoshimoto, S., Mukai, K., Koitaya, T., Yoshinobu, J., Kawai, M., Lear, A. M., Kesmodel, L. L., Tait, S. L., and Hersam, M. C.: Chemically homogeneous and thermally reversible oxidation of epitaxial graphene. Nat. Chem., 4(4):305–309, 2012.

224. Huang, B., Li, Z., Liu, Z., Zhou, G., Hao, S., Wu, J., Gu, B.-L., and Duan, W.: Adsorption of gas molecules on graphene nanoribbons and its implication for nanoscale molecule sensor. J. Phys. Chem. C, 112(35):13442–13446, 2008.

225. Wang, Q. H. and Hersam, M. C.: Room-temperature molecular-resolution characterization of self-assembled organic monolayers on epitaxial graphene. Nat. Chem., 1(3):206–211, 2009.

226. Katsnelson, M. I.: Graphene: carbon in two dimensions. Mater. Today, 10(12):20–27, 2007.

227. Castro Neto, A. H., Guinea, F., Peres, N. M. R., Novoselov, K. S., and Geim, A. K.: The electronic properties of graphene. Rev. Mod. Phys., 81:109–162, 2009.

228. Liu, L., Ryu, S., Tomasik, M. R., Stolyarova, E., Jung, N., Hybertsen, M. S., Steigerwald, M. L., Brus, L. E., and Flynn, G. W.: Graphene oxidation: Thickness-dependent etching and strong chemical doping. Nano Lett., 8(7):1965–1970, 2008.

229. Byun, I.-S., Yoon, D., Choi, J. S., Hwang, I., Lee, D. H., Lee, M. J., Kawai, T., Son, Y.-W., Jia, Q., Cheong, H., and Park, B. H.: Nanoscale lithography on monolayer graphene using hydrogenation and oxidation. ACS Nano, 5(8):6417–6424, 2011.

230. Si, Y. and Samulski, E. T.: Synthesis of water soluble graphene. Nano Lett., 8(6):1679–1682, 2008.

231. Elias, D. C., Nair, R. R., Mohiuddin, T. M. G., Morozov, S. V., Blake, P., Halsall, M. P., Ferrari, A. C., Boukhvalov, D. W., Katsnelson, M. I., Geim, A. K., and Novoselov, K. S.: Control of graphene's properties by reversible hydrogenation: Evidence for graphane. Science, 323(5914):610–613, 2009.

232. Balog, R., Jorgensen, B., Nilsson, L., Andersen, M., Rienks, E., Bianchi, M., Fanetti, M., Laegsgaard, E., Baraldi, A., Lizzit, S., Sljivancanin, Z., Besenbacher, F., Hammer, B., Pedersen, T. G., Hofmann, P., and Hornekaer, L.: Bandgap opening in graphene induced by patterned hydrogen adsorption. Nature Mater., 9(4):315–319, 2010.

233. Shytov, A. V., Abanin, D. A., and Levitov, L. S.: Long-range interaction between adatoms in graphene. Phys. Rev. Lett., 103:016806, 2009.

234. Samarakoon, D. K. and Wang, X.-Q.: Tunable band gap in hydrogenated bilayer graphene. ACS Nano, 4(7):4126–4130, 2010.

235. Wu, M., Tse, J. S., and Jiang, J. Z.: Unzipping of graphene by fluorination. J. Phys. Chem. Lett., 1(9):1394–1397, 2010.

236. Medeiros, P. V. C., Mascarenhas, A. J. S., de Brito Mota, F., and de Castilho, C. M. C.: A DFT study of halogen atoms adsorbed on graphene layers. Nanotechnology, 21(48):485701, 2010.

237. Lee, W. H., Suk, J. W., Chou, H., Lee, J., Hao, Y., Wu, Y., Piner, R., Akinwande, D., Kim, K. S., and Ruoff, R. S.: Selective-area fluorination of graphene with fluoropolymer and laser irradiation. Nano Lett., 12(5):2374–2378, 2012.

238. Yang, H., Chen, M., Zhou, H., Qiu, C., Hu, L., Yu, F., Chu, W., Sun, S., and Sun, L.: Preferential and reversible fluorination of monolayer graphene. J. Phys. Chem. C, 115(34):16844–16848, 2011.

239. Bon, S. B., Valentini, L., Verdejo, R., Garcia Fierro, J. L., Peponi, L., Lopez-Manchado, M. A., and Kenny, J. M.: Plasma fluorination of chemically derived graphene sheets and subsequent modification with butylamine. Chem. Mater., 21(14):3433–3438, 2009.

240. Ribas, M., Singh, A., Sorokin, P., and Yakobson, B.: Patterning nanoroads and quantum dots on fluorinated graphene. Nano Res., 4(1):143–152, 2011.

241. Robinson, J. T., Burgess, J. S., Junkermeier, C. E., Badescu, S. C., Reinecke, T. L., Perkins, F. K., Zalalutdniov, M. K., Baldwin, J. W., Culbertson, J. C., Sheehan, P. E., and Snow, E. S.: Properties of fluorinated graphene films. Nano Lett., 10(8):3001–3005, 2010.

242. Li, B., Zhou, L., Wu, D., Peng, H., Yan, K., Zhou, Y., and Liu, Z.: Photochemical chlorination of graphene. ACS Nano, 5(7):5957–5961, 2011.

243. Yang, M., Zhou, L., Wang, J., Liu, Z., and Liu, Z.: Evolutionary chlorination of graphene: From charge-transfer complex to covalent bonding and nonbonding. J. Phys. Chem. C, 116(1):844–850, 2012.

244. Zhang, L., Yu, J., Yang, M., Xie, Q., Peng, H., and Liu, Z.: Janus graphene from asymmetric two-dimensional chemistry. Nat. Commun., 4:1443, 2013.

245. Zheng, J., Liu, H.-T., Wu, B., Di, C.-A., Guo, Y.-L., Wu, T., Yu, G., Liu, Y.-Q., and Zhu, D.-B.: Production of graphite chloride and bromide using microwave sparks. Sci. Rep., 2:662, 2012.

246. Nakada, K., Fujita, M., Dresselhaus, G., and Dresselhaus, M. S.: Edge state in graphene ribbons: Nanometer size effect and edge shape dependence. Phys. Rev. B, 54:17954–17961, 1996.

247. Stoller, M. D., Park, S., Zhu, Y., An, J., and Ruoff, R. S.: Graphene-based ultracapacitors. Nano Lett., 8(10):3498–3502, 2008.

248. Loh, K. P., Bao, Q., Eda, G., and Chhowalla, M.: Graphene oxide as a chemically tunable platform for optical applications. Nat. Chem., 2(12):1015–1024, 2010.

249. Merlet, C., Rotenberg, B., Madden, P. A., Taberna, P.-L., Simon, P., Gogotsi, Y., and Salanne, M.: On the molecular origin of supercapacitance in nanoporous carbon electrodes. Nature, 11(4):306–310, 2012.

250. Grimme, S., Antony, J., Ehrlich, S., and Krieg, H. A.: A consistent and accurate ab initio parametrization of density functional dispersion correction (DFT-D) for the 94 elements H-Pu. J. Chem. Phys., 132(35):154104, 2010.

251. Grimme, S., Ehrlich, S., and Goerigk, L.: Effect of the damping function in dispersion corrected density functional theory. J. Comput. Chem., 32(7):1456–1465, 2011.

252. Polo, V., Kraka, E., and Cremer, D.: Electron correlation and the self-interaction error of density functional theory. Mol. Phys., 100(11):1771–1790, 2002.

253. Kästner, J., Carr, J. M., Keal, T. W., Thiel, W., Wander, A., and Sherwood, P.: DL-FIND: An open-source geometry optimizer for atomistic simulations. J. Phys. Chem. A, 113(35):11856–11865, 2009.

254. Lee, H.: Preferential functionalization on zigzag graphene nanoribbons: First-principles calculations. J. Phys.: Condens. Matter, 22(35):352205, 2010.

255. Irvine, W. M., Goldsmith, P. F., and Hjalmarson, Å: Chemical abundances in molecular clouds. In: Interstellar Processes, eds. D. J. Hollenbach and, H. A. Thronson, pp. 561–610, Dordrecht, D. Reidel Publ. Co., 1987.

256. Ohishi, M. and Kaifu, N.: Chemical and physical evolution of dark clouds molecular spectral line survey toward tmc-1. Faraday Discuss., 109:205–216, 1998.

257. Winnewisser, G. and Kramer, C.: Spectroscopy between the stars. Space Sci. Rev., 90(1-2):181–202, 1999.

258. Schutte, W. A.: Formation and evolution of interstellar icy grain mantels. In: The Cosmic Dust Connection, eds. J. M. Greenberg, pp. 1–42, Dordrecht, Kluwer, 1996.

259. Herbst, E. and van Dishoeck, E. F.: Complex organic interstellar molecules. Annu. Rev. Astron. Astr., 47(1):427–480, 2009.

260. Hollis, J. M., Lovas, F. J., and Jewell, P. R.: Interstellar glycolaldehyde: The first sugar. ApJL, 540(2):L107, 2000.

261. Tielens, A. G. G. M.: Interstellar polycyclic aromatic hydrocarbon molecules. Annu. Rev. Astron. Astr., 46(1):289–337, 2008.

262. Salama, F.: PAHs in astronomy-a review. In: Organic matter in space, eds. S. Kwok and S. Sandford, pp. 357-365. Proc. IAU Symp., 2008.

263. Ehrenfreund, P. and Sephton, M. A.: Carbon molecules in space: from astrochemistry to astrobiology. Faraday Discuss., 133:277–288, 2006.

264. Duley, W. W.: Polycyclic aromatic hydrocarbons, carbon nanoparticles and the diffuse interstellar bands. Faraday Discuss., 133:415–425, 2006.

265. Salama, F., Galazutdinov, G. A., Krelowski, J., Biennier, L., Beletsky, Y., and Song, I.-O.: Polycyclic aromatic hydrocarbons and the diffuse interstellar bands: A survey. ApJ, 728(2):154, 2011.

266. Ricks, A. M., Douberly, G. E., and Duncan, M. A.: The infrared spectrum of protonated naphthalene and its relevance for the unidentified infrared bands. ApJ, 702(1):301, 2009.

267. Spencer, M. K., Hammond, M. R., and Zare, R. N.: Laser mass spectrometric detection of extraterrestrial aromatic molecules: Mini-review and examination of pulsed heating effects. Proc. Natl. Acad. Sci. USA, 105(47):18096–18101, 2008.

268. Cami, J., Bernard-Salas, J., Peeters, E., and Malek, S. E.: Detection of C_{60} and C_{70} in a young planetary nebula. Science, 329(5996):1180–1182, 2010.

269. Sellgren, K., Werner, M. W., Ingalls, J. G., Smith, J. D. T., Carleton, T. M., and Joblin, C.: C_{60} in reflection nebulae. ApJL, 722(1):L54, 2010.

270. Allamandola, L. J., Tielens, A. G. G. M., and Barker, J. R.: Polycyclic aromatic hydrocarbons and the unidentified infrared emission bands - auto exhaust along the milky way. ApJ, 290(1):25–28, 1985.

271. Witt, A. N., Schild, R. E., and Kraiman, J. B.: Photometric study of NGC 2023 in the 3500 Å to 10000 Å region - confirmation of a near-IR emission process in reflection nebulae. ApJ, 291(1):708–718, 1984.

272. Bradley, J., Dai, Z. R., Erni, R., Browning, N., Graham, G., Weber, P., Smith, J., Hutcheon, I., Ishii, H., Bajt, S., Floss, C., Stadermann, F., and Sandford, S.: An astronomical 2175 Å feature in interplanetary dust particles. Science, 307(5707):244–247, 2005.

273. Eberlein, T., Bangert, U., Nair, R. R., Jones, R., Gass, M., Bleloch, A. L., Novoselov, K. S., Geim, A., and Briddon, P. R.: Plasmon spectroscopy of free-standing graphene films. Phys. Rev. B, 77:233406, 2008.

274. Parker, D. S. N., Zhang, F., Kim, Y. S., Kaiser, R. I., Landera, A., Kislov, V. V., Mebel, A. M., and Tielens, A. G. G. M.: Low temperature formation of naphthalene and its role in the synthesis of pahs (polycyclic aromatic hydrocarbons) in the interstellar medium. Proc. Natl. Acad. Sci. USA, 109(1):53–58, 2012.

275. Berné, O. and Tielens, A. G. G. M.: Formation of buckminsterfullerene (C_{60}) in interstellar space. Proc. Natl. Acad. Sci. USA, 109(2):401–406, 2012.

276. Irle, S., Zheng, G., Elstner, M., and Morokuma, K.: From C_2 molecules to self-assembled fullerenes in quantum chemical molecular dynamics. Nano Lett., 3(12):1657–1664, 2003.

277. Irle, S., Zheng, G., Wang, Z., and Morokuma, K.: The C_{60} formation puzzle solved: QM/MD simulations reveal the shrinking hot giant road of the dynamic fullerene self-assembly mechanism. J. Phys. Chem. B, 110(30):14531–14545, 2006.

278. Plimpton, S.: Fast parallel algorithms for short-range molecular dynamics. J. Comput. Phys., 117(1):1–19, 1995.

279. Lozovik, Y. E. and Popov, A. M.: Formation and growth of carbon nanostructures: fullerenes, nanoparticles, nanotubes and cones. Phys.-Usp., 40(1):717–737, 1997.

280. Chuvilin, A., Bichoutskaia, E., Gimenez-Lopez, M. C., Chamberlain, T. W., Rance, G. A., Kuganathan, N., Biskupek, J., Kaiser, U., and Khlobystov, A. N.: Self-assembly of a sulphur-terminated graphene nanoribbon within a single-walled carbon nanotube. Nat. Mater., 10(9):687–692, 2011.

Title: Nanodroplet Activated and Guided Folding of Graphene Nanostructures

Author: Niladri Patra, Boyang Wang, and Petr Král

Publication: Nano Letters

Publisher: American Chemical Society

Date: Nov 1, 2009

PERMISSION/LICENSE IS GRANTED FOR YOUR ORDER AT NO CHARGE

This type of permission/license, instead of the standard Terms & Conditions, is sent to you because no fee is being charged for your order. Please note the following:

- Permission is granted for your request in both print and electronic formats, and translations.
- If figures and/or tables were requested, they may be adapted or used in part.
- Please print this page for your records and send a copy of it to your publisher/graduate school.
- Appropriate credit for the requested material should be given as follows: "Reprinted (adapted) with permission from (COMPLETE REFERENCE CITATION). Copyright (YEAR) American Chemical Society." Insert appropriate information in place of the capitalized words.
- One-time permission is granted only for the use specified in your request. No additional uses are granted (such as derivative works or other editions). For any other uses, please submit a new request.

PERMISSION/LICENSE IS GRANTED FOR YOUR ORDER AT NO CHARGE

This type of permission/license, instead of the standard Terms & Conditions, is sent to you because no fee is being charged for your order. Please note the following:

- Permission is granted for your request in both print and electronic formats, and translations.
- If figures and/or tables were requested, they may be adapted or used in part.
- Please print this page for your records and send a copy of it to your publisher/graduate school.
- Appropriate credit for the requested material should be given as follows: "Reprinted (adapted) with permission from (COMPLETE REFERENCE CITATION). Copyright (YEAR) American Chemical Society." Insert appropriate information in place of the capitalized words.
- One-time permission is granted only for the use specified in your request. No additional uses are granted (such as derivative works or other editions). For any other uses, please submit a new request.

Home | Account Info | Help

Title:	Controlled Self-Assembly of Filled Micelles on Nanotubes
Author:	Niladri Patra and Petr Král
Publication:	Journal of the American Chemical Society
Publisher:	American Chemical Society
Date:	Apr 1, 2011

Logged in as:
Niladri Patra

LOGOUT

PERMISSION/LICENSE IS GRANTED FOR YOUR ORDER AT NO CHARGE

This type of permission/license, instead of the standard Terms & Conditions, is sent to you because no fee is being charged for your order. Please note the following:

- Permission is granted for your request in both print and electronic formats, and translations.
- If figures and/or tables were requested, they may be adapted or used in part.
- Please print this page for your records and send a copy of it to your publisher/graduate school.
- Appropriate credit for the requested material should be given as follows: "Reprinted (adapted) with permission from (COMPLETE REFERENCE CITATION). Copyright (YEAR) American Chemical Society." Insert appropriate information in place of the capitalized words.
- One-time permission is granted only for the use specified in your request. No additional uses are granted (such as derivative works or other editions). For any other uses, please submit a new request.

BACK | CLOSE WINDOW

Home | Account Info | Help

Title:	Dynamics of Ion Binding to Graphene Nanostructures
Author:	Niladri Patra, Dominic A. Esan, and Petr Král
Publication:	The Journal of Physical Chemistry C
Publisher:	American Chemical Society
Date:	May 1, 2013

Logged in as:
Niladri Patra

LOGOUT

PERMISSION/LICENSE IS GRANTED FOR YOUR ORDER AT NO CHARGE

This type of permission/license, instead of the standard Terms & Conditions, is sent to you because no fee is being charged for your order. Please note the following:

- Permission is granted for your request in both print and electronic formats, and translations.
- If figures and/or tables were requested, they may be adapted or used in part.
- Please print this page for your records and send a copy of it to your publisher/graduate school.
- Appropriate credit for the requested material should be given as follows: "Reprinted (adapted) with permission from (COMPLETE REFERENCE CITATION). Copyright (YEAR) American Chemical Society." Insert appropriate information in place of the capitalized words.
- One-time permission is granted only for the use specified in your request. No additional uses are granted (such as derivative works or other editions). For any other uses, please submit a new request.

BACK | CLOSE WINDOW

VITA

NAME: Niladri Patra

EDUCATION: B.Sc., Chemistry (Honours), Calcutta University, India, 2006

M. Sc., Chemistry, Indian Institute of Technology Delhi, India, 2008

Ph.D. Candidate, Computational Physical Chemistry, University of Illinois at Chicago, Illinois, August 2008 (expected graduation date: Fall 2013)

HONORS AND AWARD: Paaren Graduate Fellowship (2011-2012)
Harvard-Smithsonian Astrophysical Observatory Predoc Fellowship (2012-2013)

PROFESSIONAL MEMBERSHIP: American Chemical Society (since 2009)

ACADEMIC EXPERIENCE: Research Assistant
Modeled physical, chemical and biochemical systems, performed data analysis, prepared manuscripts

Teaching Assistant
Led discussions and practical laboratory sessions for groups of 20 undergraduate students in introductory chemistry courses for 4 semesters.
Assisted with instruction, evaluation, and mentoring of 80 students in undergraduate physical chemistry courses for 5 semesters.

PUBLICATIONS: Patra, N., Wang, B., and Král, P.: Nanodroplet Activated and Guided Folding of Graphene Nanostructures. Nano Lett. 9(11):3766-3771, 2009.

Mukherjee, G., Patra, N., Barua, P., and Jayaram, B.: Fast Empirical GAFF Compatible Partial Atomic Charge Assignment Scheme for Modeling Interactions of Small Molecules with Biomolecular Targets. J. Comp. Chem., 32(5):893-907, 2010.

Patra, N., Song, Y., and Král, P.: Nanotube Activated and Guided Folding of Graphene Nanostructures. ACS Nano, 5(3):1798-1804, 2011.

Král, P., Vuković, L., Patra, N., Wang, B., Sint, K., and Titov, A.: Control of Rotary Motion at the Nanoscale: Motility, actuation, self-assembly. J. Nanosci. Lett., 1(3):128-144, 2011.

Patra, N. and Král, P.: Controlled Self-assembly of filled Micelles on Nanotubes. J. Am. Chem. Soc. 133(16):6146-6149, 2011.

Bae, J. W., Pearson, R. M., Patra, N., Sunoqrot, S., Vuković, L., Král, P., and Hong, S.: Dendrons-mediated Self-assembly of highly PEGylated block copolymers: a modular nanocarrier platform. Chem. Comm., 47:10302-10304, 2011.

Pearson, R. M., Patra, N., Hsu, H.-J., Uddin, S., Král, P., and Hong, S.: Positively Charged Dendron Micelles Display Negligible Cellular Interactions. ACS Macro Lett., 2(1):77-81, 2013.

Patra, N., Esan, A. D., and Král, P.: Dynamics of Ion Binding to Graphene Nanostructures. J. Phys. Chem. C,117(20):10750-10754, 2013.

PAPER IN PREPARATION:

Yzeiri, I., Patra, N., and Král, P.: Porous Carbon Nanotubes: Molecular Absorption, Transport, and Separation. Submitted

Patra, N., Král, P., and Sadeghpour, H. R.: Self-assembly of Large Carbon-rich Structures in Interstellar Medium. In preparation.

PROCEEDINGS:

Král, P., Vuković, L., Patra, N., Wang, B., and Titov, A.: Control of Rotary Motion at the Nanoscale: Motility, Actuation, Self-assembly. Proceedings of the Beilstein Symposium on Functional Nanoscience, Bozen, June, 2011.

ORAL PRESENTATIONS:

Patra, N., Wang, B., and Král, P.: Nanodroplet Activated and Guided Folding of Graphene Nanostructures, 239th American Chemical Society National Meeting and Exposition, spring 2010, San Francisco, March 21–25, 2010.

Patra, N., Boyang Wang, Song, Y., and Král, P.: Activated and Guided Selfassembly of Graphene Nanostructures. 241st American Chemical Society National Meeting and Exposition, spring 2011, Anaheim, March 27–31, 2011.

Patra, N., Song, Y., and Král, P.: Controlled Self-Assembly of Nanostructures on Nanotubes. 243rd American Chemical Society National Meeting and Exposition, spring 2012, San Diego, March 25–29, 2012.

Patra, N., Esan, D. A., and Král, P.: Scanned Quantum Molecular Dynamics Simulations: Ion Binding to Graphene Nanostructures. 245th American Chemical Society National Meeting and Exposition, spring 2013, New Orleans, April 7-11, 2013.

Patra, N., Král, P., and Sadeghpour, H. R: Self-assembly of Carbon Atoms in Interstellar Space and Formation Mechanism of Naphthalene from Small Precursors: A Molecular Dynamics Study. CFA symposium, SAO, Harvard University, April 26, 2013.

POSTER PRESENTATIONS: 237th American Chemical Society National Meeting and Exposition, spring 2009, Salt Lake, Utah, March 22–26, 2009.

41st Midwest Theoretical Chemistry Conference, Carbondale, Illinois, May 28-30, 2009.

International Institute for Nanotechnology Symposium, October 29, 2009.

239th American Chemical Society National Meeting and Exposition, spring 2010, San Francisco, March 21–25, 2010.

42nd Midwest Theoretical Chemistry Conference, Purdue University, Indiana, May 20-22, 2010.

International Institute for Nanotechnology Symposium, October 21, 2010.

Workshop on Self-Assembled Bio-Inspired Materials for Energy, Argonne National Laboratory, February 4-5, 2011.

241st American Chemical Society Meeting and Exposition, spring 2011, Anaheim, March 27–31, 2011.

243rd American Chemical Society National Meeting and Exposition, spring 2012, San Diego, March 25–29, 2012.

44 th Midwest Theoretical Chemistry Conference, Wisconsin, Madison, June 7-9, 2012.

245th American Chemical Society National Meeting and Exposition, spring 2013, New Orleans, April 7–11, 2013.

WORKSHOP AND SUMMER SCHOOL ATTENDED:

Workshop on Multiscale Theory and Simulation, Center for Multiscale Theory and Simulation, University of Chicago, June 11-13, 2012.

Center for the physics of Living Cells, University of Illinois at Urbana- Champaign, July 30th - August 4th, 2012.

COMPUTER SKILLS:

Programming and Script Languages: FORTRAN 77/90/95, TCL
Molecular Modeling Packages: NAMD, LAMMPS, Quantum Espresso, TeraChem, Gaussian G09,
Applications: Visual Molecular Dynamics, LATEX, Gnuplot, PovRay, Video Mach, Gimp
Operating Systems: Linux, Windows

REFERENCES:

Prof. Petr Král, Associate Professor, Department of Chemistry, Adjunct Professor, Department of Physics, University of Illinois at Chicago, Chicago, IL 60607, USA pkral@uic.edu

Dr. Hossein. R. Sadeghpour, Director, Institute for Theoretical Atomic, Molecular and Optical Physics (ITAMP), Harvard Smithsonian Center for Astrophysics, Cambridge, MA 2138, USA, hsadeghpour@cfa.harvard.edu

Prof. Seungpyo Hong, Assistant Professor, Departments of Biopharmaceutical Sciences and Bioengineering, University of Illinois at Chicago, Chicago, IL 0612-7231, USA sphong@uic.edu